OPTIMIZATION VIA CFD

OF

AIRCRAFT HOT-AIR ANTI-ICING SYSTEMS

MATHIEU PAUL CONSTANTIN PELLISSIER
Computational Fluid Dynamics Laboratory, Department of Mechanical Engineering,
McGill University, Montréal, Québec, Canada

June 2010

A thesis submitted to McGill University in partial fulfillment of the requirements of the degree of Master of Engineering

ACKNOWLEDGEMENTS

I would like to especially thank my supervisor Professor Wagdi Habashi for having made this privileged experience possible and for his precious advice and guidance all along this Master's research project.

I would like to gratefully acknowledge the fact that this project was funded by the NSERC - J. Armand Bombardier Industrial Research Chair for Multidisciplinary CFD.

I would also like to address a special thanks to my lab-mates at the CFD Lab whose support and contributions were particularly appreciated. Thank you very much to Mostafa Najafiyazdi, Dr. Marco Fossati, Vladislav Lappo, Shezad Nilamdeen, Amir Borna, and Dr. Rooh-Ul-Amin Khurram.

I would like to gratefully thank Dr. Alberto Pueyo and Corentin Brette from Bombardier Aerospace Advanced Aerodynamics Aero-Icing Group for their advice, time and consideration.

I would also like to mention the highly appreciated availability and help of Yves Simard, the CFD Lab's System Administrator, the NTI (Newmerical Technologies International) team, Dr. Guido Baruzzi, Martin Aubé, HongZhi Wang, Karim Moumen, Patrick Lagacé, Cristhian Aliaga, Thomas Reid and Bruno Cassagne, and from the CFD Lab Associate Professor, Dr. Siva Nadarajah.

Last, but not least, I would like to gratefully thank my fiancée Maude for her unconditional support through this entire project.

ABSTRACT

In-flight icing is a major concern in aircraft safety and a non-negligible source of incidents and accidents, and is still a serious hazard today. It remains consequently a design and certification challenge for aircraft manufacturers. The aerodynamic performance of an aircraft can indeed degrade rapidly when flying in icing conditions, leading to incidents or accidents. In-flight icing occurs when an aircraft passes through clouds containing supercooled water droplets at or below freezing temperature. Droplets impinge on its exposed surfaces and freeze, causing roughness and shape changes that increase drag, decrease lift and reduce the stall angle of attack, eventually inducing flow separation and stall. This hazardous ice accretion is prevented by the use of dedicated anti-icing systems, among which hot-air-types are the most common for turbofan aircraft.

This work presents a methodology for the optimization of such aircraft hot-air-type anti-icing systems, known as Piccolo tubes. Having identified through 3D Computational Fluid Dynamics (CFD) the most critical in-flight icing conditions, as well as determined thermal power constraints, the objective is to optimize the heat distribution in such a way to minimize power requirements, while meeting or exceeding all safety regulation requirements. To accomplish this, an optimization method combining 3D CFD, Reduced-Order Models (ROM) and Genetic Algorithms (GA) is constructed to determine the optimal configuration of the Piccolo tube (angles of jets, spacing between holes, and position from leading edge). The methodology successfully results in increasingly optimal configurations from three up to five design variables.

RESUME

Le givrage en vol constitue encore et toujours un souci majeur de sûreté en aviation et demeure une source non négligeable d'incidents et d'accidents. Ainsi, le givrage en vol reste un défi de taille en termes de conception et de certification pour les constructeurs aéronautiques. Les performances aérodynamiques d'un avion peuvent en effet se dégrader rapidement quand il vole en conditions givrantes, et ainsi engendrer des incidents ou même des accidents. Le givrage en vol a lieu quand un avion traverse des nuages contenant des gouttelettes d'eau surfondues à des températures inférieures ou égales au point de congélation. Les gouttelettes impactent sur les zones exposées et gèlent, ce qui augmente la rugosité, provoquant une augmentation de la traînée, une diminution de la portance et de l'angle de décrochage, et induisant éventuellement la séparation de l'écoulement et le décrochage. L'accrétion de glace est empêchée par l'utilisation de systèmes dédiés d'antigivrage, parmi lesquels les systèmes à air chaud sont les plus utilisés par les avions de ligne.

Cet ouvrage présente une méthodologie en vue de l'optimisation de tels systèmes d'antigivrage à air chaud appelés tubes Piccolo. Ayant identifié les conditions de givrage en vol les plus sévères à l'aide de la CFD (Computational Fluid Dynamics, ou simulation numérique en dynamique des fluides) tridimensionnelle ainsi que les contraintes de puissance thermique liées au système de dégivrage, l'objectif est d'optimiser la distribution de chaleur de façon à minimiser la puissance thermique requise, tout en satisfaisant aux réglementations de sûreté en vol. Dans ce but, une méthode d'optimisation combinant la CFD 3D, la Modélisation d'Ordre Réduit (MOR) et les Algorithmes Genétiques (AG), est développée afin de déterminer la configuration optimale du tube Piccolo (en termes d'angles de jets, de distance entre les jets et de distance au bord d'attaque). Cette méthodologie mène à des configurations d'optimalité croissante de trois à cinq variables.

TABLE OF CONTENTS

NOMENCLATURE

Symbols

A, Γ	Energy equation influence matrix [J/s/K]
$[b]$, $[b^{\circ}]$, $[b^{*}]$	Energy equation Right Hand Side vector [J/s]
c	Distance between adjacent jets [m]
c_p	Specific heat capacity [J/kg/K]
d	Piccolo tube jet nozzle diameter [m]
dr	Radius increment [m]
dZ_W	Spanwise width of local cell [m]
D	Piccolo tube diameter [m]
e	Airfoil skin thickness [m]
f	Freezing fraction []
f_{rec}	Recovery factor []
GA	Genetic Algorithm
h_c	Local heat transfer coefficient [W/m^2/K]
h_f	Local water film height [m]
H_r	Relative humidity []
k	Thermal conductivity of the fluid [W/m/K]
K	Continuity equation influence matrix [kg/s/m]
L_{fus}	Latent heat of fusion [J/m^3]
L_{vap}	Latent heat of vaporization [J/m^3]
LWC	Liquid Water Content [kg/m^3]
M	Mach number []
$\dot{m}$	Mass flow rate [kg/s]
$\dot{m}''$	Mass flux [kg/s/m^2]
nm	Number of modes
ns	Number of snapshots
Nu_r	Local Nusselt number based on Piccolo hole diameter [], $Nu = h_c \cdot d/k$
$\overline{Nu}$	Mean Nusselt number based on Piccolo hole diameter [], $\overline{Nu} = \overline{h_c} \cdot d/k$
$ObjFct$	Objective function []
p	Penalty factor []
P, P_s	Local static pressure [Pa]
P_{vap}	Saturation vapor pressure [Pa]
POD	Proper Orthogonal Decomposition

Pr	Prandtl number [], $\mathrm{Pr} = \mu \cdot Cp/k$
$\dot{Q}$	Thermal power [J/s]
$\dot{Q}''$	Heat flux [J/s/m^2]
r, R	Radial distance from Piccolo jet axis [m]
[R]	Energy equation residual vector [J/s]
Re	Jet Reynolds number [], $\mathrm{Re} = 4 \cdot \dot{m}_{jet} / (\pi \cdot d \cdot \mu)$
ROM	Reduced Order Model
s	Curvilinear coordinate [m]
S	Surface area of local cell [m^2]
T , $\tilde{T}$	Local and reduced local temperature [K], $\tilde{T} = T - 273.15$
[T]	Temperature vector [K]
U_j	POD snapshot solution vector [-]
$\hat{U}$	POD target solution vector [-]
U_d	Droplet free stream velocity [m/s]
$\overline{U}_f$	Water film mean velocity [m/s]
U, V	Velocity [m/s]
X_{Pic}, Y_{Pic}	Local Cartesian coordinates of the Piccolo tube axis [m]
z_n	Normal distance from Piccolo hole to internal surface skin [m]
α	Relaxation factor []
α_{ij}	POD snapshot coefficient []
$\hat{\alpha}_i$	POD target coefficient []
β	Water droplets collection efficiency
$[\Delta h_f]$	Film height delta vector [m]
Δs	Length of local cell [m]
$[\Delta T]$	Temperature delta vector [K]
ε	Skin emissivity []
θ	Jet orientation angle [°]
λ	Thermal conductivity of the metal skin [W/m/K]
μ	Dynamic viscosity [Pa.s]
ρ	Density [kg/m^3]
τ_W	Wall shear stress [Pa]
σ	Boltzmann constant [$\sigma = 5.670 \times 10^{-8}$ W/m^2/K^4]
Φ_i	POD eigenfunction [-]

Subscripts

adiab	Adiabatic
anti-ice	Anti-icing
cond	Conduction
conv	Convection
d	Droplet
evap, vap	Evaporation
exhaust	Piccolo exhaust
ext	External flow
f	Water film
fus	Fusion
ice	Ice
ideal	Ideal target
in, IN	Coming in the control volume
int	Internal flow
jet	Piccolo jet
loss	Losses within Piccolo tube system
mean	Mean
out, OUT	Coming out of the control volume
Pic	Piccolo tube
rad	Radiation
rb	Water runback
ref	Reference value
tot	Total
w	Water
W	Wall
β	Droplet impingement
∞	External flow free-stream value

Superscripts

POD	Derived from POD solution
total	Over the entire leading edge
upper	Over the upper surface of the leading edge

LIST OF FIGURES

LIST OF TABLES

1. INTRODUCTION

1.1 In-Flight Icing

In-flight icing is a major concern in aircraft safety, a non-negligible source of accidents and is still a serious hazard today [1-3]. As a consequence, it remains a design and certification challenge for the aircraft manufacturers.

Indeed, the aerodynamic performance of an unprotected aircraft flying in icing conditions can degrade rapidly and if not treated appropriately, lead to incidents and accidents. In-flight icing generally occurs at or below the freezing point when an aircraft passes through clouds containing supercooled droplets [4-9] (unstable physical state where droplets remain liquid even far below freezing point). Also, freezing rain can occur at the interface between warm and cold fronts (in this case, the droplets are usually of bigger size and referred to as "Supercooled Large Droplets" or SLD).

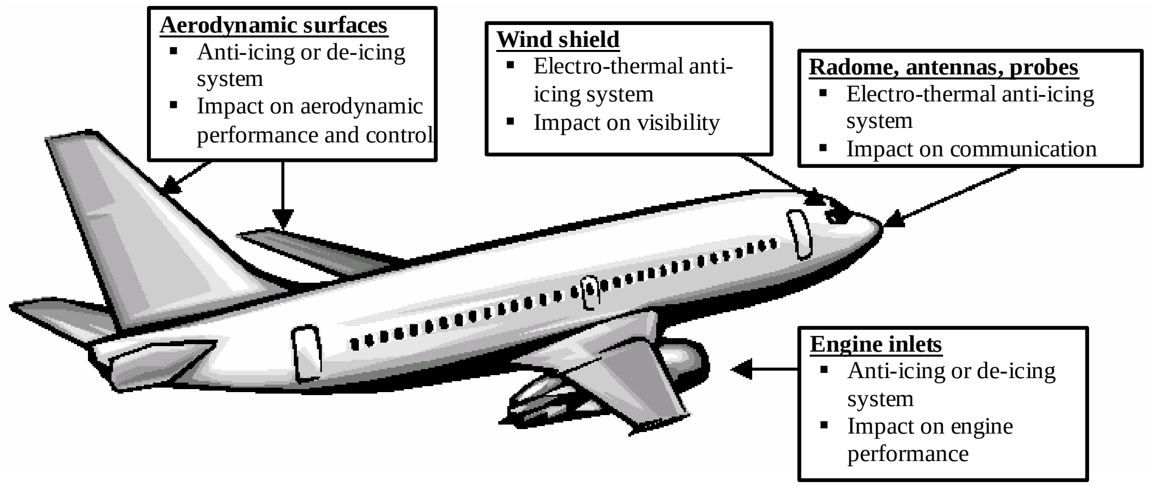

Figure 1-1: Aircraft components affected by in-flight icing, and effect.

Supercooled droplets impinging on the aircraft' exposed surfaces (cf. Figure 1-1, adapted from [10]) will either freeze upon impact to form rime ice, or run back on the surface and freeze further downstream to form glaze ice. In rime-ice conditions or "dry regime" (usually for air temperatures below -20°C) the ice will accrete in a dense opaque streamlined shape. In glaze-ice conditions or "wet regime" (usually for air temperatures between 0°C and -20°C) the ice will accrete in transparent irregular horn-like shapes (cf. Figure 1-2). Mixed-ice conditions can also be encountered. The severity of ice accretion, in terms of quantity and location, is affected by:

- The flight configuration:

    - Free-stream velocity
    - Angle of Attack (AoA)
    - Altitude
    - High-lift systems configuration
    - Flight phase
- The icing conditions:
    - Ambient air temperature
    - Liquid Water Content (LWC)
    - Droplet size distribution

These parameters directly impact the droplet collection efficiency and the ice accretion is then highly dependent on the exposure time and the efficiency of the anti-icing system.

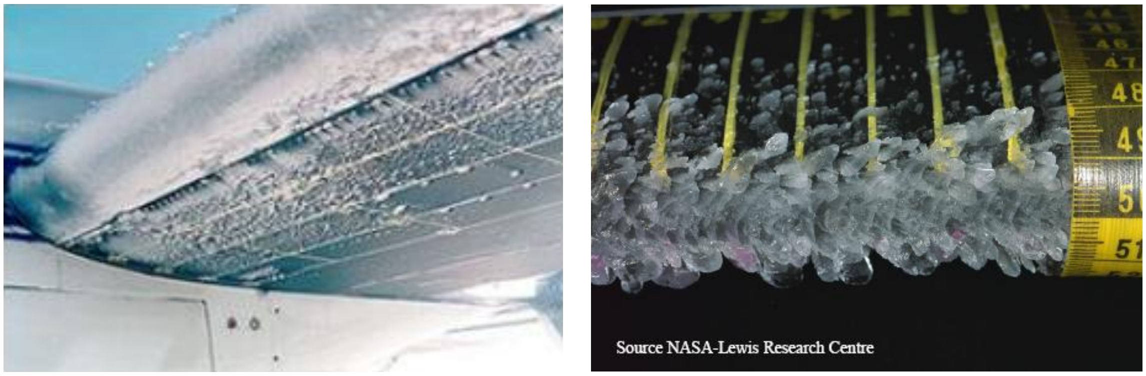

Source NASA-Lewis Research Centre

Figure 1-2: Rime ice (left) and glaze ice (right)

Beside the risks of decreasing pilots' visibility and putting in jeopardy the efficiency of the aircraft radar, communication antennas and probes (cf. Figure 1-3), in-flight icing can considerably affect the aerodynamic as well as control and stability performances of the aircraft.

Figure 1-3: Additional non-negligible side effects of in-flight icing

Droplets impinge on the exposed surfaces of the aircraft and freeze, increasing surface roughness and inducing early boundary-layer transition to turbulent flow. Ice accretion also leads rapidly to increased drag, decreased lift (cf. Figure 1-4), with a corresponding increase in stall speed and decrease in stall angle which constitute propitious conditions for flow separation and stall even at sometimes significantly lower angles of attack [5, 7, 9, 11], especially in the maneuver, holding, take-off and landing phases. It will also modify the pressure distribution and the load dispatch, induce vibrations and decrease the aircraft's maneuverability. In-flight icing is also an issue for engines and propellers, degrading performances, blocking inlets, and possibly damaging in case of ice ingestion.

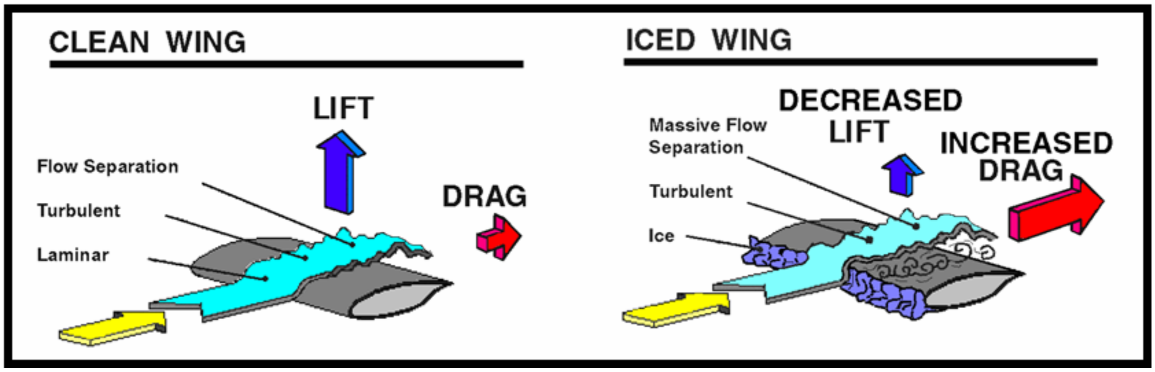

Figure 1-4: Aerodynamic effects of in-flight icing

1.2 In-Flight Icing Protection: Anti-Icing/De-Icing

To avoid such events, aircraft are equipped with systems to prevent ice accretion on the exposed critical aerodynamic and control surfaces during flight. These anti-icing systems must comply with flight safety regulations outlined by national certification authorities such as the FAA [5-6, 12] (Federal Aviation Administration), the EASA [13] (European Aviation Safety Agency) and Transport Canada [14], or other governmental entities [7-9].

As opposed to ground icing, which can be visually checked and taken care of on the runway, in-flight icing requires rigorous procedures and systems to address flight safety regulations outlined by national certification authorities. Such systems include ice detection systems coupled to ice protection systems (de-icing or anti-icing systems), usually located at the leading edge of the exposed surfaces. De-icing systems are reactive and commonly consist in mechanically deformable membranes or electro-impulse devices. Such systems are used periodically to remove already accreted ice. Anti-icing systems, such as hot-bleed-air circulation systems or electro-thermal devices, are preemptive and designed to prevent ice accretion by evaporating the impinging droplets.

One of the most widely used anti-icing devices for wings, stabilizer and engine nacelles of commercial and corporate turbofan engine aircraft is a *high-temperature* *bleed-air anti-icing system*, commonly called *Piccolo tube*. This system circulates hot-air, collected from the engine's first compressor, to the areas to be protected.

1.3 Experimental and Numerical In-Flight Icing

The physics of in-flight icing have been greatly investigated and are increasingly understood, but not yet totally elucidated. Numerical models have been developed to compute ice accretion, evaluate the consequent performance degradation, study and design anti-icing systems and evaluate their efficiency and performance throughout the in-flight icing envelop. In-flight icing software were usually focused on the external aspect, meaning the external flow, droplet impingement and computing the ice accretion, all this mostly in 2D. Some additional features like coupling with bleed-air systems internal flow or with electro-thermal anti-icing were developed to further study the anti-icing aspect itself. The new generation of software, like FENSAP-ICE, has the capability to handle 3D complex geometries in a coupled way with all external flow, droplet impingement, internal flow, heat conduction and ice accretion thermodynamics, in the case of steady or unsteady ice accretion.

On the one hand, flight-testing in natural icing conditions is expensive, and difficult to run since it is dangerous and not all conditions outlined in the FAA's FAR (Federal Airworthiness Regulations) Part 25 Appendix C [12] or the EASA's CS (Certification Specifications) Part 25 Appendix C [13] can be reproduced. On the other hand, icing-wind-tunnel-testing is costly and somewhat limiting. Both approaches are suitable for analyzing a system but can hardly be used as a design platform. Therefore, it is logical to benefit from CFD to model and optimize anti-icing systems, before they are built and tested.

Nevertheless, fully-coupled 3D simulations including 3D external flow, corresponding water impingement and ice accretion, 3D conduction through the skin and 3D internal flow coupled using Conjugate Heat Transfer (CHT), are quite demanding in terms of computing resources. As a result, exploring the design space to come up with an optimal design, which would require a large number of CFD simulations, would not be cost-effective in an industrial framework.

As the number of design variables is relatively high and their combination leads to a large variety of configurations, the design space is wide and possesses several local extrema. In such conditions, classic gradient-based optimization methods are inefficient and most often get stuck in local extrema.

In order to study the sensitivity of anti-icing power to geometric parameters of the Piccolo, a substantial number of CFD simulations of the 3D external and internal flows need to be conducted. The size of meshes being relatively large, this demands quite important computational resources.

1.4 Objective of the Current Work

It is important to consider that safety has a significant cost. Indeed the amount of air bled from the engine for ice protection, along with conditioning and cabin pressurization can represent 5% to 10% of the core engine mass flow [15], half of which is for anti-icing purpose alone [16]. Additionally, bleed-air collection induces engine performance penalties such as increase of specific fuel consumption, power loss and increase in turbine gas temperature [15-16]. The high bypass ratios and the ever-smaller core engine sizes of the modern turbofan engines make it crucial to maximize anti-icing system efficiency in order to minimize the amount of necessary bleed air.

The present work's motivation is thus to develop a Piccolo tube optimization methodology, with the idea of firstly uncoupling the problem to limit its size, secondly using a Reduced-Order Model (ROM), such as Proper Orthogonal Decomposition (POD), to limit the number of necessary computations, and thirdly applying an evolutionary optimization approach, such as Genetic Algorithms (GA), to efficiently search the wide multidimensional design space. This approach focuses, in the context of this Master's research project, on single objective optimization based on geometric parameters. The associated models are 3D CFD-based and include solving for water runback.

This work will first introduce the state of the art of bleed-air anti-icing systems study, then present the optimization methodology and the different models, next provide test case results, and finally draw conclusions and outline some recommendations for future work.

2. STATE OF THE ART

2.1 Physical Models

In-flight icing and anti-icing topics are widely addressed in the literature. The physical models dealing with ice accretion and water film runback phenomena are usually based on a Messinger-type control-volume-based finite difference scheme [17-24] and possibly including the anti-icing aspect [25-35]. These icing simulations are run using commercial, in-house or research icing codes like LEWICE [10, 36], ICECREMO [23, 26], ANTICE [37] or CANICE [31-34, 38-39] which rely on CFD computations using CFD commercial or in-house codes to get the external flow and/or water droplet impingement solutions. Fully integrated CFD/Icing packages also exist, such as FENSAP-ICE [40-46], which even provides a Conjugate Heat Transfer (CHT) framework to execute fully coupled[1] in-flight icing computations to simulate anti-icing systems.

2.2 Aircraft In-Flight Anti-Icing Systems

Some of the anti-icing studies focus on electro-thermal anti-icing systems [26-30, 32-33, 37, 47-48] which are usually easier to implement since for all practical purposes the problem can be reduced to 2D and the anti-icing heat flux distribution is directly applied as a wall boundary condition.

In this work, the attention is focused on the study of hot-bleed-air anti-icing systems which are widely covered in the literature [15, 25, 31, 34, 36, 38-39, 42, 45, 49-65].

Current methods include 2D icing CFD-based uncoupled simulations in "wet air"[2] conditions which rely on heat transfer coefficient correlations to represent the internal flow [25, 31, 34], 2D uncoupled CFD simulations of the 2D internal flow [39] and 2D icing CFD-based coupled simulations, using CFD to compute the internal flow, in "dry air" [54] and "wet air" [38] conditions.

2.5D[3] icing CFD-based coupled simulations in "wet air" conditions, using CFD to compute the internal flow, is mentioned in [36].

---

[1] The term "coupled" refers to the fact that external flow and internal flow solutions are computed in a coupled manner, usually through CHT, with or without considering the conduction within the skin.

[2] As opposed to "dry air", "wet air" means that the LWC is non-zero and thus implies solving for droplet impingement, water runback and ice accretion.

[3] 2.5D stands for solving external and internal flows in 3D and computing water runback and ice accretion in a two-dimensional manner.

3D icing CFD-based coupled simulations, using CFD to compute the internal flow, were also covered in “dry air” [45, 50, 53-55] and “wet air” conditions [42].

Most of these studies compared their results against experimental icing tunnel test results or against other computational results obtained with different codes.

Also, experimental [57, 61, 63] and computational [15, 58, 60, 64] investigations and parametric studies of hot-air anti-icing systems were carried out to evaluate the efficiency and performance of such systems, investigate their sensitivity to in-flight icing conditions and Piccolo tube geometric and thermodynamic parameters, and examine their behavior to off-design conditions.

2.3 Impinging Jet Flow

The study of heat transfer from an impinging jet onto a surface is also a well-addressed topic. The local Nusselt number is recovered either from heat/mass transfer analogy using the sublimation of a volatile chemical like naphthalene at the wall, or from the temperature distribution when imposing a constant and uniform heat flux via a thin metallic foil covering the surface. The main objective of such studies is usually to investigate experimentally and/or numerically the impact of certain parameters such as the jet Reynolds number, the normal distance from hole to surface, the jet diameter and the radial distance from the jet stagnation point, on the heat transfer to the wall, in order to elaborate a correlation for the average Nusselt number.

For this purpose, experimental studies of a single impinging jet on a flat plate are done [66-71]. Also, parametric investigations about staggered impinging jet arrays on a flat plate were addressed experimentally and/or numerically [72-74], including the effect of the jet-to-jet spacing on the Nusselt number [72, 74].

In order to get more specific to the Piccolo tube anti-icing system geometry, 3D numerical studies of the flow and heat transfer of an hot-air impinging jet array on a concave surface were proposed [52, 75].

Moreover, experimental and numerical studies were engaged directly on hot-air anti-icing systems to obtain Nusselt number correlations. Brown *et al.* [49] ran experimental investigations on a nacelle inlet hot-air anti-icing system model, a three-row staggered jet array Piccolo tube, and proposed an average Nusselt number correlation independent of the normal distance from hole to surface.

Planquart *et al.* [59] presented an experimental and numerical study on a wing slat three-row staggered jet array Piccolo tube, using infrared thermography combined with the heating foil method to recover the thermal exchange coefficient distribution.

The experimental data is used to obtain a Nusselt number correlation and to validate the corresponding numerical simulations.

Wright [65] presented a review of Nusselt number correlations for three-row staggered jet Piccolo tube application. The aim of the study was to do an evaluation of the jet impingement heat transfer correlations by integrating them to anti-icing numerical simulations and validating against experimental data in "wet air" conditions.

2.4 Anti-Icing Systems Optimization Methodology

Up to this point, the optimization as such of anti-icing systems was not addressed and is not widely represented in the literature; quite the contrary.

Wang *et al.* [48] proposed a thermo-fluid optimization methodology to improve the de-icing strategy thermal effectiveness of an electrically-heated intake scoop of a helicopter engine cooling-bay inlet. The optimization method involved the Latin Hypercube Design of Experiments (DOE) method, the Boender-Timmer-Rinnooy-Kan (BTRK) clustering algorithm coupled with an adaptive-response-surface-based reduced-order model method. The methodology was able to handle up to four geometric parameters and one thermodynamic parameter as design variables.

Concerning hot-bleed-air anti-icing systems, there are two particularly relevant articles of great insight in terms of optimization methods.

Santos *et al.* [76] performed a sensitivity analysis on a 6-parameter internal flow correlation that was coupled with external flow, droplet impingement and ice accretion 2D solvers. The sensitivity analysis methodology was performed to reveal the most significant geometrical and operational parameters of the hot-bleed-air anti-icing system in order to provide guidelines for parametric optimization. This methodology, which does not strictly speaking constitute an optimization procedure, relies on a Sobol design of experiments procedure and a response-surface-based reduced-order model method. It was able to handle four geometric parameters and two thermodynamic parameters as design variables.

Last but not least, Saeed and Paraschivoiu [77] used a Micro-Genetic-Algorithm optimization code to determine the optimum Piccolo tube configuration for a given range of flight and icing conditions. The methodology relied on an internal flow 2D correlation coupled with the 2D icing code CANICE and managed two independent geometric parameters and one thermodynamic parameter as design variables. The problem is set like a multi-objective optimization problem with two icing parameters and three flight parameters defined within a chosen in-flight icing envelop. Their preliminary results suggested that the genetic-algorithm-based optimization had a great application potential for the design of hot-air anti-icing systems.

These references were of great interest and inspiration for the elaboration of the optimization methodology presented in this work.

The present work’s optimization methodology is pushed further by incorporating the 3D external flow CFD solution and an internal flow 3D CFD-based correlation to a Messinger water film model, with the possibility to integrate higher fidelity solutions, and by combining “classic” (as opposed to micro) genetic algorithms and POD-based reduced-order model and managing up to five independent geometric parameters as design variables.

3. OPTIMIZATION METHODOLOGY

3.1 Parameterization

3.1.1 Geometry of the System

The 3D swept constant chord wing model and the wing slat Piccolo tube anti-icing system used in this work, shown in Figure 3-1, are generic models provided by Bombardier Aerospace [78], which have not been used on any of its aircraft but for which experimental data has been obtained. A cut of the Piccolo tube inside the wing slat is shown in Figure 3-2. In this study, only the smooth configuration is considered, i.e. the slat is not deployed.

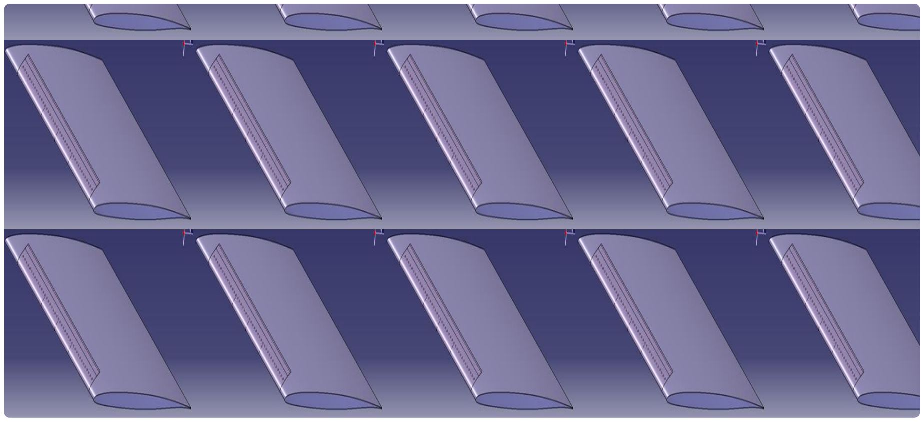

Figure 3-1: 3D generic constant chord swept wing.

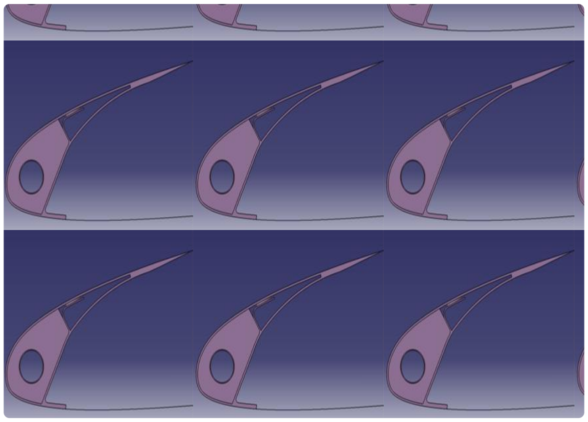

Figure 3-2: Piccolo tube section on the wing slat in smooth configuration.

The Piccolo tube is an integrated system mainly composed of a tube located inside the leading edge of the wing, guiding the bleed air collected from the engine's first compressor. This tube is perforated with a number of rows (usually two or three, in this case two) of small holes, usually disposed in a staggered manner, oriented to blow the hot air onto the wing's leading edge inner skin surface, as shown on a close-up of the anti-icing system in Figure 3-3. The function of the Piccolo tube is primarily to heat up the skin so as to evaporate most of the impinging water droplets, and thereby prevent dangerous ice accumulation on the wings.

Fixing and arranging the geometry are important steps in order to be able to properly generate the CFD mesh, smoothly run the CFD computation, and get accurate results. The adjustments on the geometry aim to keep only the relevant features while discarding unnecessary complexities. Also, the quality of the surfaces' definition, when importing from the virtual design definition process to the mesh generation process, is crucial. Indeed, as the mesh is projected onto the CAD (Computer Aided Design) surface, a low quality definition or "kinky" surface will lead to bad quality mesh. This is all the more critical in this particular case where heat fluxes and flow variables are to be extracted at the wall.

3.1.2 Parameterization of the Problem

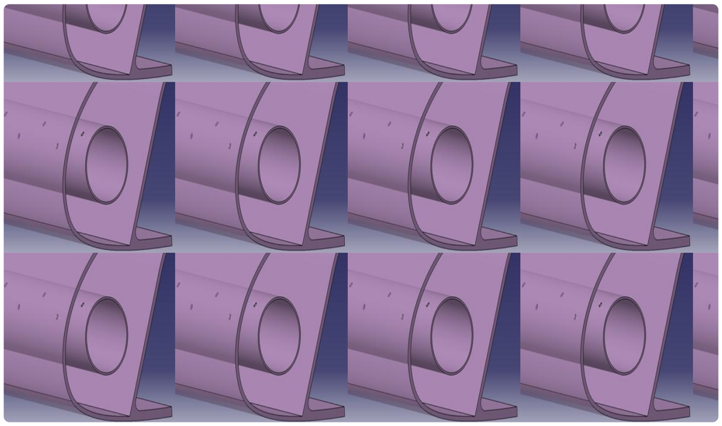

Figure 3-3: Piccolo tube geometric configuration.

In the perspective of single-objective optimization, the proposed approach considers a single in-flight icing condition which is a combination of a flight configuration (ambient pressure, air speed, angle of attack) and icing conditions (ambient temperature, liquid water content, droplets size). This particular in-flight icing condition is based on maximum total catch rate in the case of the Appendix C 45-minute holding, as it is considered as one of the most adverse design points. The above parameters, along with the corresponding constrained available anti-icing power for holding flight regime (bleed air mass flow, total pressure and temperature levels) were chosen as a generic, yet realistic, design point and were provided by Bombardier Aerospace.

As a proof of concept, five geometric parameters were considered as design variables, as shown in Figure 3-4:

- the Piccolo tube horizontal and vertical positions inside the slat:

  $20\ mm \leq X_{Pic} \leq 30\ mm$ and $-1.5\ mm \leq Y_{Pic} \leq 8\ mm$
- the jet orientation angle for each of the two rows:

  $\{-60° \leq \theta_1 \leq 0°$ and $0° \leq \theta_2 - \theta_1 \leq 45°\}$ or $\{-45° \leq \theta_{mean} \leq 30°$ and $\Delta\theta = 30°\}$
- the spacing between adjacent jets: $25\ mm \leq c \leq 75\ mm$

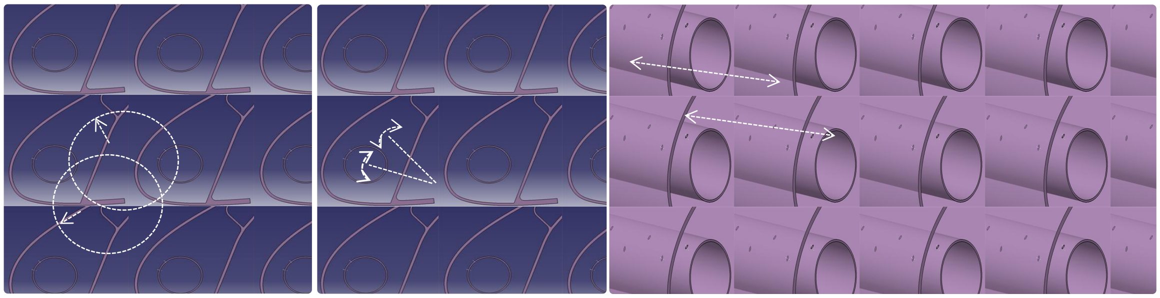

Piccolo tube location Jets orientation Spanwise jet nozzle spacing

Figure 3-4: Geometric parameters.

The Piccolo tube diameter, number of rows, and the Piccolo holes diameter were fixed. Concerning the Piccolo thermodynamic parameters, the jet air temperature and total pressure as well as the available mass flow were also given. In this study, the thermodynamic parameters will not be considered as design variables, even though their impact on the anti-icing heat transfer is great, since they depend on the flight phase or more precisely on the engine regime.

Concerning the handling of several design points (external conditions), the method can still be applied with an adaptation of the objective function to account for the additional constraints or with the construction of a Pareto front in a multi-objective optimization framework [79].

3.2 Optimization Methodology

3.2.1 Overview

In the context of numerous design variables and therefore extended multidimensional design space, optimization faces challenges in terms of feasibility and cost-effectiveness, especially when 3D CFD coupled simulations are involved. In the particular case of Conjugate Heat Transfer (CHT) coupled with icing and 3D CFD, solving the fully coupled problem is not feasible in an industrial context. It would also necessitate re-computing the external flow each time which in the current case of single-objective optimization would be unnecessarily redundant.

Therefore the present methodology proposes to uncouple the problem, thus computing the external flow only once and solving the internal flow and water film for each design. The conduction normal to the metal skin will be neglected.

The size of the multidimensional design space would require the use of an evolutionary research algorithm which will still necessitate a relatively high number of computations. To decrease both the computational cost and the number of computations, the present methodology proposes the use of a reduced-order model (ROM).

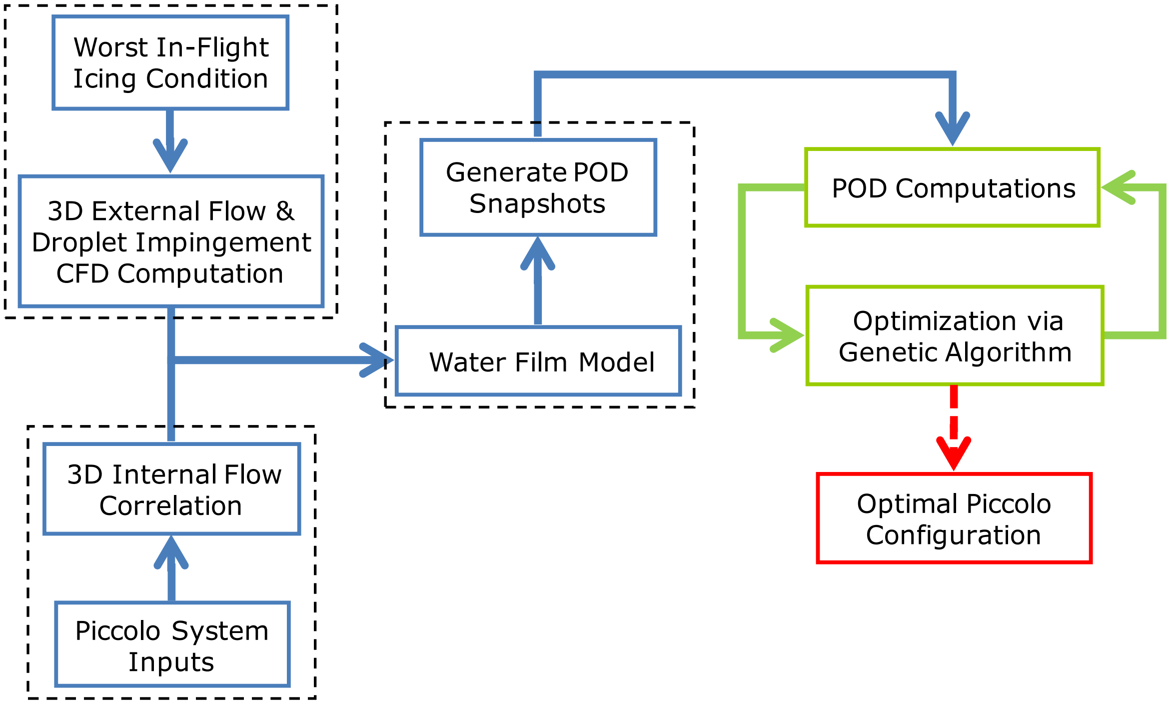

Figure 3-5: Optimization methodology diagram.

The optimization methodology is illustrated in the diagram of Figure 3-5. It is designed in a modular fashion to allow easy upgrading of any module independently. The top left module refers to the external flow simulation. Using the single set of identified worst-case in-flight icing condition, the 3D external flow and associated droplet impingement solutions are computed. The bottom left module refers to the internal flow simulation. Given the Piccolo system inputs, the 3D internal flow is computed and provides the corresponding anti-icing heat transfer coefficient distribution. Combining these entries into the water film model module, a water runback solution is computed. A set of water runback solutions, spanning the different sets of design variables, is pre-computed to constitute the snapshots database of the POD (Proper Orthogonal Decomposition) module. The optimization core of the methodology, here in green on the diagram, is composed of a Genetic Algorithm (GA) module coupled with a POD-based ROM module.

The methodology was embedded in MATLAB, integrating the modules in a main routine, calling for the different modules coded in MATLAB or in FORTRAN, and managing the input and output files.

A description of these modules as well as the different models used in the methodology is presented in the next sections.

3.2.2 Genetic Algorithms

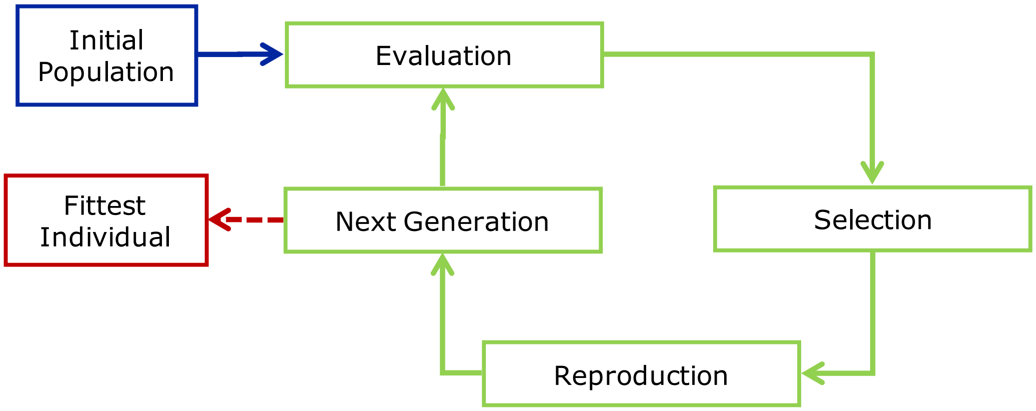

Figure 3-6: Genetic algorithms procedure.

Genetic Algorithms (GA) are already widely used as single- or multi-objective global optimization strategies involving CFD [80-82]. It is frequently coupled with interpolation techniques, such as Kriging [79, 83-86], especially in the case of large multidimensional design space, where they perform better than other optimization methods [87] (namely gradient-based methods). In this project, the GA module of the MATLAB optimization toolbox was used.

GA used as optimization tools were inspired by evolution and natural selection theories which advocates the survival of the fittest *individual*. The term *individual* refers here to a particular set of design variables, encoded (usually in binary format) as a chromosome, whose genes refer to each design variable. From an initial group of *individuals*, referred as the *population*, some of the best *individuals* are *selected* according to their *fitness* in order to perform *reproduction* which gives birth to a new *generation* [88-92]. This recursive procedure is repeated until convergence, leading to the fittest *individual*, i.e. the global optimum, as illustrated in Figure 3-6.

An important point concerning the use of this method is to maintain a certain degree of *diversity* inside the population to avoid converging towards local extrema, while limiting the *population* size and number of *generations* to get reasonably fast convergence [93]. For this purpose, the different parameters of the GA have to be carefully selected.

- The evaluation of *individuals* through the *fitness* corresponding to objective (or cost) function is reinterpreted as *selection* proportionality rate by a *fitness* scaling, usually defined as proportional to the *fitness* or rank-based in the case of a "flat" objective function.
- Concerning the *selection* method, the roulette wheel is considered a "fair" selection algorithm (choosing the *parents* randomly with a probability rate proportional to their *fitness*), whereas the tournament (choosing each *parent* as the best *individual* out of a small set of randomly chosen *individuals*) is a more local method in the sense that it better preserves diversity (less chance to fall in a local minimum but usually longer to converge).
- In terms of *reproduction*, the cross-over method is the most commonly used. It consists in exchanging parts of the *chromosomes* of the *parents*. A multiple-point cross-over implies bigger difference between *parents* and *children* than single-point, thus providing wider diversity (again at the cost of longer convergence). The elite option enables to preserve the "history" of the fittest *individuals*. The cross-over fraction is usually set between 70% and 90%, the remaining is obtained by *mutation* (random bit changes within the *chromosome*), in addition to the fittest *individuals* introduced by the elite option. Note that increasing *mutation* would ensure a higher diversity level, which is essential in the case of a small *population* size. Ideally, it would be beneficial to have a higher *mutation* rate for the first *generations* and a decreasing rate towards the last *generations*.
- The resolution is also an important parameter. It depends on the size (number of bit) of the *chromosome*, more precisely the size of each *gene*, and the width of the corresponding variable interval.
- The more complex the *fitness* function, the bigger the *population*, with eventually higher *mutation* rate to limit *population* size.
- It can be interesting to use *subpopulations* (each *evolving* separately), especially in the case of multiple-optima *fitness* functions. In this case, *niching* is a way to increase diversity (since it preserves local *ecosystems*), and *migration* allows some mixing between *subpopulations*.

In this work, the GA module was configured in the following manner. The tournament selection method was chosen with proportional fitness scaling. The reproduction method relies on a single point cross-over fraction of 75% (and thus a 25% mutation rate) and an elite count of two. The population size is 20 (respectively 25 and 30) for three (respectively four and five) design variables. No subpopulations were used. The number of generations was set to 50.

Generally, a GA *population* of 30 *individuals* for 50 *generations* leads to 1500 *evaluations* and thus 1500 associated computations. In order to run the optimization loop in reasonable time, the optimization procedure relies on POD-computed solutions to explore the wide multidimensional design space. Indeed, using fully 3D CFD computation for the internal flow and water film model requires 30hrs per run. Replacing the 3D CFD internal flow computation by a 3D heat transfer coefficient correlation requires about 5mins per run, whereas using POD brings the computational time down to 15s per run.

Familiarization with GA was accomplished by solving for the Brachistochrone problem with a simple GA code and using B-spline control points as variables. This was done to have a better understanding of the different GA parameters, as well as how to express the constrained design variables and choose the objective function.

3.2.3 Objective Function

In order to compare individuals, the genetic algorithm procedure involves *evaluating* each of them by means of an objective function (or "cost" function) closely related to the intrinsic specifications of the system. In the case of a thermal anti-icing system, the aim is ideally to achieve the evaporation of all the impinging water, on both upper and lower surfaces, within the heated area. It means that there should be no water running back past the limits of the heated zone. It is possible that more than one configuration could lead to fully evaporative conditions. In such case, the most energy efficient configuration would be chosen, i.e. maximizing the actual transferred anti-icing power ($\dot{Q}_{anti-ice}$) to potential total anti-icing power ($\dot{Q}_{ref} = \dot{m}_{Piccolo} \cdot c_p \cdot \left(T_{Piccolo} - T_\infty\right)$) ratio and thus the objective function would be:

$$ObjFct = \left(\dot{Q}_{anti-ice} - \dot{Q}_{vap}\right) \big/ \dot{Q}_{ref} \tag{1}$$

In practice, this "globally fully-evaporative" condition may be quite difficult to fulfil on both upper and lower surfaces and may necessitate an over-designed energy requirement. In such case, especially if the given potential total anti-icing power is inadequate to achieve globally fully-evaporative in any configuration, then another more realistic and practical criterion can be used. This criterion could be defined as follows: fulfil fully-evaporative conditions on the upper surface and ensure minimal runback on the lower surface. Using this new criterion, the optimization goal is reformulated:

> *From given available anti-icing power, minimize the water runback on the lower surface of the slat while enforcing fully-evaporative condition on the upper surface, within the range of the design parameters.*

Therefore, the cost function is defined as the global wasted power to global available power ratio (where the wasted power is simply the power that was not used for evaporation purpose), in the case of running back or partially evaporative configurations:

$$ObjFct = \left(\dot{Q}_{ref} - \dot{Q}_{vap} \cdot e^{-p}\right) \Big/ \dot{Q}_{ref} = 1 - \dot{Q}_{vap} \cdot e^{-p} \Big/ \dot{Q}_{ref} \qquad (2)$$

This expression of the objective function is chosen to be more consistent with partially evaporative configurations, with additional penalty in the presence of runback out of the protected zone on the upper surface. The penalty term *p* is expressed as a function of the mass flow rate of upper surface runback.

$$p = 10 \cdot \sqrt{\dot{m}_{rb\,out}^{upper} \Big/ \dot{m}_{\beta}^{total}} \qquad (3)$$

Another way to look at it is to directly consider the amount of wasted energy at the anti-icing system exhaust:

$$ObjFct = \left(\dot{Q}_{ref} - \dot{Q}_{exhaust}\right) \Big/ \dot{Q}_{ref} = \dot{m}_{Pic} \cdot c_p \cdot \left(T_{Pic} - T_{exhaust}\right) \Big/ \dot{Q}_{ref} = \left(T_{Pic} - T_{exhaust}\right) \Big/ \left(T_{Pic} - T_{\infty}\right) \quad (4)$$

This is actually the inverse of the global thermal efficiency defined by de Mattos and Oliviera [50]. This last cost function definition is actually very close to the actual transferred anti-icing power to potential total anti-icing power ratio ($\dot{Q}_{anti-ice} \Big/ \dot{Q}_{ref}$) defined earlier since the reference available anti-icing power can be expressed as $\dot{Q}_{ref} = \dot{Q}_{anti-ice} + \dot{Q}_{exhaust} + \dot{Q}_{loss}$ where the losses are reduced to zero if the rear walls of the slat are considered adiabatic. However, this way of expressing the objective function was not used since it did not explicitly contain the key aspect of water evaporation.

Note that earlier into the project, the cost function was defined as:

$$ObjFct = \sqrt{\left(\dot{Q}_{anti-ice} - \dot{Q}_{ideal}\right)^2} \qquad (5)$$

In this expression, $\dot{Q}_{ideal}$ would be the ideal target anti-icing heat flux distribution. However, $\dot{Q}_{ideal}$ does not have an analytical expression and it would therefore be an optimization problem itself to find such distribution. This would correspond more closely to the way to proceed in the case of the electro-thermal type of anti-icing. A few attempts were made using genetic algorithms on the parameters of analytic distributions like piecewise continuous, quadratic, Gaussian and double-Gaussian. These attempts were however not very conclusive, so $\dot{Q}_{ideal}$ was then considered as the "locally fully evaporative" distribution, meaning enforcing instantaneous evaporation of incoming water. Within the impingement zone, the local temperature level would correspond to the local amount of impinging water to be evaporated. Outside, the anti-icing heat flux would be either considered null or corresponding to a wall temperature of 0°C. Actually, not only the heat flux distribution is compared to the ideal one, but also the temperature level, especially with regards to the evaporation process which is mainly dependent on temperature.

Unfortunately, the anti-icing heat flux distribution obtained with a Piccolo tube is not at all uniform like the ideal one would be, which makes this choice of cost function unsuitable in this case. Indeed, even though having an anti-icing heat flux distribution as uniform as possible would be desirable, it would not be achievable with such an anti-icing system.

3.2.4 Proper Orthogonal Decomposition

Reduced-Order Modeling, such as Proper Orthogonal Decomposition, has already been applied in the field of CFD [94-98] and is increasing in popularity, especially in the context of CFD-based optimization [99-101]. The main idea is to greatly decrease the computational cost of a CFD solution by decreasing the number of degrees of freedom of the system to be solved, keeping the order of accuracy of the models identical. POD aims to reconstruct an intermediate target solution from a set of previously computed high fidelity solutions, referred to as set of snapshots.

The distribution of the snapshots within the design space has a great impact on the performance of POD. Indeed, the Reduced-Order Model constructed from the set of snapshots can only reproduce the physical features inherent to the database. Physics that would not be present in the snapshots would not appear in the target POD computation. Therefore, the snapshots must be chosen with care and judiciously distributed over the design space in order to enforce a more diverse combination of the parameters and avoid or reduce unnecessary redundancy in the physical features captured by the snapshots. For this purpose, the Lp-τ space filling method [102-107] was used since it ensures both uniformity and dispersion of the sampling. A supplementary and useful feature of the Lp-τ method is that if additional design points are required, they will simply be added to the already computed list of snapshots, avoiding computing again the entire set of solutions. In this work, a set of 120 (160 and 200, respectively) snapshots was computed for the 3-design-variable case (4- and 5-design-variable cases respectively). Each of these sets of snapshots was judiciously distributed over their corresponding design space using the Lp-τ method.

Once a suitable database of snapshots is selected and acquired (in this case, the wall temperature and the water runback mass flow rate distributions from the water film model, cf. Appendix C), the snapshots can be decomposed into a linear combination of "basis functions" or "eigenfunctions" and associated coefficients (cf. Equation (6)).

$$U_j = \sum_{i=1}^{ns} \alpha_{ij} \cdot \Phi_i \qquad (6)$$

These basis functions are extracted by means of the POD method [108-111], from the eigenvalue problem associated to the cross-correlation matrix of the combined snapshots, which indicates how the snapshots are correlated to one another. Solving the eigenvalue problem provides an eigenvalue-eigenvector pair for each mode, sorted from highest to lowest in terms of energy content, the principal features being contained into the most energetic modes. Thus, the first 10 or 15 modes (corresponding to normalized energy contents higher than 10^{-5} and a cumulative energy content of 99.9% or even 99.99%) would usually suffice to obtain the target computed solution, decreasing again to some extent the computational cost. There are as many modes as the number of snapshots considered by the POD model.

As the vector space spanned by the basis functions is orthonormal by definition, each coefficient is simply the dot-product of the corresponding eigenfunction with the corresponding snapshot itself.

The target solution can also be expressed as a linear combination of the basis functions, as shown in Equation (7). Among the different existing methods to obtain the corresponding target coefficients, interpolation methods constitute certainly the cheapest and most effective ones. In the present case, the Kriging interpolation method [79, 83-86] was used for its strong capacity to handle multidimensional space.

$$\hat{U} = \sum_{i=1}^{nm \leq ns} \hat{\alpha}_i \cdot \Phi_i \qquad (7)$$

In this work, the current ROM module is based on the previous work of McGill University CFD Laboratory Masters students Kunio Nakakita [112-113] and Vladislav

Lappo [114-115]. Additional features were implemented in order to improve the speed and to some extent the accuracy. These features can be identified as local-POD – local-Kriging. The idea is to select a lower number of snapshots but of higher relevance to build the POD model and compute the target solutions.

The Kriging model is not based on a deterministic approach and it could in some cases encounter difficulties managing a high number of snapshots (about 80 and over in this particular case of interpolating temperature and water runback flow rate distributions). This would also motivate the choice of the local features.

The initial "global" POD-Kriging model would build the POD model out of the entire set of snapshots and then would interpolate the target coefficient with Kriging also using the coefficients from the entire set of snapshots. This POD-Kriging version would perform poorly below 40 snapshots and achieve best cost-effective performance for about 50 to 60 snapshots. In this case, the snapshots are the "global" ones, i.e. following the order of the list provided by Lp-τ.

The first variant can be identified as global-POD – local-Kriging. This feature allows reducing the "pollution" of the target solution with irrelevant features contained in remote snapshots as well as decreasing the load on the POD and the interpolation modules, by considering a certain set of closest snapshots instead of the entire set to interpolate the POD coefficients for each target solution. Therefore, out of a data set of about 55 snapshots, 15 to 20 target-dependent closest snapshots would be chosen to achieve Kriging interpolation.

The second and more adequate variant is the one currently used in this work and can be identified as local-POD – local-Kriging, as illustrated in an example for two-dimensional design space in Figure 3-7. The blue dots represent the snapshots, uniformly distributed over the design space using the Lp-τ space filling method. The red dot represents the target solution to be computed with POD. The POD model is then built from a set of closest snapshots, represented as the black dots within the black circle. Again, this is done in order to reduce the "pollution" of the target solution with irrelevant features contained in remote snapshots, decrease the load on the POD module and gain in speed without compromising the accuracy. The target's linear combination coefficients are then interpolated using Kriging from a possibly even closer set of snapshots, represented as the green dots within the green circle in Figure 3-7. Again, this is done in order to get a more coherent solution with respect to the neighbouring snapshots by reducing the range and the number of degrees of freedom and therefore ease the interpolation process.

The global set of snapshots can be more substantial to better represent the whole design space, while building the POD model and interpolating with closest snapshots containing the most relevant physical features provides better and more cost-effective results. 40 to 60 snapshots out of the global set would be used as closest set for the POD model, along with 15 to 20 even closer snapshots (within the 40) for the Kriging interpolation.

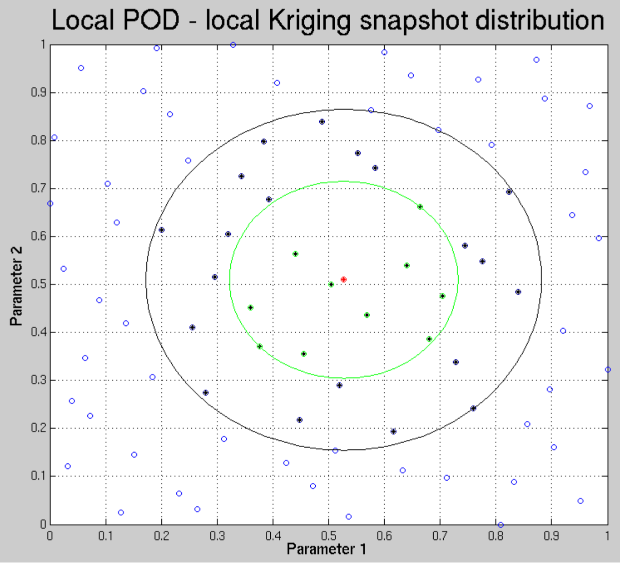

Figure 3-7: Illustration of the concepts of local POD and local Kriging in 2D.

The POD-Kriging module is called by the Genetic Algorithm module in order to quickly and efficiently compute the objective function for each individual of each generation:

$ObjFct^{POD} = 1-\dot{Q}^{POD}_{evap}/\dot{Q}_{ref}$ or $ObjFct^{POD} = \left(\dot{Q}^{POD}_{Anti-ice}-\dot{Q}^{POD}_{evap}\right)/\dot{Q}_{ref}$ with $\dot{Q}^{POD}_{evap} = \dot{m}^{POD}_{evap}\cdot L_{vap} = \left(\dot{m}_{\beta}-\dot{m}^{POD}_{rb}\right)\cdot L_{vap}$ and $\dot{Q}^{POD}_{Anti-ice} = h_{c\,\mathrm{int}}\cdot S\cdot\left(T_{Piccolo}-T^{POD}_{w}\right)$.

After having defined the optimization core of the methodology, the following section describes the different models used in the external flow, internal flow and water runback modules.

3.3 Numerical Models

3.3.1 External Flow

In the context of single objective optimization, the external flow and water impingement solution are computed once, for the conditions mentioned in section 3.1.2. The three-dimensional external flow and associated droplet solution were computed on a close to 1.5-million-node structured C-H mesh, solving the Navier-Stokes equations and the Eulerian multiphase flow equations using state-of-the-art

3D CFD simulation tools [46]. Here, the Spalart-Allmaras one-equation turbulence model was chosen.

The fluid domain over the constant chord swept wing is limited at both ends by a periodic boundary plane and surrounded by a far-field boundary condition.

Figure 3-8 illustrates the 3D external flow results computed by FENSAP and the droplet impingement computed by DROP3D.

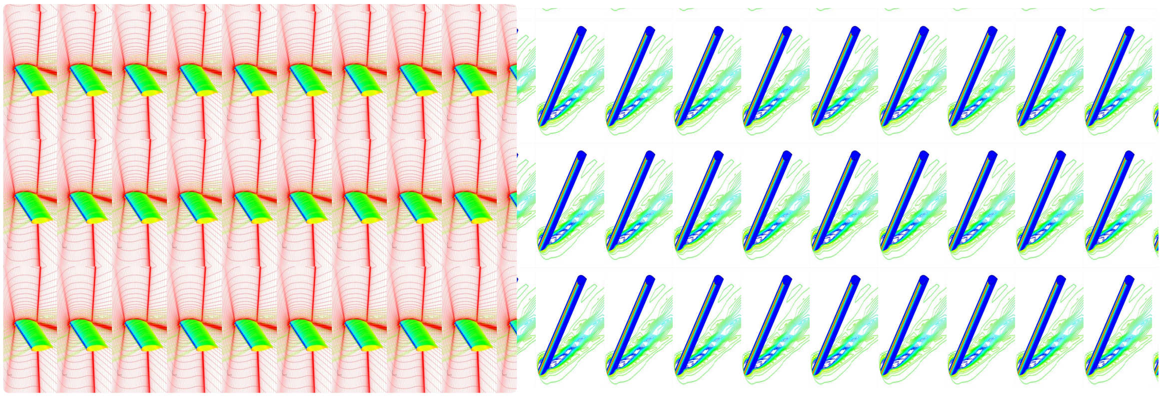

Figure 3-8: 3D flow around swept wing (left) and corresponding droplet impingement (right).

A sensitivity analysis was done, which revealed weak dependence of the relevant flow variables and particularly of the heat transfer coefficient distribution, to wall temperature boundary condition (cf. Appendix A). Thus, a boundary temperature distribution chosen as the mean value between free stream and Piccolo reference temperatures is imposed on the airfoil exchange surface. This arbitrary boundary condition is chosen in order to ensure the condition T_w-T_{ref} ≥ 40 K for which the impact of wall temperature stays below 1%.

Therefore, external and internal flow computations are uncoupled, meaning that they are computed separately, essentially to reduce the computational cost.

In fact, solving for the complete coupled problem (external flow, internal flow, heat conduction via conjugate heat transfer and ice accretion) within the optimization framework would not be computationally affordable. Convergence for a single run would necessitate about a week on a 64-CPU cluster.

3.3.2 Internal Flow

Figure 3-9 illustrates the 3D internal flow solution, also computed using FENSAP. On the left hand side is the anti-icing heat flux distribution on the slat’s surface. The other two pictures show the internal flow streamlines, which reveal highly three-dimensional flow features.

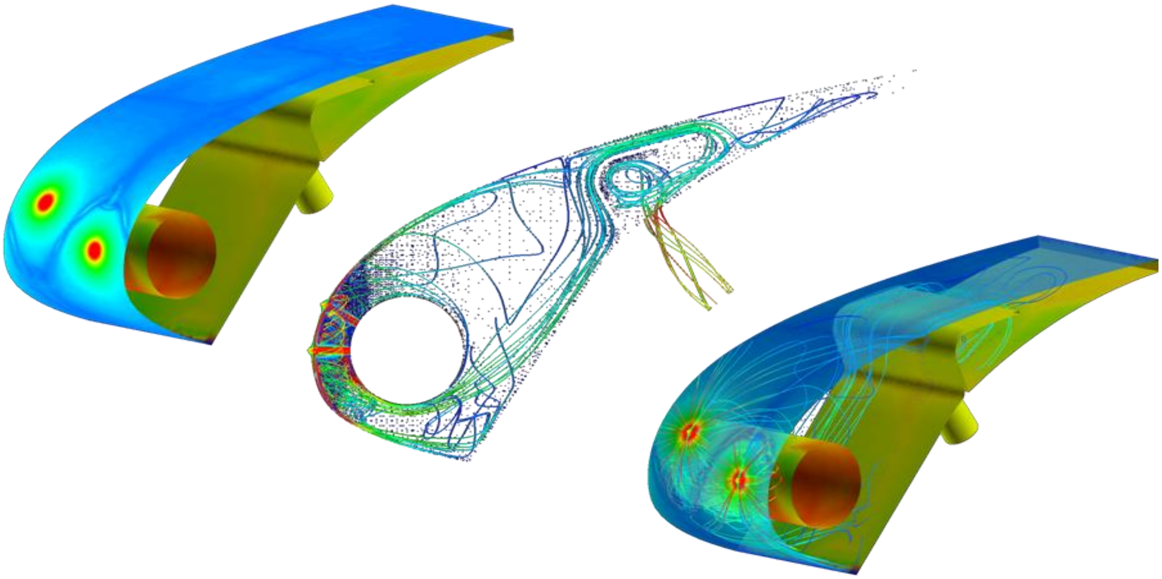

Figure 3-9: 3D internal flow inside Piccolo anti-icing system.

The internal fluid domain is composed of the smallest periodic pattern, delimited on each side by periodic boundary conditions. The meshes used for these simulations contained about 500,000 nodes and were based on tetrahedral elements with prism layers normal to each wall (first layer of one micron in thickness), and density boxes to refine the mesh along each jet.

Some issues arose concerning the setting of boundary conditions. The inlet boundary conditions were imposed as velocity profile boundary condition, calculated from the total pressure and static pressure data. Then, as the pressure level has to be set somewhere in the domain, it was applied as outlet boundary condition. The actual outlet had to be extruded far enough to allow the flow to be properly guided out of the fluid domain, because of convergence problems. Also, the pressure level and mass flow rate had to be matched at the inlets, playing on the outlet pressure.

Concerning the temperature boundary conditions at the walls, the heat exchange surface was treated in the same way as the external surface to ensure minimal impact on the flow, while the remaining walls were treated as adiabatic surfaces.

3.3.3 From 3D Internal Flow Simulation to 3D Internal Flow Correlation

In order to reduce computational time and cost, and given that heat transfer coefficient is the only field of interest extracted from internal flow computations, the costly internal flow 3D CFD simulations were replaced by 3D impinging jet correlations, as shown in Figure 3-10.

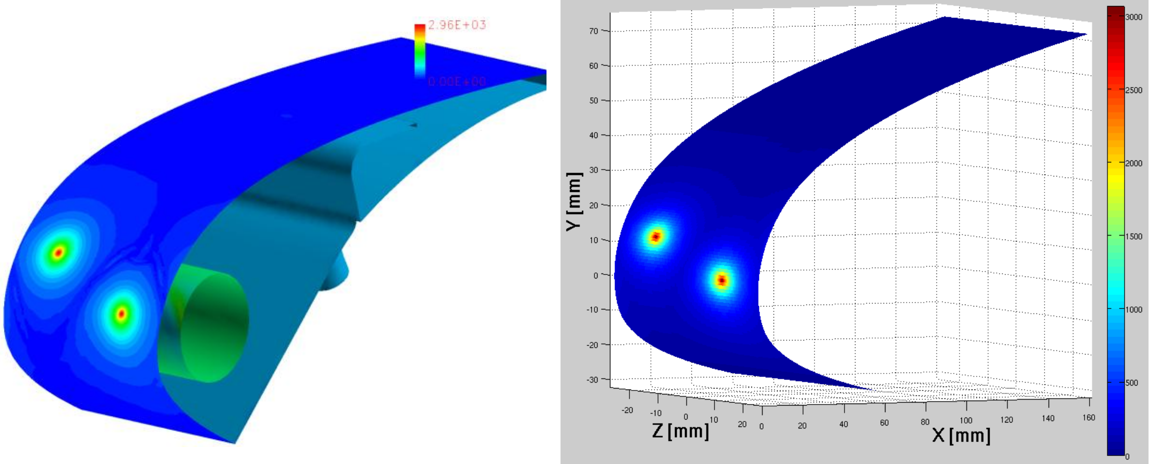

Figure 3-10: Internal heat transfer coefficient distribution from CFD and correlation.

The heat transfer coefficient distribution on the internal skin is obtained, based on an average Nusselt number correlation determined by Goldstein [66]. This strategy was mentioned by Wright [65] and used by Lee [36]. The correlation is presented in Equation (8).

$$\overline{Nu}\Big\|_0^r = \mathrm{Re}^{0.76}\cdot\left(24-\left|\left(z_n/d\right)-7.75\right|\right)\Big/\left(533+44\cdot\left(r/d\right)^{1.285}\right) \tag{8}$$

where Re is the Reynolds number based on the hole diameter d, r is the radial distance from the impinging jet stagnation point on the wall and z_n is the normal distance from the hole to the wall. The correlation was developed for Reynolds numbers up to 124000, normal distances from 6 to 12 hole diameters, and radial distances up to 32 hole diameters. Even though this correlation was developed for a single jet impinging on a flat plate, which is not very representative of the problem at hand, it was one of the very few correlations that could provide the average Nusselt number as an explicit function of the radial distance (cf. [65]).

The local Nusselt number is recovered from the integral definition of the average Nusselt number as developed in the following expressions:

$$\overline{Nu}\Big\|_0^R = 2\big/R^2\cdot\int_0^R Nu_r\cdot r\cdot dr \tag{9}$$

$$\overline{Nu}\Big\|_0^{R+dR} = 2\big/\left(R+dR\right)^2\cdot\int_0^{R+dR} Nu_r\cdot r\cdot dr \tag{10}$$

$$\overline{Nu}\Big\|_0^{R+dR} = 2\big/\left(R+dR\right)^2\cdot\left(\int_0^R Nu_r\cdot r\cdot dr+\int_R^{R+dR} Nu_r\cdot r\cdot dr\right) \tag{11}$$

If dR is taken small enough, then the local Nusselt number can be considered constant over the annulus of radius R and thickness dR:

$$\overline{Nu}\Big\|_0^{R+dR} = \frac{R^2}{\left(R+dR\right)^2}\cdot\overline{Nu}\Big\|_0^{R} + \frac{2}{\left(R+dR\right)^2}\cdot Nu_{r=R}\cdot\left[R^2/2\right]_R^{R+dR} \tag{12}$$

Equivalently, from a simple area average on a disk of radius (r+dr), we get the same expression illustrated in Equation (13).

$$\overline{Nu}\Big\|_0^{r+dr} = \frac{\pi\cdot r^2\cdot\overline{Nu}\Big\|_0^{r} + \pi\cdot\left(\left(r+dr\right)^2 - r^2\right)\cdot Nu_r}{\pi\cdot\left(r+dr\right)^2} \tag{13}$$

Therefore the local Nusselt number is obtained from the average Nusselt number as shown in Equation (14), slightly simplified in Equation (15) when neglecting certain second order terms as dr is already taken small.

$$Nu_r = \left(r+dr\right)^2 \Big/ \left(2\cdot rdr + dr^2\right)\cdot\overline{Nu}\Big\|_0^{r+dr} - r^2\Big/\left(2\cdot rdr + dr^2\right)\cdot\overline{Nu}\Big\|_0^{r} \tag{14}$$

$$Nu_r = \left(r+dr\right)^2 \Big/ \left(2\cdot rdr\right)\cdot\overline{Nu}\Big\|_0^{r+dr} - r\Big/\left(2\cdot dr\right)\cdot\overline{Nu}\Big\|_0^{r} \tag{15}$$

When r gets close to zero, i.e. near to the stagnation point of the jet, the average Nusselt number tends towards the local Nusselt number, as illustrated in Equation (16) and therefore the local Nusselt number at the jet stagnation point is taken as the average Nusselt number for r equal zero.

$$\lim_{r\to 0}\overline{Nu}\Big\|_0^{r+dr} = \lim_{r\to 0}\frac{r^2\cdot\overline{Nu}\Big\|_0^{r} + \left(\left(r+dr\right)^2 - r^2\right)\cdot Nu_r}{\left(r+dr\right)^2} = Nu_r \tag{16}$$

Finally, the corresponding local heat transfer coefficient distribution is recovered, as shown in Equation (17).

$$h_{c\,\mathrm{int}}\left(r\right) = Nu_r\cdot k/d \tag{17}$$

The correlation is applied on each node for each of the neighbouring Piccolo hole and the heat transfer coefficient distribution is taken as the global maximum.

Note that the Reynolds number used in the correlation is based on the jet mass flow rate. Since the total Piccolo mass flow rate is fixed, the jet mass flow rate is indirectly a function of the distance between holes until the jet gets chocked.

The above correlation was actually adapted to the current problem and fitted to 3D CFD simulations of the internal flow for different geometric configurations using FENSAP. Thus, the curvature of the impinged surface and to some extent the interaction between jets are much better accounted for (cf. Appendix B). The CFD-computed heat transfer coefficients are obtained from the Gresho convective heat flux (mentioned in [35]) at the wall and the temperature difference between the reference Piccolo temperature and the local wall temperature, as presented in Equation (18).

$$h_{c\,int} = \frac{q_{c\,\mathrm{int}}}{\left(T_{Pic} - T_w\right)} \tag{18}$$

The 3D fitted correlations are presented in Equation (19) and Equation (20).

$$\overline{Nu}\Big\|_0^r = \mathrm{Re}^{0.76} \cdot \mathrm{Pr}^{0.42} \cdot \left(33 - 2.8 \cdot z_n/d\right) \Big/ \left(533 + 44 \cdot \left(r/d\right)^{1.285}\right) \tag{19}$$

$$Nu_r = \left[r/\left(2 \cdot dr\right) \cdot \left(\left(1 + dr/r\right)^2 \cdot \overline{Nu}\Big\|_0^{r+dr} - \overline{Nu}\Big\|_0^r \right) \right] \cdot \left[z_n/15 + \left(2.6 - z_n/15\right) \cdot e^{-0.25 \cdot r} \right] \tag{20}$$

The gain in terms of computational time is considerable. Indeed, the correlation takes less than 1 second to compute as opposed to the internal 3D CFD computation on a 64-CPU cluster which requires 30 hours to run.

3.3.4 Water Runback

The wing is virtually divided into an upper part and a lower part, from the stagnation line at the leading edge to the upper and lower ends of the protected area. Each part is discretized, according to the external flow surface mesh, therefore recovering the relevant external flow parameters (pressure, convective heat flux, wall shear stress, water collection efficiency) at the nodes.

The water runback and surface temperature distributions were computed using a quasi-2D control-volume-based finite difference model solving for the mass and energy balance on the water film, along 2D cuts linked by transversal conduction, integrating the 3D internal flow and 3D external flow data. This model, illustrated in Figure 3-11 (adapted from [40]), is based on the water film thermodynamic analysis which was first introduced by Messinger [21], and further improved for aircraft icing [22, 25, 29, 34].

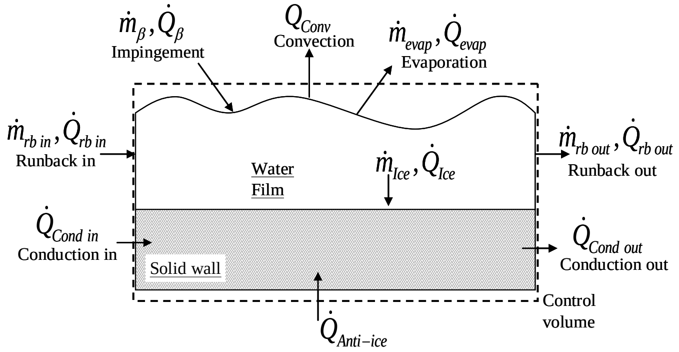

Figure 3-11: Mass and energy balance over a control volume.

Inputs

The water film model uses as inputs relevant flow variables which are extracted from the external flow, droplet impingement and internal flow computations. The water droplet collection efficiency is used to compute the local water mass flow rate impinging on the wing surface. The wall shear stress is used to deduce the water film thickness from the computed water runback. The external local pressure is used to compute the amount of evaporating water. The external local heat flux and imposed boundary temperature, along with the corresponding local adiabatic temperature are used to compute the external local heat transfer coefficient distribution. The adiabatic temperature distribution itself is obtained from an external flow computation at the same conditions except for adiabatic boundary conditions at the wall.

Note that the external convection is referred to the local adiabatic wall temperature in order to take into account the kinetic or aerodynamic heating through viscous friction and avoid referring to a mean recovery reference temperature $T_{ref} = f_{rec} \cdot T_{tot}$ defined by means of a recovery factor $f_{rec} = \left(T_{tot} - T_{\infty}\right) / \left(0.2 \cdot T_{\infty} \cdot M_{\infty}^{2}\right)$ and usually of the order of 0.88. The adiabatic wall temperature distribution is computed for the same flow conditions, replacing the temperature boundary condition by an adiabatic boundary condition at the wall. The external heat transfer coefficient distribution is obtained from the Gresho convective heat flux distribution at the wall as follows.

$$h_{c\,ext} = \frac{q_{c\,ext}}{\left(T_w - T_{adiab}\right)} \tag{21}$$

Also, introducing the adiabatic wall temperature as a reference is a more physical way to look at convective heat transfer and the physical meaning of heat transfer coefficient, which can be considered as the capacity of the fluid flow to locally extract heat from a temperature difference. Indeed, having locally a zero temperature difference does not necessarily mean that the fluid flow has no potential energy extraction capability, even though the local heat transfer is zero.

The local internal heat transfer coefficient distribution (cf. Equation (17)) is obtained from the impinging jet correlation and derived from the Nusselt number expressions presented in Equation (19) and Equation (20).

Assumptions

Before introducing the equations involved in the water film model, the physical assumptions considered in this work are presented.

- The phenomena of interest are considered stationary and fully developed.
- The water runback within and beyond the impingement zone is considered as a uniform water film flowing from the stagnation point on. The formation of the film from the coalescence of impinging water droplets is not addressed.
- The water film is considered smooth and the perturbation, splashing and bouncing of impinging droplets are neglected, as well as the breaking of the film into rivulets.
- The water film is solved over the minimum spanwise periodic pattern, discretized with about 150 spanwise cuts.
- The control volume is located parallel to the wing's skin in the flow direction and includes the metal skin and the water film. At the surface, the cell has a length of Δs and a width of dZw.
- The water film inertia terms are considered negligible compared to the viscous terms and the velocity profile within the film is considered linear.
- The droplet kinetic energy is computed using an impact velocity taken as the free-stream velocity.
- The water film is considered thermally fully developed and the film thickness is so thin (of the order of tens of microns) that there is no temperature gradient within the water film normal to the wall. The local temperatures of the water film and the metal skin are considered equal.
- There is no temperature gradient across the metal skin normal to the wall which means that the conduction from inner to outer skin is neglected ($T_w = T_{w\,ext} = T_{w\,int}$)
- The presence of the water film does not affect the air flow. The mean water film velocity being very small compared to the free stream velocity, the wall shear stress at the air/film interface is assumed equal to the wall shear stress computed by the air flow CFD simulation directly at the wall.
- All physical and thermodynamic variables are considered constant within a given control volume.

Mass and energy balance

The water film model consists in a local mass and energy balance, solving for local steady-state wall temperature and water runback mass flow rate over the airfoil surface. It was implemented using a control-volume-based finite difference scheme.
The mass balance is expressed as follows in Equation (22).

$$\dot{m}_{IN} = \dot{m}_{rb\,in} + \dot{m}_{\beta} = \dot{m}_{rb\,out} + \dot{m}_{evap}\left(+\dot{m}_{ice}\right) = \dot{m}_{OUT} \tag{22}$$

Water impingement mass flow rate	$\dot{m}_\beta = LWC_\infty \cdot V_\infty \cdot \beta \cdot S_w$
Water runback mass flow rate	$\dot{m}_{rb\,out} = \rho_w \cdot dZ_w \cdot h_f \cdot \bar{U}_f$
Water evaporative mass flow rate	$\dot{m}_{evap} = \frac{0.7 \cdot h_{c\,ext} \cdot S_w}{c_p} \cdot \left[\frac{P_{vap\,w} - H_r \cdot P_{vap\,\infty}}{P_{s\,w}}\right]$

Table 1: Mass balance terms

$P_{vap\,w}$ is the saturation vapor pressure at the wall, H_r is the relative humidity, $P_{vap\,\infty}$ is the saturation vapor pressure in ambient air and $P_{s\,w}$ is the static pressure above the control volume.

Note that the water running back into the control volume is equal to the water running back out of the previous cell.

The energy balance is expressed as follows:

$$\left[\dot{Q}_{rb}\right]_{in}^{out} + \dot{Q}_\beta + \dot{Q}_{anti-ice} + \dot{Q}_{cond\,\equiv} + \dot{Q}_{cond\,\perp} - \dot{Q}_{conv} - \dot{Q}_{evap} - \dot{Q}_{rad} \left(+\dot{Q}_{ice}\right) = 0 \qquad (23)$$

Water runback enthalpy	$\dot{Q}_{rb} = \dot{m}_{rb} \cdot c_{p\,w} \cdot T_{rb}$
Impinging droplets total enthalpy	$\dot{Q}_\beta = \dot{m}_\beta \cdot \left(\left\|U_d\right\|^2 / 2 + c_{p\,w} \cdot T_{d,\infty}\right)$
Ice and phase change enthalpy	$\dot{Q}_{ice} = \dot{m}_{ice} \cdot \left[L_{fus} - c_{p\,ice} \cdot \tilde{T}_w\right]$
Evaporative power	$\dot{Q}_{evap} = \dot{m}_{evap} \cdot L_{vap}$
Internal convective power	$\dot{Q}_{anti-ice} = h_{c\,int} \cdot S_w \cdot \left(T_{Pic} - T_w\right)$
External convective power	$\dot{Q}_{conv} = h_{c\,ext} \cdot S_w \cdot \left(T_w - T_{adiab}\right)$
Tangential conductive power	$\dot{Q}_{cond\,\equiv} = \lambda \cdot e \cdot dZ_w \cdot \left[\left(T_{i-1} - T_i\right)/\Delta s_{i-1} + \left(T_{i+1} - T_i\right)/\Delta s_{i+1}\right]$
Transversal conductive power	$\dot{Q}_{cond\,\perp} = \lambda \cdot e \cdot \left\|s_{i+1} - s_{i-1}\right\| \cdot \left(T_{j+1} - 2 \cdot T_j + T_{j-1}\right) / \left(2 \cdot dZ_w\right)$
Irradiative power	$\dot{Q}_{rad} = \sigma \cdot \varepsilon \cdot S_w \cdot \left(T_w^4 - T_\infty^4\right)$

Table 2: Energy balance terms

The streamwise conductive heat transfer terms along the 2D cuts are expressed as tangential conduction whereas the spanwise conductive heat transfer terms in-between 2D cuts are expressed as transversal conduction.

The system of equations for the energy balance is put in matrix form and solved iteratively from an initial temperature distribution. The temperature dependent mass balance is updated at each iteration until convergence.

$$A \cdot [\Delta T] = [R] = [\mathrm{b}] - A \cdot [T] \qquad (24)$$

A is the influence matrix, [b] the forcing vector, [R] the residual vector and the temperature vector [T] is obtained as follows: $\left[T\right]^{n+1} = \left[T\right]^{n} - \alpha \cdot \left[\Delta T\right]^{n+1}$.

Note that in the context of this study of anti-icing system, the main focus is what is occurring within the heated zone in terms of water runback or ice accretion. On this protected area, the temperature would very rarely reach the freezing point or below, which is why the ice accretion terms are expressed between brackets in the above equations. However, in the occurrence of subzero temperature, a flag is triggered and the system is then expressed slightly differently with a new variable defined as the freezing fraction (i.e. fraction of incoming liquid water that freezes), as shown in Equation (25) and Equation (26). The unknowns become the surface temperature and the freezing fraction.

$$f = \dot{m}_{ice} \big/ \dot{m}_{IN} = \dot{m}_{ice} \Big/ \left(\dot{m}_{rb\,in} + \dot{m}_{\beta} \right) \tag{25}$$

$$\dot{m}_{rb\,out} + \dot{m}_{evap} = \left(1 - f\right) \cdot \dot{m}_{IN} = \left(1 - f\right) \cdot \left(\dot{m}_{rb\,in} + \dot{m}_{\beta} \right) \tag{26}$$

Substituting the terms in both the mass continuity and the energy equations, and first assuming T_w=273.15 K, the freezing fraction is evaluated. A negative freezing fraction would imply that the surface temperature should be in fact greater than 273.15 K, so f would be set to zero and T_w recomputed. Having $0 \leq f \leq 1$ implies that the initial guess for T_w was correct. A freezing fraction greater than unity would imply that the surface temperature should be in fact lower than 273.15 K so f would be set to one and T_w recomputed. The freezing fraction and surface temperature are thus computed iteratively until convergence [25, 34].

Once the wall temperature, water runback, water evaporation and eventual ice accretion are computed, the water film height is deduced from the water runback mass flow rate, assuming a linear velocity profile in the film, as shown in Equation (27) and Equation (28).

$$\dot{m}_{rb\,out} = \rho_w \cdot dZ_w \cdot h_f \cdot \bar{U}_f = \rho_w \cdot dZ_w \cdot h_f \cdot \left(\frac{1}{2} \cdot \frac{\tau_w}{\mu_w} \cdot h_f\right) \tag{27}$$

$$h_f = \sqrt{\frac{\mu_w}{\rho_w} \cdot \frac{2 \cdot \dot{m}_{rb\,out}}{\tau_w \cdot dZ_w}} \tag{28}$$

Within the impingement zone, the impinging droplets coalesce to form a water film which will remain until the impingement limit or as long as its height is important enough. Otherwise, below a minimum height defined as a function of the maximum bead height and contact angle, the film breaks into rivulets [17-20, 47] as illustrated in Figure 3-12 (adapted from [19]).

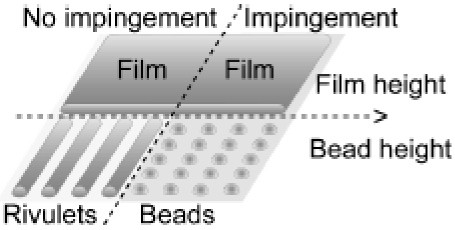

Figure 3-12: Water film breaking into rivulets.

Practically speaking, this phenomenon induces a decrease of the thermal exchange surface and thus a local loss of anti-icing performance since some increasing part of the exchange surface is directly exposed to external convection instead of providing energy to the water. This aspect was not implemented in the current model since the main focus was not the accuracy of the icing model.

A finite-element-based water film model inspired by the PDE (Partial Differential Equation) expression of water runback was also implemented in order to solve directly for the water film thickness [43-44, 116].

Indeed, from the continuity and energy equations of the water film expressed in PDE form, we get:

$$\rho_w \cdot \left[\frac{\partial h_f}{\partial t} + \vec{\nabla}\left(\bar{U}_f \cdot h_f\right) \right] = \dot{m}''_\beta - \dot{m}''_{evap} - \dot{m}''_{ice} \tag{29}$$

$$\begin{aligned} \rho_w \cdot \left[\frac{\partial h_f \cdot c_{p\,w} \cdot \tilde{T}_w}{\partial t} + \vec{\nabla}\left(\bar{U}_f \cdot h_f \cdot c_{p\,w} \cdot \tilde{T}_w\right) \right] &= \dot{m}''_\beta \cdot \left(\left\| U_d \right\|^2 / 2 + c_{p\,w} \cdot \tilde{T}_{d,\infty} \right) \\ -\dot{m}''_{evap} \cdot L_{evap} - h_{conv} \cdot \left(\tilde{T}_w - \tilde{T}_{adiab} \right) + \dot{Q}''_{cond} - \dot{Q}''_{rad} + \dot{Q}''_{anti-ice} &+ \dot{m}''_{ice} \cdot \left[L_{fus} - c_{p\,ice} \cdot \tilde{T}_w \right] \end{aligned} \tag{30}$$

Again, considering steady state conditions and a linear velocity profile inside the water film, neglecting the radiation and assuming no ice accretion inside the heated zone, the equations become:

$$\rho_w \cdot \vec{\nabla}\left(\frac{\tau_w}{2 \cdot \mu_w} \cdot h^2{}_f \right) = \dot{m}''_\beta - \dot{m}''_{evap} \tag{31}$$

$$\rho_w \cdot \vec{\nabla}\left(\frac{\tau_w \cdot c_{p\,w}}{2 \cdot \mu_w} \cdot h_f{}^2 \cdot \tilde{T}_w \right) = \dot{Q}''_\beta - \dot{Q}''_{evap} - \dot{Q}''_{conv} + \dot{Q}''_{cond} + \dot{Q}''_{anti-ice} \tag{32}$$

Integrating over the domain, using the weak Galerkin formulation with linear shape functions, we get in matrix form the following coupled systems of equations:

$$\begin{cases} K\cdot\left[\Delta h_f\right]=\left[R^{\circ}\right]=\left[b^{\circ}\right]-K\cdot\left[h_f\right] \\ \Gamma\cdot\left[\Delta T_w\right]=\left[R^{*}\right]=\left[b^{*}\right]-\Gamma\cdot\left[T_w\right] \end{cases} \tag{33}$$

Here K and Γ refer to the influence matrices of the continuity and energy equations respectively; $[R^{\circ}]$ and $[R^{*}]$ are the residual vectors and $[b^{\circ}]$ and $[b^{*}]$ the forcing vectors. The matrix systems are solved iteratively from initial guess solutions.

Implementing the finite element method to solve directly for temperature and water film height brought interesting insights and better understanding concerning the numerical behaviour of the discretized equations and the implementation and treatment of the boundary conditions, but this model was not further used in this work due to stability issues in a few cases which made it difficult to manage in the frame of an GA-based optimization loop.

Water Film Solution

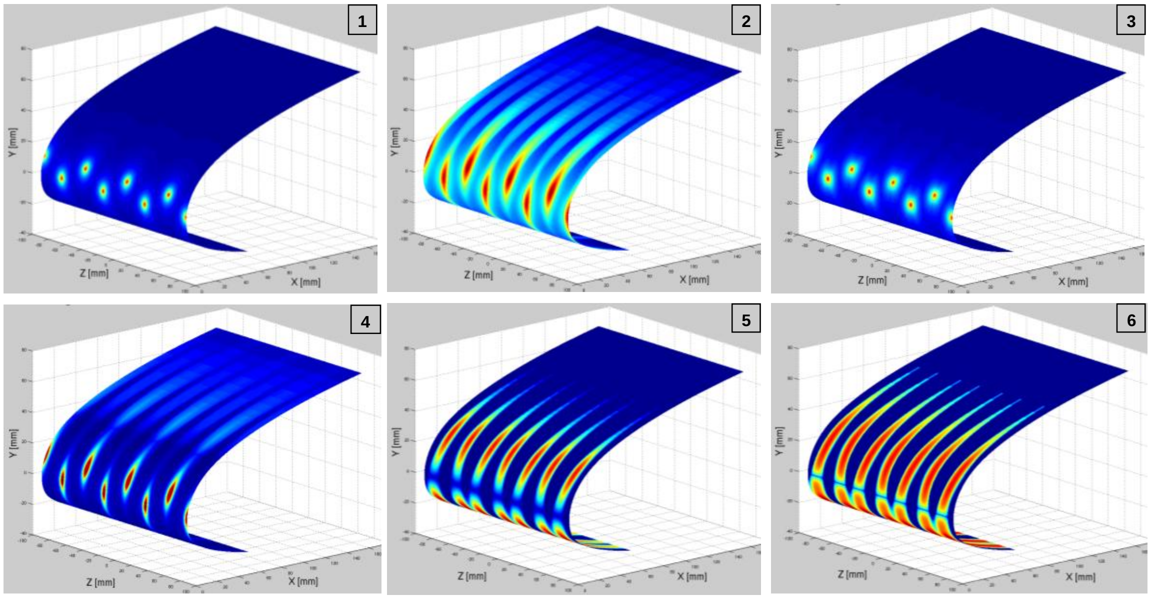

1. Internal heat transfer coefficients
2. Wall temperature
3. Anti-icing heat flux
4. Water evaporation
5. Water runback
6. Water film thickness

Figure 3-13: Example of water film solution.

Figure 3-13 illustrates an example of water film solution in the case of non-fully-evaporative conditions. Actually, in this case, a fully-evaporative state is still reached on the upper surface. The results are presented over a section of three periodic patterns for better visibility. From external flow inputs and correlated anti-icing heat transfer coefficient distribution (cf. Picture (1)), the surface temperature is obtained (cf. Picture (2)) which leads to the anti-icing heat flux distribution provided to the skin (cf. Picture (3)). Picture (4) shows the distribution of evaporated water. Picture

(5) presents the water runback on the airfoil skin, whose corresponding film thickness is shown in Picture (6). In this case, we are only interested in what is occurring on the heated zone. If any water runback is exiting the zone of interest, it might eventually freeze further downstream which leads to the definition of the optimization criterion introduced in the previous section.

This water film model was validated with respect to icing tunnel test results provided by Bombardier Aerospace [78].

3.3.5 Validation Results

Two sets of icing tunnel experimental data obtained over the currently used generic swept wing were available and provided by Bombardier Aerospace [78]. These data consists in temperature sensor data taken over a cut on the wing surface located in-between two consecutive Piccolo holes, and compiled for two different test conditions. The first set is obtained in "dry air" condition (with zero Liquid Water Content) and the second one in "wet air" condition. Table 3 summarizes the test conditions with the external flow parameters presented in blue and the Piccolo tube flow parameters in red.

Flow Parameters	**Dry Air Test Case**	**Wet Air Test Case**
Angle of Attack	**4.7°**	**4.5°**
Free-Stream Velocity	**76.7 m/s**	**76.4 m/s**
Free-Stream Mach Number	**0.234**	**0.233**
Free-Stream Total Pressure	**103421 Pa**	**103421 Pa**
Free-Stream Temperature	**266.6 K**	**266.7 K**
Liquid Water Content	**0 g/m^3**	**0.62 g/m^3**
Median Volume Diameter	**N/A**	**40 μm**
Bleed-Air Temperature	**445.6 K**	**482 K**
Bleed-Air Total Pressure	**257702 Pa**	**186796 Pa**
Total Bleed-Air Mass Flow Rate	**75.54 g/s**	**40.96 g/s**
Bleed-Air Mass Flow Rate per Hole	**1.3 g/s**	**0.7 g/s**

Table 3: Icing experimental test case parameters.

These icing experimental test cases were treated as test cases for the models presented in the previous sections, in the sense that the corresponding numerical solutions were computed according to the methodology. Strictly speaking, the internal heat transfer coefficient distributions were directly extracted from the internal flow 3D CFD computations, and the version of the water film solver included the transversal (spanwise) conduction.

Comparison between experimental and numerical results is presented in Figure 3-14.

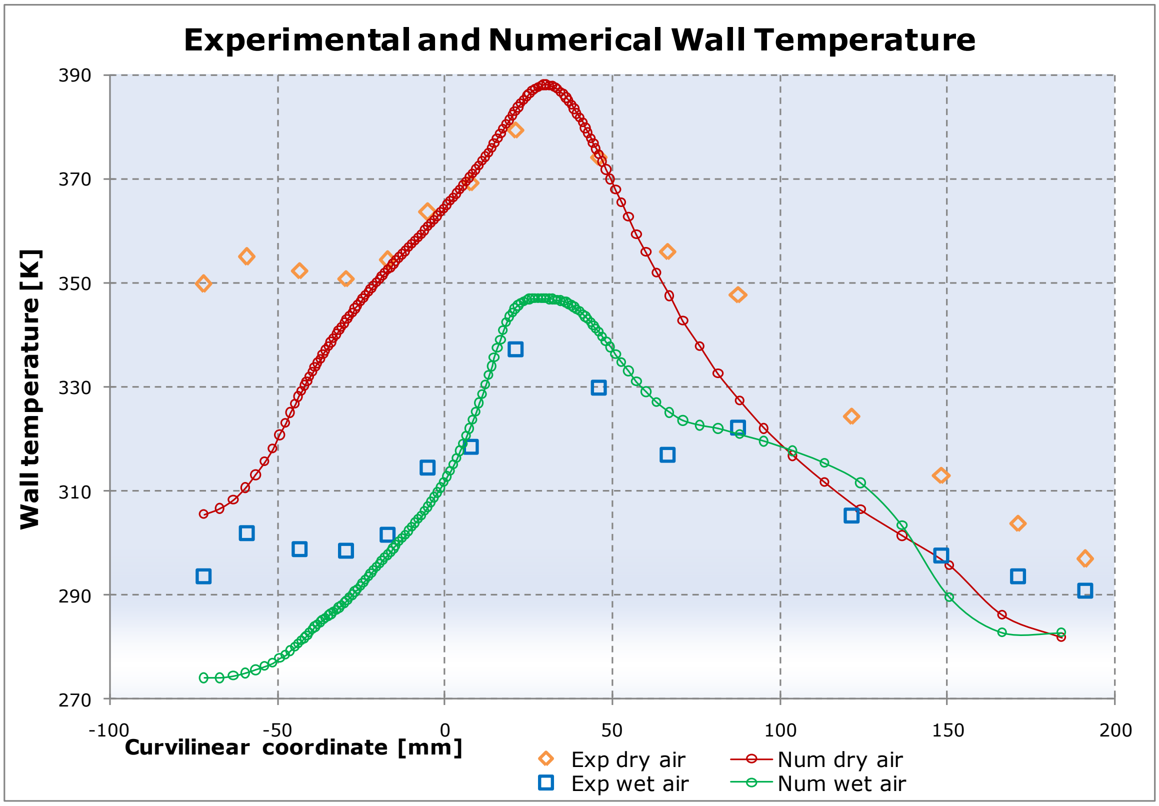

Figure 3-14: Experimental and numerical icing test results.

The numerical results revealed quite acceptable match with the experimental results, particularly in the region located in the vicinity of the jets impact zones ($-40\ \mathrm{mm} \le s \le 80\ \mathrm{mm}$) where the relative error would be less than ±3%. The average temperature difference was 4.4°C for the "dry air" case and 5.6°C for the "wet air" case. The error increased towards the upper end of the slat to about 8% and 5% for the "dry air" and the "wet air" conditions, respectively. The highest discrepancies occurred towards the lower end of the slat where the relative error would reach 13% and 8%, respectively. These discrepancies are attributed on the one hand to the difficulty to accurately compute the internal flow through the slot and rear bay because of geometric simplifications, and on the other hand to the presence of the exhaust flow and conduction through the stiffener, as illustrated in Figure 3-15 (adapted from Planquart *et al* [59]), which were not introduced in the numerical model.

The remaining discrepancies can be attributed to the simplifying assumptions of the water film model which does not account for certain features, like the non-negligible effect of rivulet flow described in the previous section or the slight spanwise component of the water runback, especially in the vicinity of the stagnation point, due to the three-dimensionality of the flow over the swept wing.

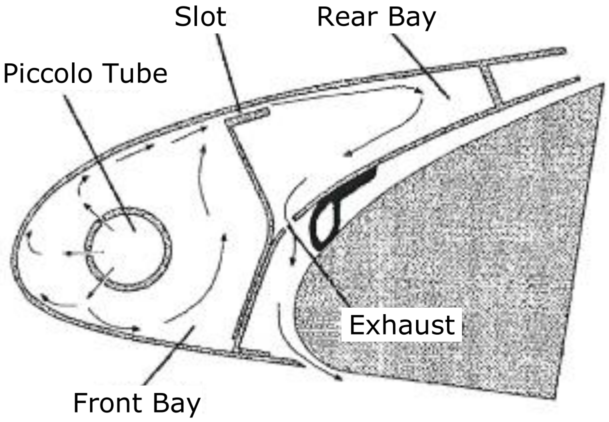

Figure 3-15: Sketch of a slat hot-air anti-icing system section.

Now that the methodology is introduced and the different models are defined and validated, the optimization process is applied to the generic design case provided by Bombardier Aerospace and the results are presented in the next section.

4. APPLYING THE OPTIMIZATION METHODOLOGY

4.1 Genetic Algorithm's Convergence

Figure 4-1 illustrates the typical convergence behavior of the genetic algorithms.

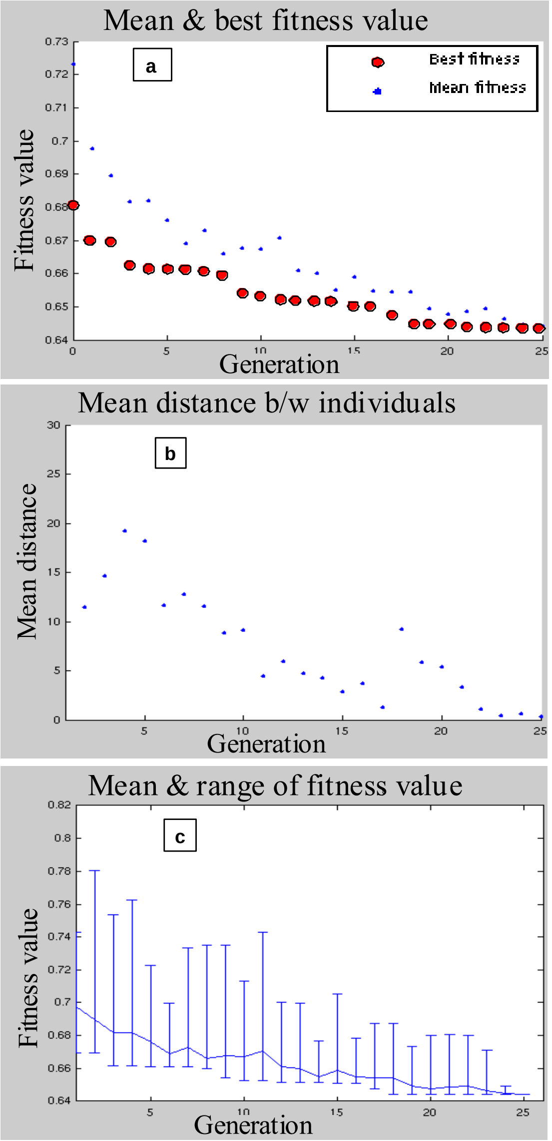

Figure 4-1: Genetic algorithm's convergence.

The red dots in Picture (a) show the evolution of the best individual from generation to generation, which gradually converges towards the global optimum. The blue dots represent the average of the population, which also gradually evolves towards the best individual. In Picture (b) the mean distance between individuals tends to decrease as the generation number grows. In fact, the population is initially uniformly distributed across the design space using the Lp-τ method and will gradually contract and converge towards the global optimum, as summarized in Picture (c) which shows the evolution of the mean value and range of the population with the generations. Note that a gap in the mean distance or the range of fitness value between two consecutive generations, like between generations 17 and 18 in Figure 4-1, can be explained as the result of stochastic mutations (cf. section 3.2.2).

As a lower-dimension analogy, easier to visualize, a simpler 2D optimization example with a relatively simple arbitrarily chosen objective function containing a global optimum and a local one is presented in Figure 4-2.

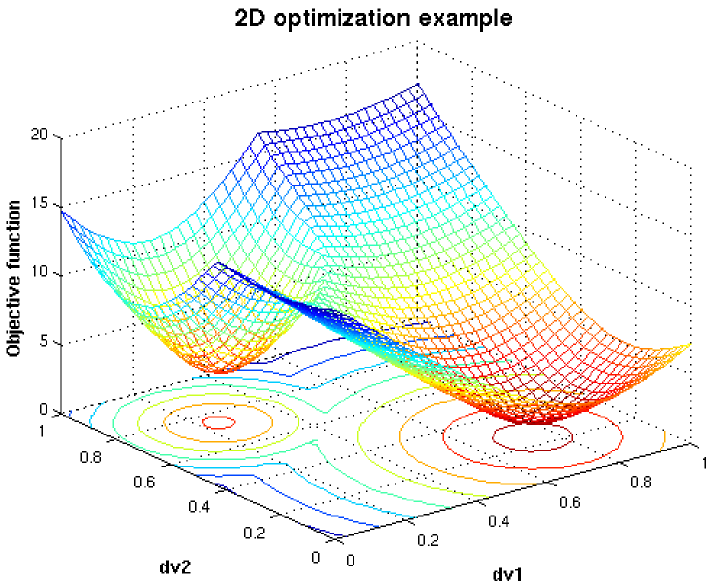

Figure 4-2: 2D optimization example.

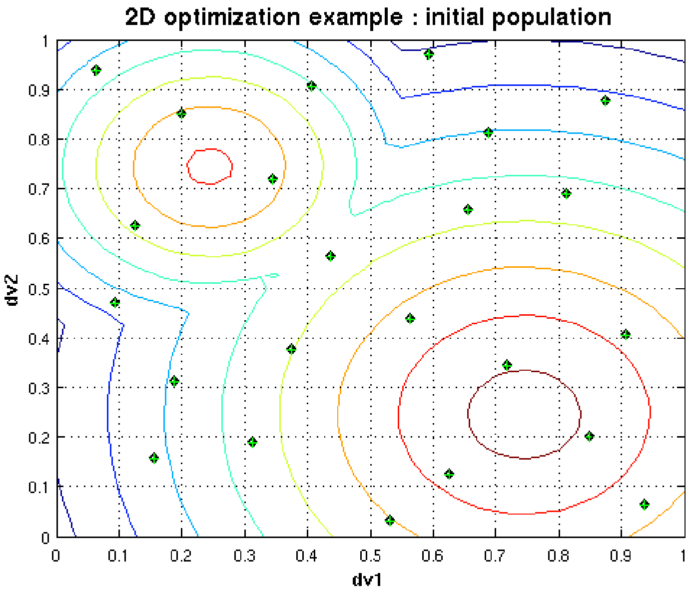

Figure 4-3: Initial population uniformly spread using Lp-τ.

The GA initial population (in this case 23 individuals) is first uniformly distributed over the design space, as shown in Figure 4-3. The GA processes unfold with the generations. Partial convergence is shown at generation #5 and #8 in Figure 4-4 and the finally converged population is obtained for generation #12, as shown in Figure 4-5.

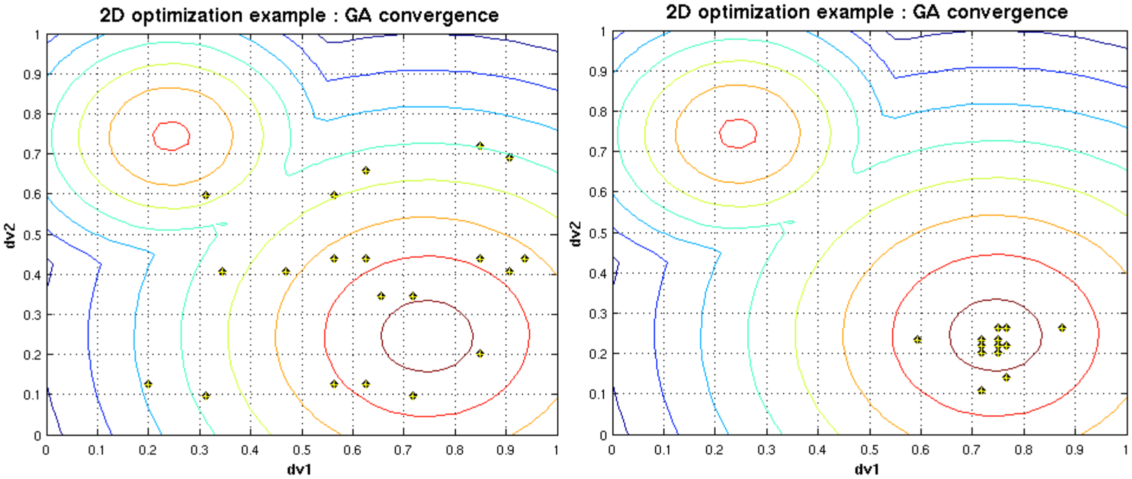

Figure 4-4: Partial GA convergence.

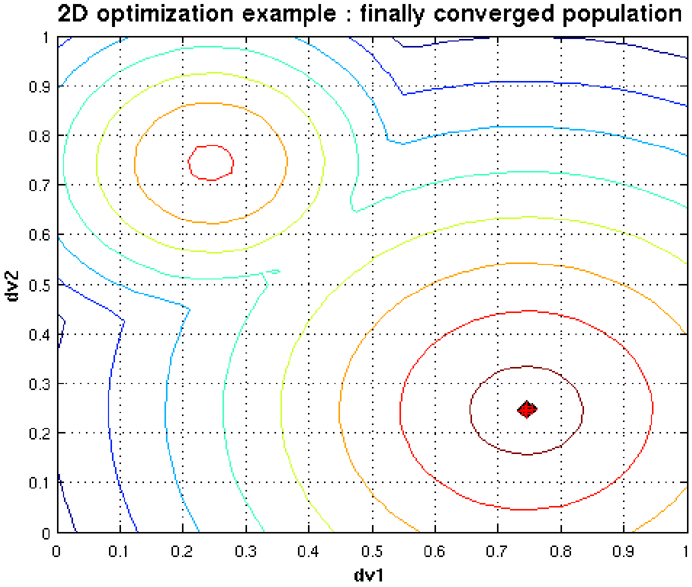

Figure 4-5: Final GA convergence.

In order to illustrate the subtleties of Piccolo tube optimization with fixed available anti-icing power, Figure 4-6 presents three Piccolo tube configurations (cf. Pictures denoted by -a) with their associated water runback solutions (cf. Pictures denoted by -b).

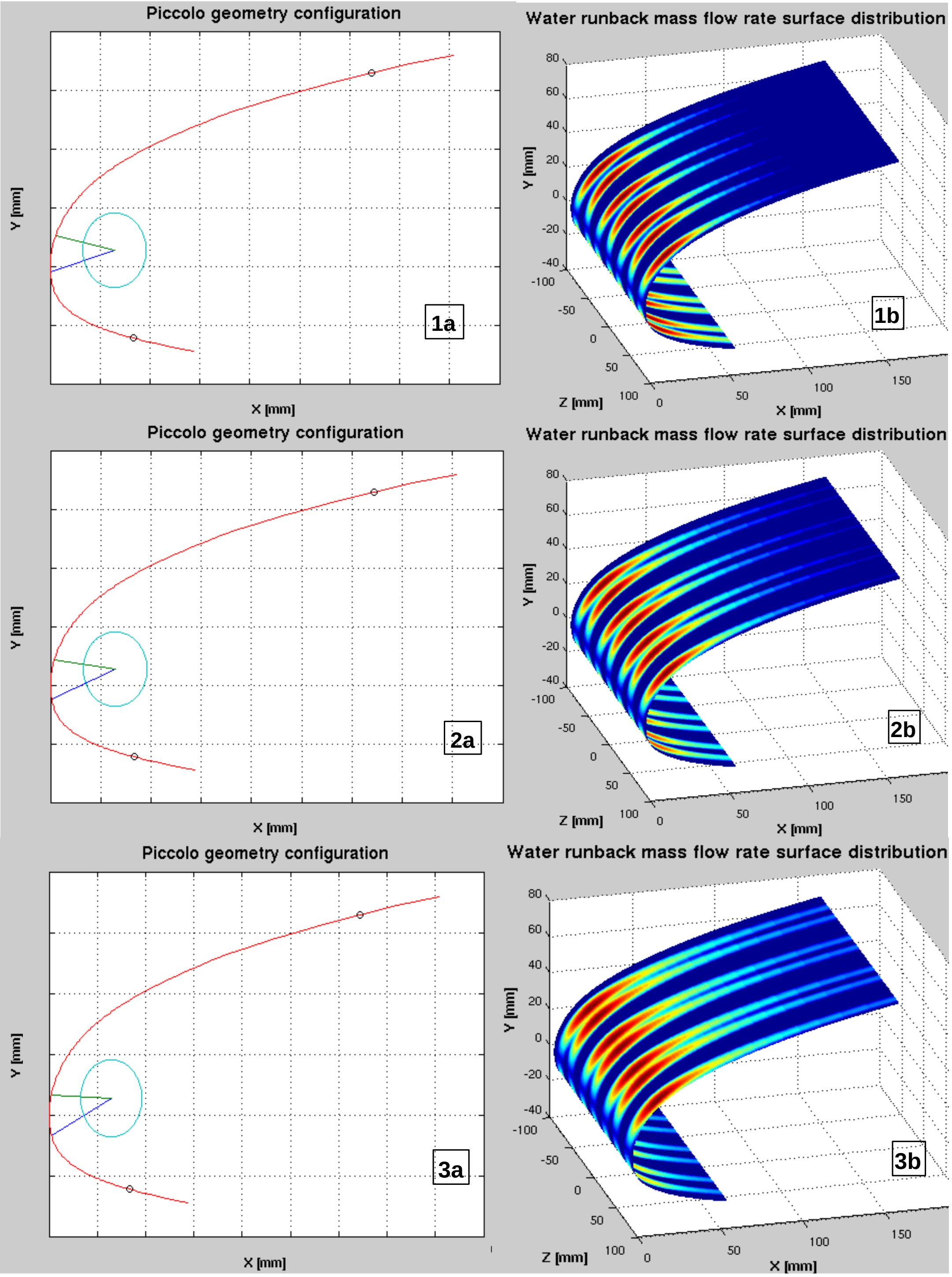

Figure 4-6: Optimal design configuration versus slightly off-design configurations.

In this study, the given anti-icing enthalpy seemed to be inadequate to achieve fully evaporative in any configuration within the range of the design variables. Therefore, the lower surface minimum water runback criterion, mentioned in section 3.3.3, was used.

The second configuration in Picture (2a) refers to the optimal geometric configuration in the case of 3 design variables (jet angles and distance between holes). It shows fully evaporative conditions by the end of the upper heated surface with minimal runback out of the lower heated surface, as shown in Picture (2b). Configurations (1) and (3) correspond to slight variations about the optimal point. On the one hand, the first configuration (cf. Picture (1a)) leads to stronger evaporative conditions on the upper heated surface, but to more runback on the lower heated surface (cf. Picture (1b)). On the other hand, the third configuration (cf. Picture (3a)) leads to water runback on both upper and lower surfaces (cf. Picture (3b)). It is important pointing out that, for all three configurations, the available anti-icing power (i.e. the Piccolo tube air temperature and mass flow rate) is identical.

The optimization results for 3, 4 and 5 design variables presented in the following sections for different arrangements are compared to the initial generic geometric configuration and water film results (cf. configuration #0 in Figure 4-7).

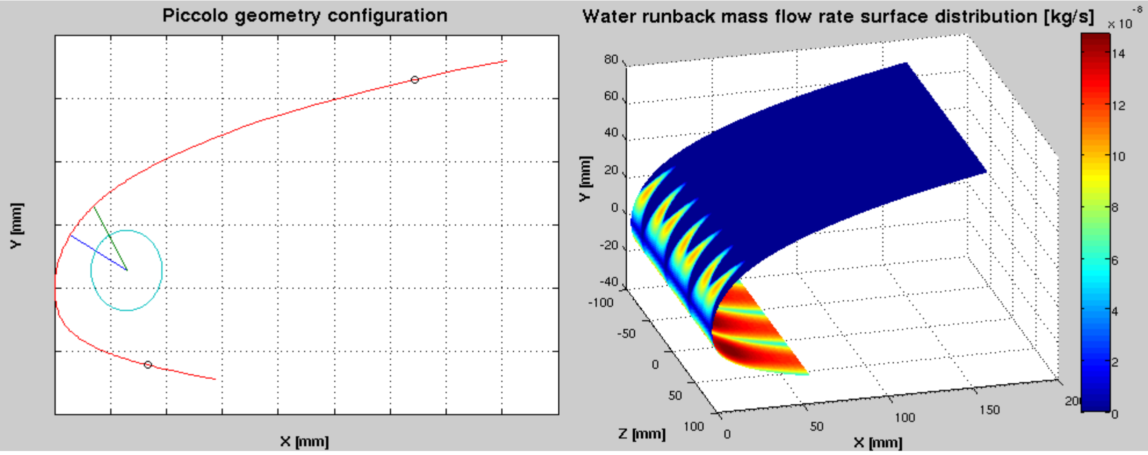

Figure 4-7: Initial generic configuration and corresponding water runback.

These results are the optimal geometric configurations obtained in the context of this particular single objective optimization and within the range of the design variables.

Also, the following results represent a mean of 3 to 5 GA results in order to better represent the coherence of the results and level down the slight variations in the results introduced by the non-deterministic nature of genetic algorithms.

4.2 3-Design-Variable Configurations

The first arrangement for 3 design variables consists of the two jet angles and the distance between holes (cf. configuration #1 in Figure 4-8). The second arrangement for 3 design variables consists of one jet angle (keeping a 30° opening between the two rows) and the x- and y- positions of the Piccolo tube (cf. configuration #2 in

Figure 4-9). Figure 4-8 and Figure 4-9 present the results for configurations #1 and #2, respectively, showing the optimal Piccolo geometry configuration on the left picture and the corresponding water runback results on the right picture. These results for three design variables were obtained using a GA population size of 20 for 50 generations. The POD module was supported by a database of 120 snapshots.

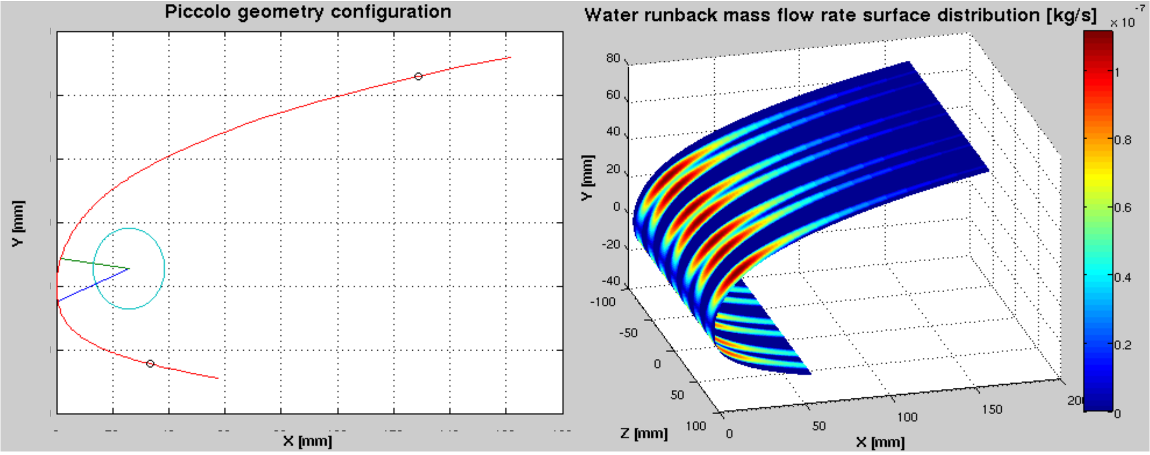

Figure 4-8: First 3-design-variable optimal configuration and corresponding water runback.

For all these arrangements, the parameters which are not used as design variables are kept identical to the initial generic configuration (cf. Table 4).

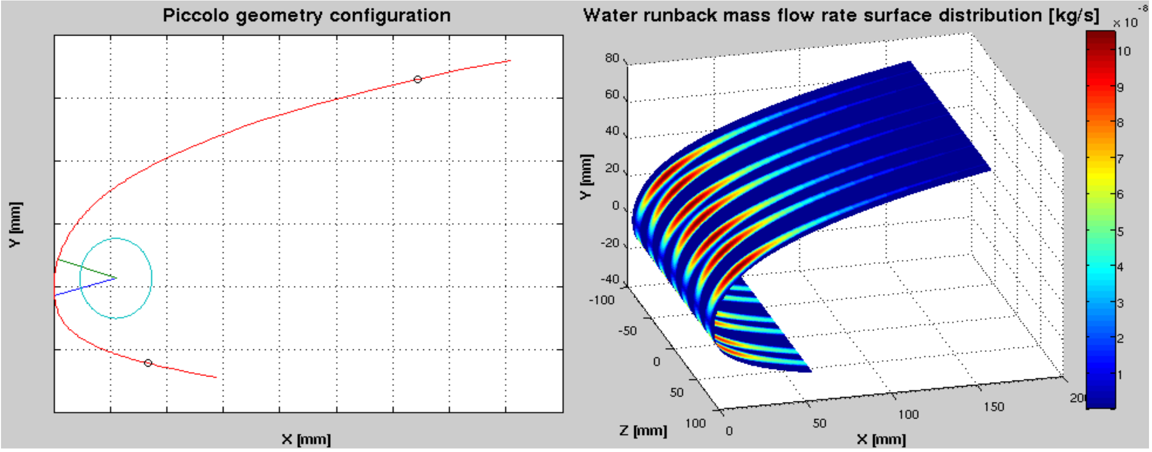

Figure 4-9: Second 3-design-variable optimal configuration and corresponding water runback.

4.3 4-Design-Variable Configurations

The first arrangement for 4 design variables consists of the two jet angles and the x- and y- positions of the Piccolo tube (cf. configuration #3 in Figure 4-10). The second arrangement for 4 design variables consists of one jet angle (keeping a 30° opening between the two rows), the distance between holes and the x- and y- positions of the Piccolo tube (cf. configuration #4 in Figure 4-11). Again, the parameters which are not used as design variables are kept identical to the initial generic configuration (cf. Table 4). These results for three design variables were obtained using a GA population size of 25 for 50 generations. The POD module was supported by a database of 160 snapshots.

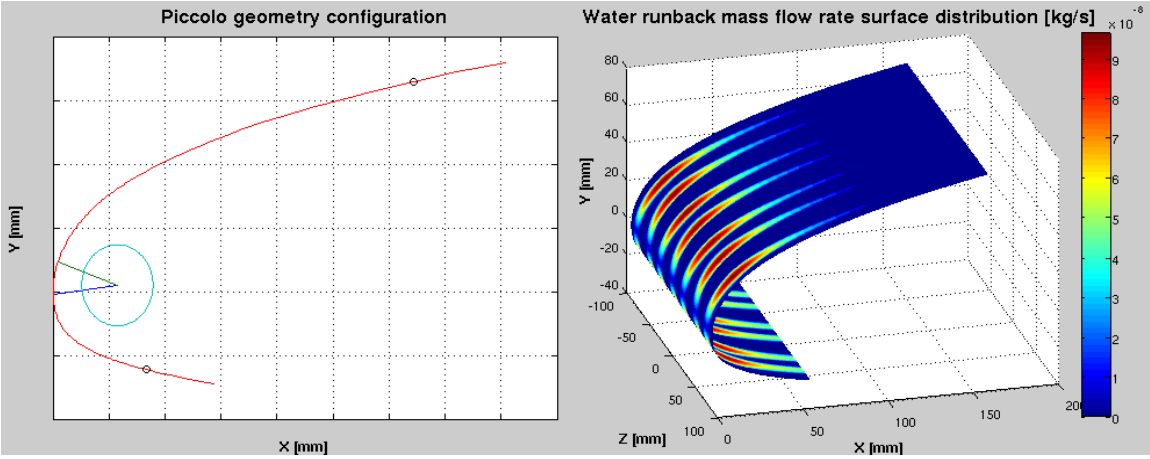

Figure 4-10: First 4-design-variable optimal configuration and corresponding water runback.

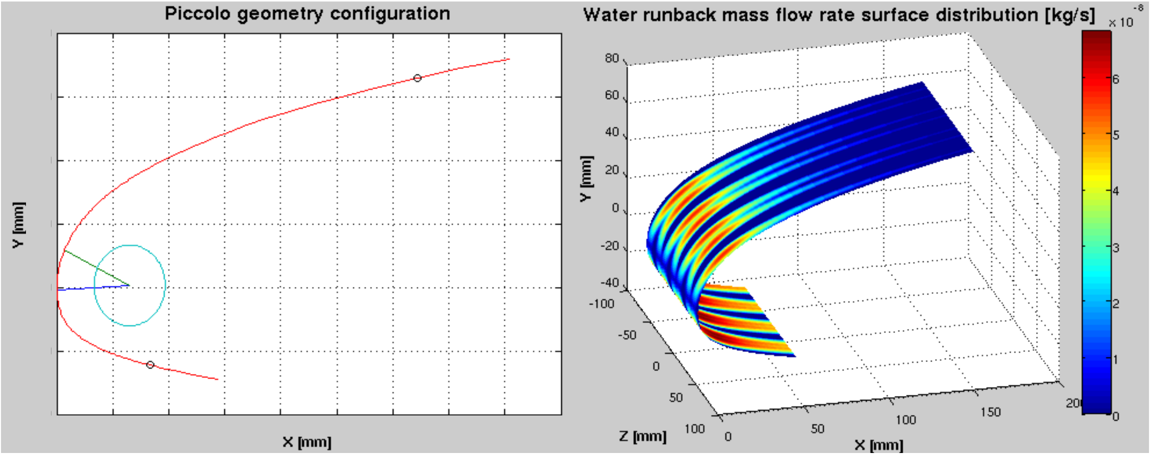

Figure 4-11: Second 4-design-variable optimal configuration and corresponding water runback.

4.4 5-Design-Variable Configuration

Finally, the arrangement for 5 design variables combines all Piccolo tube geometric parameters (cf. configuration #5 in Figure 4-12). Again, the parameters that are not used as design variables are kept identical to the initial generic configuration (cf. Table 4). These results for three design variables were obtained using a GA population size of 30 for 50 generations. The POD module was supported by a database of 200 snapshots.

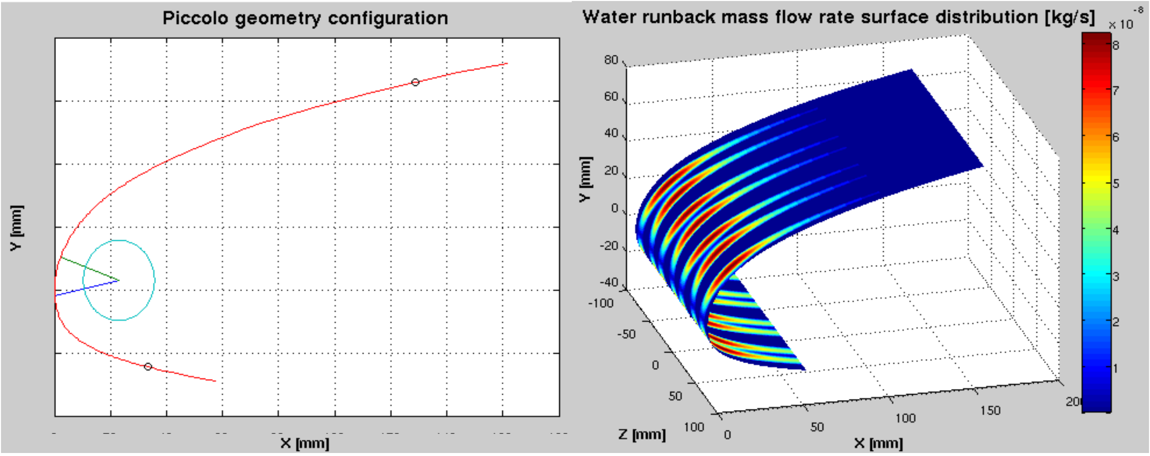

Figure 4-12: 5-design-variable optimal configuration and corresponding water runback.

4.5 Results Summary

The different configurations are summarized in Table 4. The values of the initial generic configuration's parameters are specified in blue. The last column shows the amount of water runback on the lower surface in [mg/s/m of span].

Configuration	Jet Angle #1	Jet Angle #2	Distance b/w Holes	X-location	Y-location	Water Runback
Total Impingement	N/A	N/A	N/A	N/A	N/A	978.4 mg/s/m
Generic	30°	Δθ = 30°	50 mm	25 mm	5 mm	203.3 mg/s/m
3 design variables #1	-19.1°	Δθ = 26.4°	46.8 mm	25 mm	5 mm	36.85 mg/s/m
3 design variables #2	-15.3°	Δθ = 30°	50 mm	22.1 mm	2.5 mm	39.19 mg/s/m
4 design variables #1	-8.6°	Δθ = 37.3°	50 mm	23.2 mm	2.1 mm	26.29 mg/s/m
4 design variables #2	-15.3°	Δθ = 30°	31.8 mm	25.9 mm	0.6 mm	43.75 mg/s/m
5 design variables	-11.4°	Δθ = 45.8°	45.2 mm	22.8 mm	3.2 mm	37.95 mg/s/m

Table 4. Summary of the different optimal configurations compared to initial generic design.

For this particular design case, the computed amount of water runback for the initial generic configuration was 203.3 mg/s/m of span for a total amount of water droplet impingement of 978.4 mg/s/m of span. For 3 design variables, configuration #1 led to a reduction of the water runback by a factor of 550% and configuration #2 by close to 520% (i.e. the water runback was divided by 5.2). For 4 design variables, configuration #1 led to a reduction of the water runback by a factor of about 775%

and configuration #2 by 465%. Finally, for 5 design variables, the obtained optimal configuration led to a reduction of the water runback by a factor of 535%.

Considering a more coherent way to look at the results by comparing only the related configurations gives an interesting perspective regarding the consistency of the results. Logically, releasing an additional degree of freedom, i.e. adding a design variable, will lead to a "better" optimum. Actually, the optimal configuration of the subspace might only be a local optimum of the higher-dimension space. It is the most probable case since the subspace is constrained arbitrarily with respect to the remaining design variables. This improvement of the optimal configuration was in fact experienced when progressing from three to four design variables (cf. Table 5).

Configuration	Jet Angle #1	Jet Angle #2	Distance b/w Holes	X-location	Y-location	Water Runback
Total Impingement	**N/A**	**N/A**	**N/A**	**N/A**	**N/A**	**978.4 mg/s/m**
Generic	**30°**	**Δθ = 30°**	**50 mm**	**25 mm**	**5 mm**	**203.3 mg/s/m**
3 design variables	**-15.3°**	**Δθ = 30°**	**50 mm**	**22.1 mm**	**2.5 mm**	**39.19 mg/s/m**
4 design variables	**-8.6°**	**Δθ = 37.3°**	**50 mm**	**23.2 mm**	**2.1 mm**	**26.29 mg/s/m**
5 design variables	**-11.4°**	**Δθ = 45.8°**	**45.2 mm**	**22.8 mm**	**3.2 mm**	**37.95 mg/s/m**

Table 5. Consecutive optimal configurations compared to initial generic design.

However, this was not satisfied for five design variables, even though the design was greatly improved with respect to the generic configuration (in the context of this single objective optimization) and still better than the 3-design-variable optimal configuration.

Unfortunately, releasing an additional degree of freedom expands the size of the design space whose accurate exploration is thus made more difficult as more POD snapshots would be needed. Also, it is important to keep in mind that the GA procedure is based on POD approximate evaluations which can introduce increasing error with the number of dimensions and mislead GA convergence. This is in relation to the Kriging interpolation method as well, which contains non-deterministic components and gets more delicate to perform with increasing number of dimension and associated increasing non-linearity of the problem. Not only that, but also the set of POD snapshots used for three, four and five design variables was different by definition since discretizing different subspaces. This would affect the optimization process by modifying the way the physical features are incorporated into the POD model. Another related aspect concerns the repeatability of the genetic algorithm which is intrinsically non-deterministic. In any case, there is also a compromise between accuracy and computational cost since increasing the population size will help the exploration of the design space and increase the consistency of the model, while increasing the number of generations will improve the convergence level and the consistency and repeatability of the results, at least as far as the genetic algorithm is concerned, but certainly at the cost of additional computations.

Here, the optimization was not done sequentially, since for each of these configurations the GA was re-initialized to a uniformly distributed initial population. However, sequential optimization was investigated with moderate results. Indeed, starting from the lower-dimension optimal GA population results would not necessarily lead to significant improvement, even if the population is uniformly spread in the supplementary dimension. This bias in the GA initial population could lead to the convergence towards a local optimum and therefore would not guaranty convergence towards the best possible optimum of the constrained design space. It would even result in a more laborious convergence, since it would require a higher rate of mutation to recover the necessary diversity in the population.

As a lower-dimension analogy, a simpler 2D optimization example with a relatively simple arbitrarily chosen objective function containing a global optimum and a local one was implemented (cf. Appendix D) and the trends mentioned above were verified.

In order to clarify this matter, the optimization methodology was run for five design variables without the POD-Kriging module, with the Genetic Algorithm module directly linked to the water film solver. It led to a clear convergence towards a much more consistent result (885% improvement in terms of water runback), as shown in Table 6.

Configuration	**Jet Angle #1**	**Jet Angle #2**	**Distance b/w Holes**	**X-location**	**Y-location**	**Water Runback**
Total Impingement	**N/A**	**N/A**	**N/A**	**N/A**	**N/A**	**978.4 mg/s/m**
Generic	**30°**	**Δθ = 30°**	**50 mm**	**25 mm**	**5 mm**	**203.3 mg/s/m**
5 design variables w/o POD	**-17.8°**	**Δθ = 36.6°**	**74.4 mm**	**23.6 mm**	**1.1 mm**	**23.03 mg/s/m**

Table 6. Optimal configuration obtained without POD.

The optimal Piccolo geometric configuration and associated water runback solution is presented in Figure 4-13.

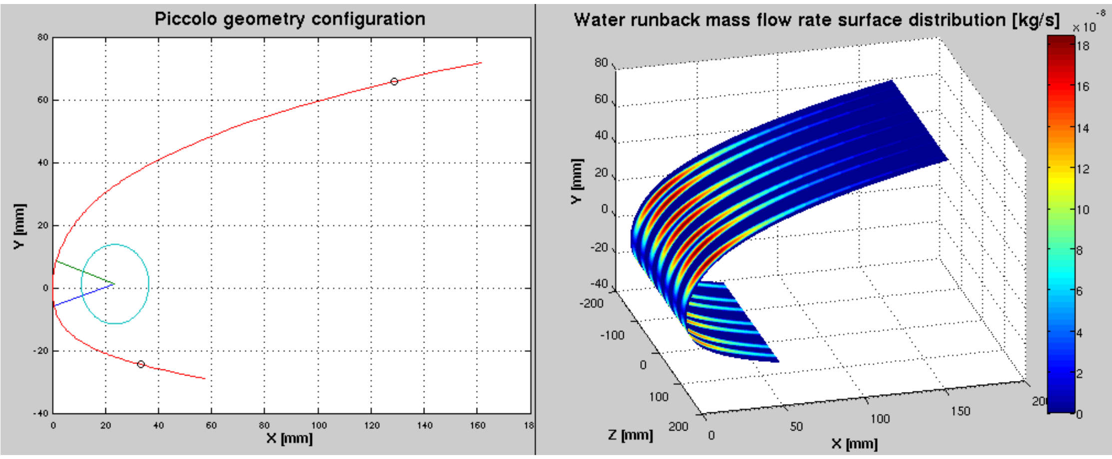

Figure 4-13: Optimal configuration obtained without POD and corresponding water runback.

As a concluding remark, it would be of great value to work on improving the accuracy of the POD-Kriging module especially for higher dimension. Moreover, the use of a hybrid optimization method combining genetic algorithms for the first phase of design space search to a gradient-based method in a second phase is to be investigated for a more efficient optimization framework. It would also most probably improve the repeatability of the methodology.

CONCLUSION AND FUTURE WORK

This work tries to bring some rigor to a field long governed by trial-and-error and empiricism. It presents an optimization methodology for anti-icing systems based on 3D CFD computations and combining powerful tools such as a genetic evolutionary algorithm, which is ideal for searching multi-dimensional design space, and a POD-based Reduced-Order Model allowing to greatly reducing the computational cost. Being thus affordable and modular, this optimization method is promising and adaptable to handle more complex 3D geometries and physics. This method was successfully applied and led to optimal geometric configurations for 3- to 5-dimensional design spaces, improving the initial generic design by up to 885%.

In terms of future developments, geometric shape and Piccolo power inputs variations in the spanwise direction can be taken into account, as well as wing tip and root effects. The ROM module can be upgraded to improve accuracy. Moreover, the correlation can be upgraded back to a 3D CFD computation, while the water film model could be replaced by the ICE3D module of FENSAP-ICE.

Concerning the handling of several design points (external conditions), the method can still be applied with an adaptation of the objective function to account for the additional constraints or with the construction of a Pareto front in a multi-objective optimization framework.

Further research could focus on applying the Reduced-Order Model directly to fully coupled computations constituting the snapshots, and running the genetic algorithm module with such a higher-fidelity POD model. An interesting future application would be to adapt this method to electro-thermal anti-icing systems.

In addition to the new technical skills that I acquired and perfected throughout this project, in thermodynamics, CFD, optimization and Reduced-Order Modelling, this experience constituted a personal challenge which I am particularly proud to have accomplished.

REFERENCES

[1] National Transportation Safety Board, *Annual Review of Aircraft Accident Data*, U.S. General Aviation, 2005.

[2] K. R. Petty, and C. D. J. Floyd, "A Statistical Review of Aviation Airframe Icing Accidents in the US," *11th ASM Conference on Aviation, Range, and Aerospace*, Hyannis, MA, USA, 2004.

[3] European Aviation Safety Agency, *Annual Safety Review 2007*, EASA, 2007.

[4] S. G. Cober, and G. A. Isaac, "Aircraft Icing Environments Observed In Mixed-Phase Clouds," *40th AIAA Aerospace Sciences Meeting and Exhibit*, AIAA-2002-675, Reno, NV, USA, 2002.

[5] Federal Aviation Administration, *General Aviation Safety Challenges 2008 - Part 2*, FAA, 2008.

[6] United States Department of Transportation, *In-Flight Aircraft Icing Plan*, FAA, 1997.

[7] Civil Aviation Authority of New Zealand, *Aircraft Icing Handbook*, Lower Hutt, New Zealand, 2000.

[8] I. Paraschivoiu, and M. T. Brahimi, *Aircraft In-Flight Icing*, Centre de Développement Technologique, École Polytechnique de Montréal, Montreal, QC, Canada, 1997.

[9] G. Mingione, and M. Barocco, *Flight in Icing Conditions Summary*, French DGAC, 1997.

[10] M. G. Potapczuk, "A Review of NASA Lewis' Development Plans for Computational Simulation of Aircraft Icing," *AIAA Paper*, AIAA–1999–243, 1999.

[11] J. Steuernagle, K. Roy, and D. Wright, *Safety Advisor : Aircraft Icing*, AOPA Air Safety Foundation, 2008.

[12] Federal Aviation Administration, *Airworthiness Standards: Transport Category Airplanes, Part 25, Appendix C*, FAA, 2007.

[13] European Aviation Safety Agency, *Certification Specifications for Large Aeroplanes CS-25, Appendix C*, EASA, 2003.

[14] Transport Canada. "Canadian Aviation Regulations 2009-2," http://www.tc.gc.ca/civilaviation/regserv/affairs/cars/menu.htm.

[15] K. E. Yeoman, "Efficiency of a Bleed Air Powered Inlet Icing Protective System," *32nd AIAA Aerospace Sciences Meeting and Exhibit*, AIAA-1994-717, Reno, NV, USA, 1994.

[16] R. M. Norris, K. J. Rumford, and D. S. Youd, *Anti-icing valve* United States Patent 4831819,to Avco Corporation (Providence, RI) 1989.

[17] K. M. Al-Khalil, T. G. Keith Jr., and K. J. De Witt, "New Concept in Runback Water Modeling for Anti-Iced Aircraft Surfaces," *Journal of Aircraft,* vol. 30, no. 1, pp. 41-49, 1993.

[18] K. M. Al-Khalil, T. G. Keith Jr., and K. J. De Witt, "Development of an Improved Model for Runback Water on Aircraft Surfaces," *Journal of Aircraft,* vol. 31, no. 2, pp. 271-278, 1994.

[19] G. Fortin, A. Ilinca, J.-L. Laforte, and V. Brandi, "New Roughness Computation Method and Geometric Accretion Model for Airfoil Icing," *Journal of Aircraft,* vol. 41, no. 1, pp. 119-127, 2004.

[20] G. Fortin, J.-L. Laforte, A. Ilinca, and V. Brandi, "Prediction of 2D Airfoil Ice Accretion by Bisection Method and by Rivulets and Beads Modeling," *39th Aerospace Sciences Meeting and Exhibit*, AIAA-2003-1076, Reno, NV, USA, 2003.

[21] B. L. Messinger, "Equilibrium Temperature of an Unheated Icing Surface as a Function of Airspeed," *Journal of Aeronautical Sciences,* vol. 20, no. 1, pp. 29-42, 1953.

[22] T. G. Myers, "Extension to the Messinger Model for Aircraft Icing," *AIAA Journal,* vol. 39, no. 2, pp. 211-218, 2001.

[23] T. G. Myers, J. P. F. Charpin, and S. J. Chapman, "The Flow and Solification of a Thin Fluid Film on an Arbitrary Three-Dimensional Surface," *Journal of Phisics of Fluids,* vol. 14, no. 8, pp. 2788-2803, 2002.

[24] T. G. Myers, and C. P. Thompson, "Modeling the Flow of Water on Aircraft in Icing Conditions," *AIAA Journal,* vol. 36, no. 6, pp. 1010-1013, 1998.

[25] C. N. Donatti, R. A. Silveira, C. R. Maliska, and A. F. C. da Silva, "Ice Accretion Simulation in Presence of a Hot Air Anti-Icing System," *19th COBEM International Congress of Mechanical Engineering*, Brasília, DF, Brazil, 2007.

[26] O. Harireche, P. Verdin, C. P. Thompson, and D. W. Hammond, “Explicit Finite Volume Modeling of Aircraft Anti-Icing and De-Icing,” *Journal of Aircraft,* vol. 45, no. 6, pp. 1924-1936, 2008.

[27] S. Kato, “Solution for Aircraft Anti-Icing System Simulation by a Modified Perturbation Method,” *Journal of Aircraft,* vol. 43, no. 2, pp. 544-554, 2006.

[28] G. A. Lima da Silva, O. de Mattos Silvares, and E. J. Godoy de Jesus Zerbini, "Simulation of an Airfoil Electro-Thermal Anti-Ice System Operating in Running Wet Regime," *43rd AIAA Aerospace Sciences Meeting and Exhibit*, AIAA 2005-1374, Reno, NV, USA, 2005.

[29] G. A. Lima da Silva, O. de Mattos Silvares, and E. J. Godoy de Jesus Zerbini, “Numerical Simulation of Airfoil Thermal Anti-Ice Operation, Part 1: Mathematical Modeling,” *Journal of Aircraft,* vol. 44, no. 2, pp. 627-634, 2007.

[30] G. A. Lima da Silva, O. de Mattos Silvares, and E. J. Godoy de Jesus Zerbini, “Numerical Simulation of Airfoil Thermal Anti-Ice Operation, Part 2: Implementation and Results,” *Journal of Aircraft,* vol. 44, no. 2, pp. 635-641, 2007.

[31] F. Morency, M. T. Brahimi, F. Tezok, and I. Paraschivoiu, "Hot Air Anti-Icing System Modelization in the Ice Prediction Code CANICE," *36th AIAA Aerospace Sciences Meeting and Exhibit*, AIAA-1998-192, Reno, NV, USA, 1998.

[32] F. Morency, F. Tezok, and I. Paraschivoiu, “Anti-Icing System Simulation Using CANICE,” *Journal of Aircraft,* vol. 36, no. 6, pp. 999-1006, 1999.

[33] F. Morency, F. Tezok, and I. Paraschivoiu, “Heat and Mass Transfer in the Case of Anti-Icing System Simulation,” *Journal of Aircraft,* vol. 37, no. 2, pp. 245-252, 2000.

[34] F. Saeed, “State-of-the-Art Aircraft Icing and Anti-Icing Simulation,” *ARA Journal,* vol. 2000-2002, no. 25-27, pp. 106-113, 2003.

[35] H. Wang, “3D Conjugate Heat Transfer Simulation of Aircraft Hot-Air Anti-Icing Systems,” Masters Thesis, Mechanical Engineering, McGill University, Montreal, QC, Canada, 2005.

[36] J. Lee, D. Rigby, W. Wright, and Y. Choo, "Analysis of Thermal Ice Protection System (TIPS) with Piccolo Tube using State-of-the-Art Software," *44th AIAA Aerospace Sciences Meeting and Exhibit*, AIAA-2006-1011, Reno, NV, USA, 2006.

[37] K. M. Al-Khalil, T. G. Keith Jr., and K. J. De Witt, “Icing Calculations on a Typical Commercial Jet Engine Inlet Nacelle,” *Journal of Aircraft,* vol. 34, no. 1, pp. 87-93, 1997.

[38] A. Pueyo, F. Mokhtarian, and F. Kafyeke, "Validation of a Hot-Air Anti-icing Simulation Code," *World Aviation Congress & Exposition, SAE*, Montreal, QC, Canada, 2003.

[39] F. Saeed, F. Morency, and I. Paraschivoiu, "Numerical Simulation of a Hot-Air Anti-Icing System," *38th AIAA Aerospace Sciences Meeting and Exhibit*, AIAA-2000-630, Reno, NV, USA, 2000.

[40] C. N. Aliaga Rivera, “An Unsteady Multiphase Approach to In-Flight Icing,” Maters Thesis, Mechanical Engineering, McGill University, Montreal, QC, Canada, 2008.

[41] K. Nakakita, S. Nadarajah, and W. G. Habashi, “Towards Real-Time Aero-Icing Simulation of Complete Aircraft, via FENSAP-ICE,” *Journal of Aircraft,* vol. 47, no. 1, pp. 96-109, 2010.

[42] H. Wang, P. Tran, W. G. Habashi, Y. Chen, M. Zhang, and L. Feng, "Anti-Icing Simulation in Wet Air of a Piccolo System using FENSAP-ICE," *2007 SAE Aircraft and Engine Icing International Conference*, Seville, Spain, 2007.

[43] H. Beaugendre, “A PDE-Based 3D Approach to In-Flight Ice Accretion,” Ph.D. Thesis, Mechanical Engineering, McGill University, Montreal, QC, Canada, 2003.

[44] Y. Bourgault, H. Beaugendre, and W. G. Habashi, “Development of a Shallow-Water Icing Model in FENSAP-ICE,” *Journal of Aircraft,* vol. 37, no. 4, pp. 640-646, 2000.

[45] G. F. Croce, W. G. Habashi, G. Guevremont, and F. Tezok, "3D Thermal Analysis of an Anti-Icing Device Using FENSAP-ICE," *36th AIAA Aerospace Sciences Meeting and Exhibit*, AIAA-1998-193, Reno, NV, USA, 1998.

[46] W. G. Habashi, “Recent Advances in CFD for In-Flight Icing Simulation,” *Japan Society of Fluid Mechanics,* vol. 28, no. 2, pp. 99-118, 2009.

[47] G. A. Lima da Silva, O. de Mattos Silvares, and E. J. Godoy de Jesus Zerbini, "Water Film Breakdown and Rivulets Formation Effects on Thermal Anti-Ice Operation Simulation," *9th AIAA/ASME Joint Thermophysics and Heat Transfer Conference*, AIAA-2006-3785, San Francisco, CA, USA, 2006.

[48] D. Wang, G. F. Naterer, and G. Wang, "Thermofluid Optimization of a Heated Helicopter Engine Cooling-Bay Surface," *Canadian Aeronautics and Space Journal,* vol. 49, no. 2, pp. 73-86, 2003.

[49] J. M. Brown, S. Raghunathan, J. K. Watterson, A. J. Linton, and D. Riordon, "Heat Transfer Correlation for Anti-Icing Systems," *Journal of Aircraft,* vol. 39, no. 1, pp. 65-70, 2002.

[50] B. S. de Mattos, and G. L. Oliveira, "Three-Dimensional Thermal Coupled Analysis of a Wing Slice Slat with a Piccolo Tube," *18th AIAA Applied Aerodynamics Conference*, AIAA-2000-3921, Denver, CO, USA, 2000.

[51] M. Fregeau, M. Gabr, F. Saeed, and I. Paraschivoiu, "Numerical Simulation of Heat Transfer from an Array of Hot-Air Jets Impinging on a 3D Concave Surface," *50th CASI Annual General Meeting & Conference*, Montreal, QC, Canada, 2003.

[52] M. Fregeau, F. Saeed, and I. Paraschivoiu, "Numerical Heat Transfer Correlation for Array of Hot-Air Jets Impinging on 3-Dimensional Concave Surface," *Journal of Aircraft,* vol. 42, no. 3, pp. 665-670, 2005.

[53] J. Hua, F. Kong, and H. H. T. Liu, "Unsteady Thermodynamic Computational Fluid Dynamics Simulations of Aircraft Wing Anti-Icing Operation," *Journal of Aircraft,* vol. 44, no. 4, pp. 1113-1117, 2007.

[54] J. Hua, and H. H. T. Liu, "Fluid Flow and Thermodynamic Analysis of a Wing Anti-Icing System," *Canadian Aeronautics and Space Journal, CASI,* vol. 51, no. 1, pp. 35-40, 2005.

[55] H. H. T. Liu, and J. Hua, "Three-Dimensional Integrated Thermodynamic Simulation for Wing Anti-Icing System," *Journal of Aircraft,* vol. 41, no. 6, pp. 1291-1297, 2004.

[56] S. Özgen, and M. Canibek, "Ice Accretion Simulation on Multi-Element Airfoils Using Extended Messinger Model," *Heat and Mass Transfer,* vol. 45, pp. 305-322, 2009.

[57] M. Papadakis, S.-H. Wong, H.-W. Yeong, S.-C. Wong, and G. T. Vu, "Icing Tunnel Experiments with a Hot Air Anti-Icing System," *46th AIAA Aerospace Sciences Meeting and Exhibit*, AIAA-2008-444, Reno, NV, USA, 2008.

[58] M. Papadakis, and S.-H. J. Wong, "Parametric Investigation of a Bleed Air Ice Protection System," *44th AIAA Aerospace Sciences Meeting and Exhibit*, AIAA-2006-1013, Reno, NV, USA, 2006.

[59] P. Planquart, G. Vanden Borre, and J.-M. Buchlin, "Experimental and Numerical Optimization of a Wing Leading Edge Hot Air Anti-icing System," *43rd AIAA Aerospace Sciences Meeting and Exhibit*, AIAA-2005-1277, Reno, NV, USA, 2005.

[60] D. Rigby, "Numerical Investigation of Hole Pattern Effect on Piccolo Tube Anti-Icing," *44th AIAA Aerospace Sciences Meeting and Exhibit*, AIAA-2006-1012, Reno, NV, USA, 2006.

[61] S. J. Riley, and E. H. James, "Investigations Relating to the Effects of Various Internal Geometries on the Effectiveness of an Aero-Engine Intake Thermal Anti-Icing System," *39th ASME International Gas Turbine & Aeroengine Congress & Exposition*, The Hague, Netherlands, 1994.

[62] F. Saeed, and A. Z. Al-Garni, "Numerical Simulation of Surface Heat Transfer from an Array of Hot-Air Jets," *Journal of Aircraft,* vol. 45, no. 2, pp. 700-714, 2008.

[63] E. A. Whalen, A. P. Broeren, M. B. Bragg, and S. Lee, "Characteristics of Runback Ice Accretions on Airfoils and their Aerodynamic Effects," *43rd AIAA Aerospace Science Meeting and Exhibit*, AIAA-2005-1065, Reno, NV, USA, 2005.

[64] S.-H. Wong, M. Papadakis, and A. Zamora, "Computational Investigation of a Bleed Air Ice Protection System," *1st AIAA Atmospheric and Space Environments Conference*, AIAA-2009-3966, San Antonio, Texas, USA, 2009.

[65] W. B. Wright, "An Evaluation of Jet Impingement Heat Transfer Correlations for Piccolo Tube Application," *42nd AIAA Aerospace Sciences Meeting and Exhibit*, AIAA-2004-62, Reno, NV, USA, 2004.

[66] R. J. Goldstein, A. I. Behbahani, and K. Kieger Heppelmann, "Streamwise Distribution of the Recovery Factor and the Local Heat Transfer Coefficient to an Impinging Circular Air Jet," *Int. J. Heat and Mass Transfer,* vol. 29, no. 8, pp. 1227-1235, 1986.

[67] R. Gardon, and J. C. Akfirat, "The Role of Turbulence in Determining the Heat-Transfer Characteristics of Impinging Jets," *Int. J. Heat and Mass Transfer,* vol. 8, pp. 1261-1272, 1965.

[68] K. Jambunathan, M. A. Moss, and B. L. Button, "A Review of Heat Transfer Data for Single Circular Jet Impingement," *Int. J. Heat and Fluid Flow,* vol. 13, no. 2, pp. 106-115, 1992.

[69] L. Huang, and M. S. El-Genk, "Heat Transfer of an Impinging Jet on a Flat Surface," *Int. J. Heat and Mass Transfer,* vol. 37, no. 13, pp. 1915-1923, 1994.

[70] A. A. Tawfek, "Heat Transfer and Pressure Distributions of an Impinging Jet on a Flat Plate," *Heat and Mass Transfer,* vol. 32, no. 1-2, pp. 49-54, 1996.

[71] M. Angioletti, R. M. Di Tommaso, E. Nino, and G. Ruocco, "Simultaneous Visualization of Flow Field and Evaluation of Local Heat Transfer by Transitional Impinging Jets," *Int. J. Heat and Mass Transfer,* vol. 46, no. 10, pp. 1703-1713, 2003.

[72] A. M. Huber, and R. Viskanta, "Effect of Jet-Jet Spacing on Convective Heat Transfer to Confined, Impinging Arrays of Axisymmetric Air Jets," *Int. J. Heat and Mass Transfer,* vol. 37, no. 18, pp. 2859-2869, 1994.

[73] D.-H. Rhee, P.-H. Yoon, and H. H. Cho, "Local Heat/Mass Transfer and Flow Characteristics of Array Impinging Jets with Effusion Holes Ejecting Spent Air," *Int. J. Heat and Mass Transfer,* vol. 46, no. 6, pp. 1049-1061, 2003.

[74] J.-Y. San, and M.-D. Lai, "Optimum Jet-to-Jet Spacing of Heat Transfer for Staggered Arrays of Impinging Air Jets," *Int. J. Heat and Mass Transfer,* vol. 44, no. 21, pp. 3997-4007, 2001.

[75] B. V. N. Rama Kumar, and B. V. S. S. S. Prasad, "Computational Flow and Heat Transfer of a Row of Circular Jets Impinging on a Concave Surface," *Heat and Mass Transfer,* vol. 44, no. 6, pp. 667-678, 2008.

[76] L. C. d. C. Santos, R. H. Domingos, R. B. Maria, and M. d. F. Leal, "Sensitivity Analysis of a Bleed Air Anti-Ice Thermal Model to Geometrical and Operational Parameters," *46th AIAA Aerospace Sciences Meeting and Exhibit*, AIAA-2008-445, Reno, NV, USA, 2008.

[77] F. Saeed, and I. Paraschivoiu, "Optimization of a Hot-Air Anti-Icing System," *41st AIAA Aerospace Sciences Meeting and Exhibit*, AIAA-2003-733, Reno, NV, USA, 2003.

[78] Bombardier Aerospace proprietary data, 2009.

[79] H.-S. Chung, and J. J. Alonso, "Multiobjective Optimization Using Approximation Model-based Genetic Algorithms," *10th AIAA/ISSMO Symposium on Multidisciplinary Analysis and Optimization*, AIAA-2004-4325, Albany, NY, USA, 2004.

[80] H. Arizono, and K. Isogai, "Application of Genetic Algorithm for Aeroelastic Tailoring of a Cranked-Arrow Wing," *Journal of Aircraft,* vol. 42, no. 2, pp. 493-499, 2005.

[81] A. Saario, A. Oksanen, and M. Ylitalo, "Combination of Genetic Algorithm and Computational Fluid Dynamics in Combustion Process Emission Minimization," *Combustion Theory and Modelling,* vol. 10, no. 6, pp. 1037-1047, 2006.

[82] Y. Tahara, S. Tohyama, and T. Katsui, "CFD-based Multi-Objective Optimization Method for Ship Design," *International Journal for Numerical Methods in Fluids,* vol. 52, no. 5, pp. 499-527, 2006.

[83] A. Kumar, A. J. Keane, P. B. Nair, and S. Shahpar, "Efficient Genetic Algorithm Based Robust Design Method for Compressor Fan Blades," *ASME 2005 International Design Engineering Technical Conferences & Computers and Information in Engineering Conference*, Long Beach, CA, USA, 2005.

[84] S. Jeong, M. Murayama, and K. Yamamoto, "Efficient Optimization Design Method Using Kriging Model," *Journal of Aircraft,* vol. 42, no. 2, pp. 413-420, 2005.

[85] L. Padovan, V. Pediroda, and C. Poloni, *Multi Objective Robust Design Optimization of Airfoils in Transonic Field*, pp. 283-295, Springer, 2005.

[86] R. A. Van den Braembussche, "Evolutive Methods : Theoretical Aspects & Definitions," *NATO Research and Technology Organization Lecture Series (AVT-167) on "Strategies for Optimization and Automated Design of Gas Turbine Engines"*, Montreal, Canada, October 26-27, 2009.

[87] I. Lepot, "Introduction and Terminology," *NATO Research and Technology Organization Lecture Series (AVT-167) on "Strategies for Optimization and Automated Design of Gas Turbine Engines"*, Montreal, Canada, October 26-27, 2009.

[88] L. Bernier, "A Genetic Algorithm with Self-Adaptive Niche Sizing," Masters Thesis, Computer Science, McGill University, 1995.

[89] P. Haroun, "Genetic Algorithm and Data Visualization," Masters Thesis, Computer Science, McGill University, 1997.

[90] K. F. Man, K. S. Tang, and S. Kwong, "Genetic Algorithms : Concepts and Applications," *IEEE Transactions on Industrial Electronics,* vol. 43, no. 5, pp. 519-534, 1996.

[91] M. Srinivas, and L. M. Patnaik, "Genetic Algorithms : A Survey," *Computer,* vol. 27, no. 6, pp. 17-26, 1994.

[92] D. Whitley, "A Genetic Algorithm Tutorial," *Statistics and Computing,* vol. 4, no. 2, pp. 65-85, 1994.

[93] R. A. Van den Braembussche, "Tuning of Optimization Strategies," *NATO Research and Technology Organization Lecture Series (AVT-167) on "Strategies for Optimization and Automated Design of Gas Turbine Engines"*, Montreal, Canada, October 26-27, 2009.

[94] J. Burkardt, M. Gunzburger, and H.-C. Lee, "POD and CVT-based Reduced-Order Modeling of Navier-Stokes Flows," *Computer Methods in Applied Mechanics and Engineering,* vol. 196, no. 1-3, pp. 337-355, 2006.

[95] G. Li, M. Li, S. Azarm, J. Rambo, and Y. Joshi, "Optimizing Thermal Design of Data Center Cabinets with a New Multi-Objective Genetic Algorithm," *Distributed and Parallel Databases,* vol. 21, no. 2-3, pp. 167-192, 2007.

[96] J. Favier, L. Cordier, A. Kourta, and A. Iollo, "Calibrated POD Reduced-Order Models of Massively Separated Flows in the Perspective of their Control," *ASME Joint U.S. - European Fluids Engineering Summer Meeting*, Miami, FL, USA, 2006.

[97] J. Rambo, and Y. Joshi, "Reduced Order Modeling of Steady Turbulent Flows Using the POD," *ASME Summer Heat Transfer Conference*, San Francisco, CA, USA, 2005.

[98] L. Sirovich, "Turbulence and the Dynamics of Coherent Structures - Part III : Dynamics and Scaling," *Quarterly of Applied Mathematics,* vol. 45, no. 3, pp. 583-590, 1987.

[99] R. F. Coelho, P. Breitkopf, and C. Knopf-Lenoir, "Model Reduction for Multidisciplinary Optimization - Application to a 2D Wing," *Structural and Multidisciplinary Optimization,* vol. 37, no. 1, pp. 29-48, 2008.

[100] I. Lepot, "Complements on Surrogate Based Optimization for Engineering Design," *NATO Research and Technology Organization Lecture Series (AVT-167) on "Strategies for Optimization and Automated Design of Gas Turbine Engines"*, Montreal, Canada, October 26-27, 2009.

[101] D. E. Raveh, "Computational-Fluid-Dynamics-Based Aeroelastic Analysis and Structural Design Optimization - a Researcher's Perspective," *Computer Methods in Applied Mechanics and Engineering,* vol. 194, no. 30-33, pp. 3453-3471, 2005.

[102] P. Bratley, and B. L. Fox, "Algorithm 659: Implementing Sobol's Quasirandom Sequence Generator," *ACM Transactions on Mathematical Software,* vol. 14, no. 1, pp. 88-100, 1988.

[103] A. Chang, I. Izmailov, S. Rizzo, S. Wynter, O. Alexandrov, and C. Tong, *Computer Experiments for Function Approximations*, Lawrence Livermore National Laboratory, Livermore, CA, USA, October 17, 2007.

[104] A. Isaacs, *Sampling Strategies for Computer Experiments*, January 2004.

[105] S. Joe, and F. Y. Kuo, "Remark on Algorithm 659: Implementing Sobol's Quasirandom Sequence Generator," *ACM Transactions on Mathematical Software,* vol. 29, no. 1, pp. 49-57, 2003.

[106] I. M. Sobol, "On the Systematic Search in a Hypercube," *SIAM Journal on Numerical Analysis,* vol. 16, no. 5, pp. 790-793, 1979.

[107] R. B. Statnikov, and J. B. Matusov, *Multicriteria Optimization and Engineering*, p. 212, New York: Chapman & Hall, 1995.

[108] A. Chatterjee, "An Introduction to the Proper Orthogonal Decomposition," *Current Science,* vol. 78, no. 7, pp. 808-817, 2000.

[109] P. Holmes, J. L. Lumley, and G. Berkooz, *Turbulence, Coherent Structures, Dynamical Systems and Symmetry*, pp. 86-117, New York: Cambridge University Press, 1996.

[110] Y. C. Liang, H. P. Lee, S. P. Lim, W. Z. Lin, K. H. Lee, and C. G. Wu, "Proper Orthogonal Decomposition and its Applications - Part 1 : Theory," *Journal of Sound and Vibration,* vol. 252, no. 3, pp. 527-544, 2002.

[111] L. Sirovich, "Turbulence and the Dynamics of Coherent Structures - Part I : Coherent Structures," *Quarterly of Applied Mathematics,* vol. 45, no. 3, pp. 561-571, 1987.

[112] K. Nakakita, "Toward Real-Time Aero-Icing Simulation Using Reduced Order Models," Mechanical Engineering, McGill, Spring 2007.

[113] K. Nakakita, S. Nadarajah, and W. G. Habashi, "Towards Real-Time Aero-Icing Simulation of Complete Aircraft, via FENSAP-ICE," *Journal of Aircraft,* vol. 47, no. 1, pp. 96-109, January-February 2010.
[114] V. Lappo, "POD-Kriging Approximations of Multi-Disciplinary CFD Simulation with Application to In-Flight Icing," Mechanical Engineering, McGill, Montreal, Spring 2010.
[115] V. Lappo, and W. G. Habashi, "POD-Kriging Approximations of Multi-Disciplinary CFD Simulation with Application to In-Flight Icing," *17th Annual Conference of the CFD Society of Canada*, CFDSC2009-6E3, Ottawa, ON, Canada, 2009.
[116] B. D. Matheis, and A. P. Rothmayer, "Numerical Simulation of Thin Air Driven Films," *40th AIAA Aerospace Sciences Meeting and Exhibit*, AIAA-2002-525, Reno, NV, USA, 2002.

APPENDIX A

A. SENSITIVITY ANALYSIS OF THE IMPACT OF WALL TEMPERATURE

A.1. On External Flow

A sensitivity analysis was performed in order to assess the impact of the wall boundary condition temperature level on the flow variables involved in the icing phenomena.

For the same set of external conditions, different constant temperature distributions (270 K to 300 K in increments of 5 K, and adiabatic wall condition, for a free-stream temperature of 265 K) were imposed as wall boundary condition, as illustrated in Figure A-1.

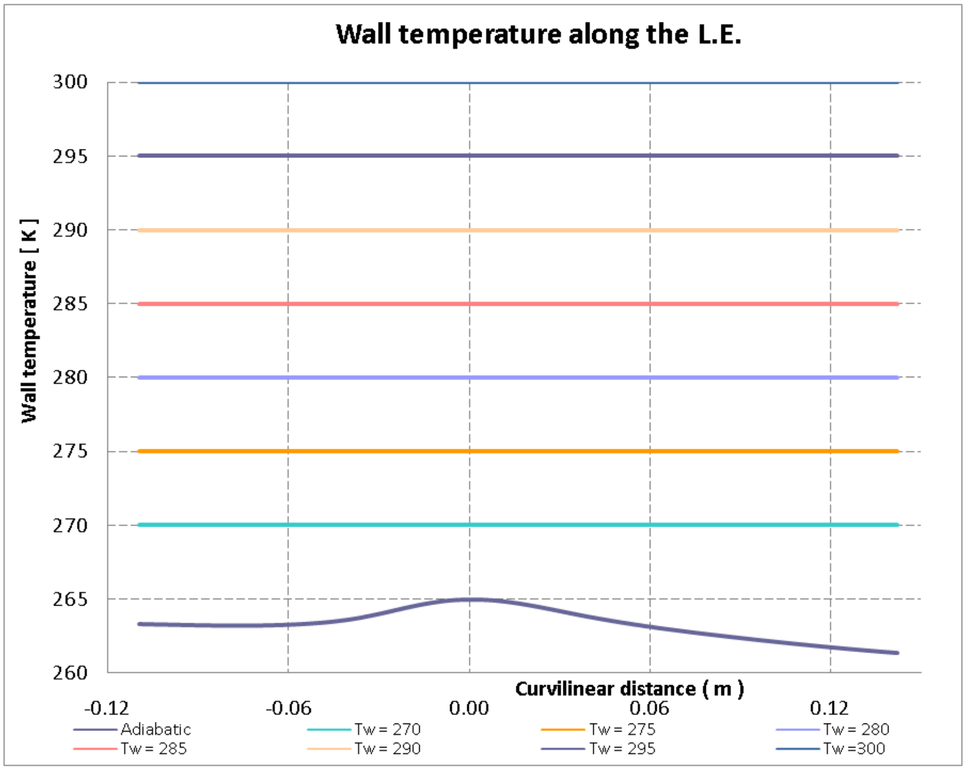

Figure A-1. Imposed wall temperature boundary conditions.

The following figures show the different relevant flow variable distributions extracted along a 2D cut on the slat's surface, tangent to the free-stream.

The pressure distribution at the wall is negligibly affected, as shown in Figure A-2. The wall shear stress seems to be slightly more impacted, as shown in Figure A-3, but the range of variations is contained within ±6% which is acceptable.

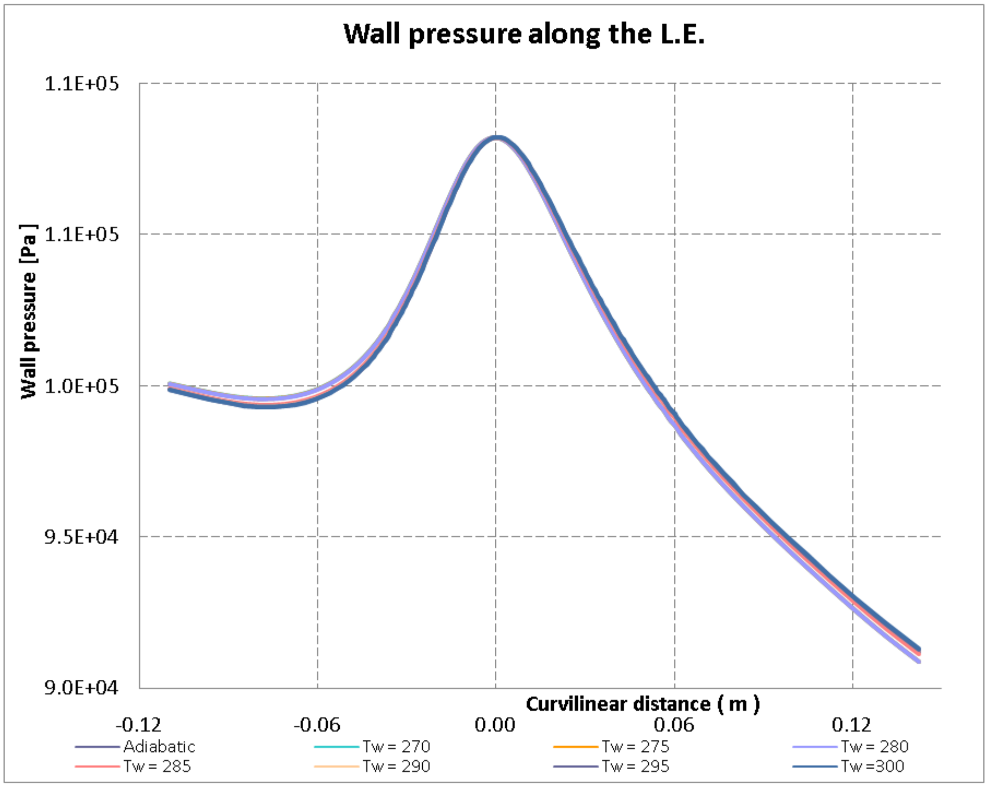

Figure A-2. Wall pressure distribution along the skin.

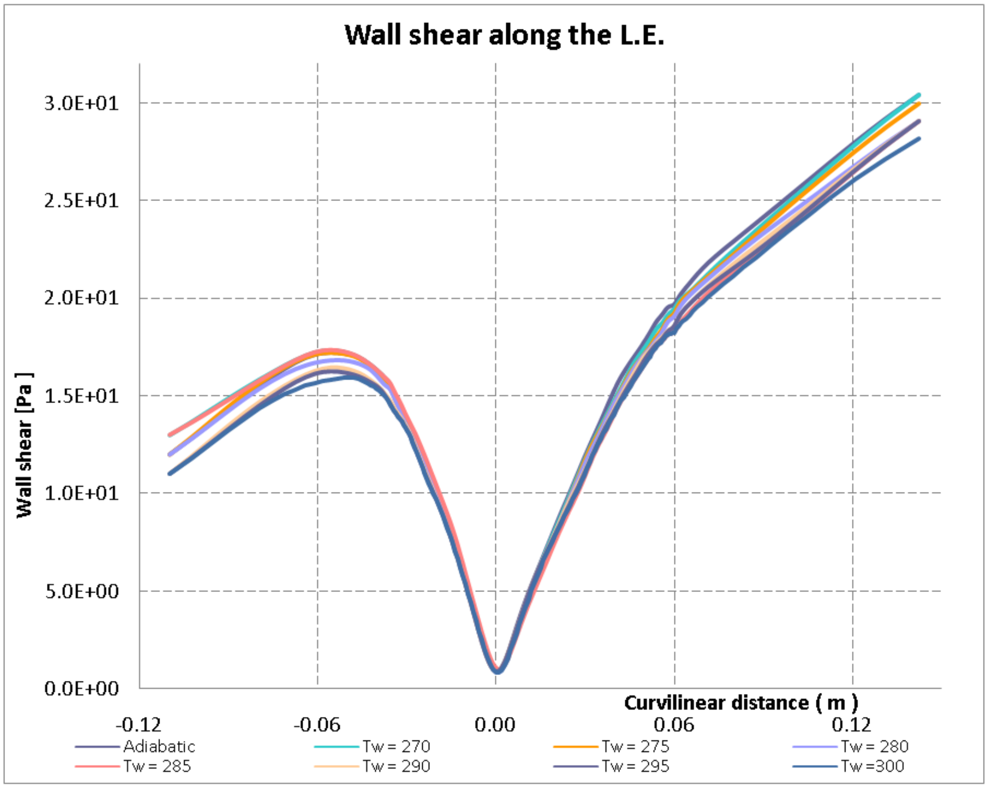

Figure A-3. Wall shear stress distribution along the skin.

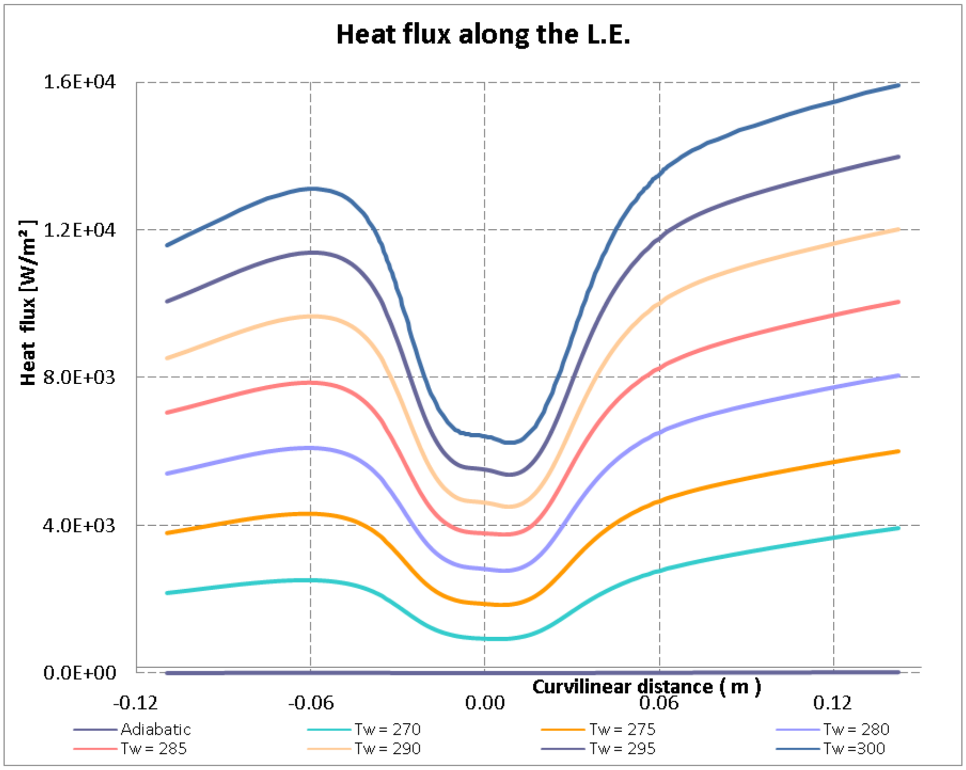

Figure A-4. Convective heat flux distribution along the skin.

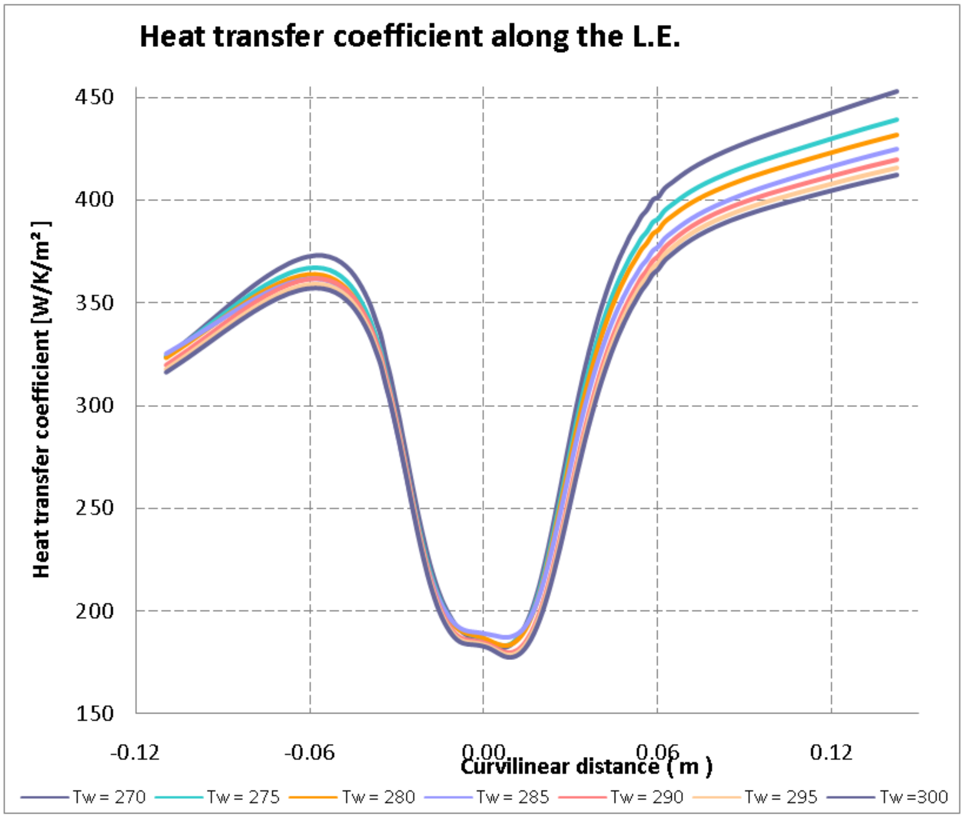

Figure A-5. Heat transfer coefficient distribution along the skin.

The convective heat flux distribution is obviously affected since the higher the temperature at the wall, the higher the convective heat flux, as shown in Figure A-4. The interesting aspect concerns the heat transfer coefficient distribution, computed from the convective heat flux, divided by the difference between local wall temperature and local adiabatic temperature. It is interesting to notice that the higher the temperature difference between imposed and free-stream temperatures, the lower the impact on the heat transfer coefficient distribution, as shown in Figure A-5. From a maximum error of about 10% for a temperature difference of 5 K, the distribution seems to converge towards a settled distribution, within ±0.5% after a temperature difference of 30 K. Therefore, the external flow will be considered unaffected as long as a temperature difference of at least 30 K is emphasized.

With respect to the variable related to the droplet impingement calculation, namely the local liquid water content, collection efficiency and impinging mass flux distributions, the impact of wall temperature level is negligible as illustrated in Figure A-6, Figure A-7 and Figure A-8.

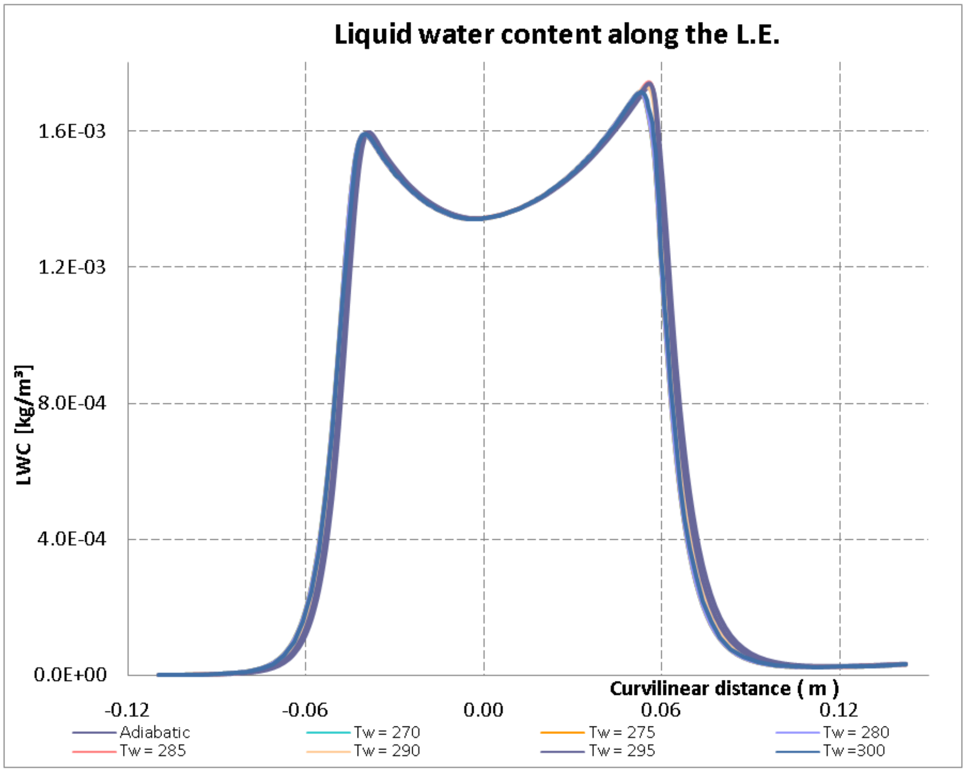

Figure A-6. Local liquid water content distribution along the skin.

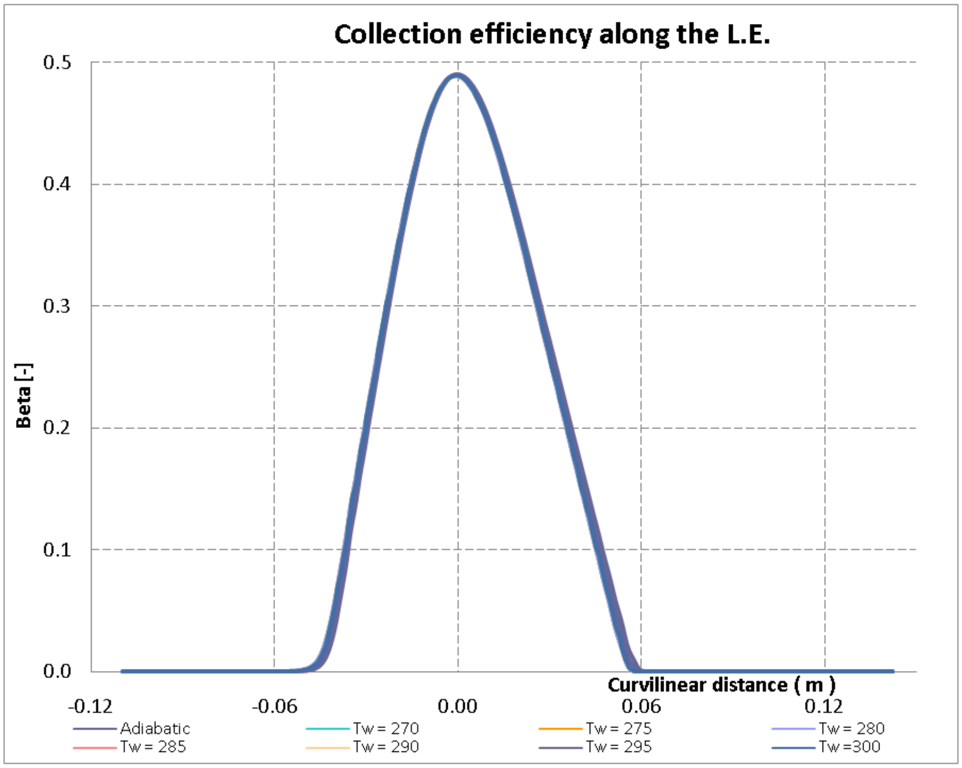

Figure A-7. Collection efficiency distribution along the skin.

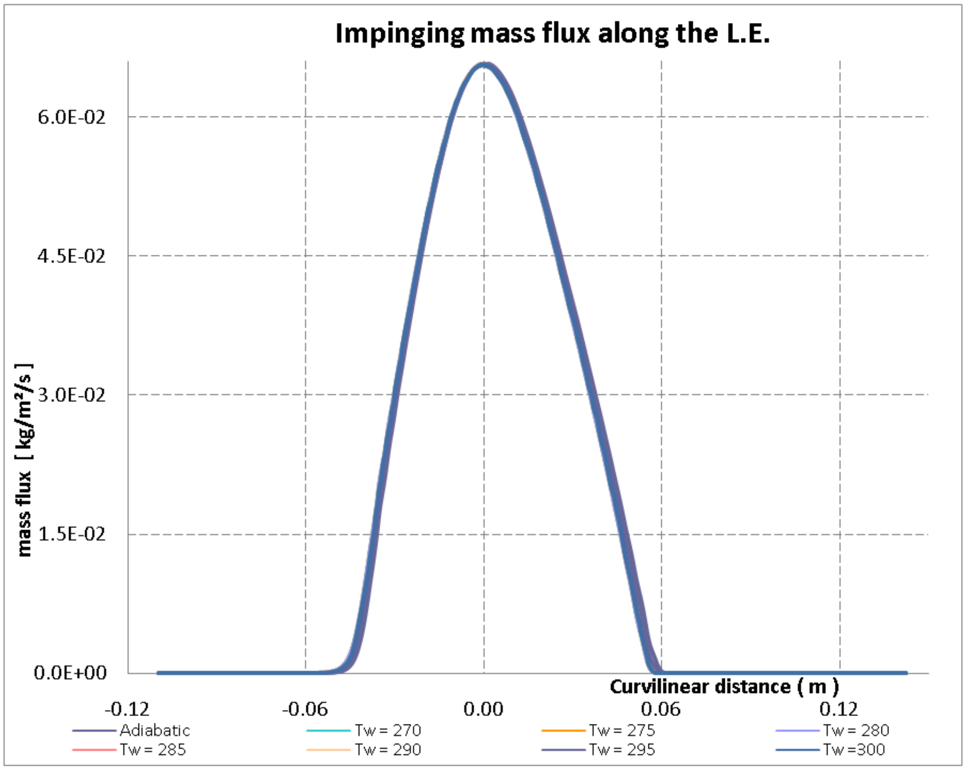

Figure A-8. Impingement mass flux distribution along the skin.

A.2. On Internal Flow

Having in mind the recommendations from the external flow sensibility study, the focus was oriented towards the impact on the internal heat transfer coefficient distribution in order to have an idea of the error implied by the "uncoupling" assumption. Thus, different wall temperature boundary conditions were imposed for three test cases of 3D internal flow, as shown in Figure A-9:

1. a constant distribution at temperature level 288K
2. a constant distribution at temperature level 350K
3. a distribution somewhat similar to the temperature distribution obtained after solving for the water film

In this case, the reference temperature is not the free-stream temperature nor the adiabatic distribution but the Piccolo inlet temperature.

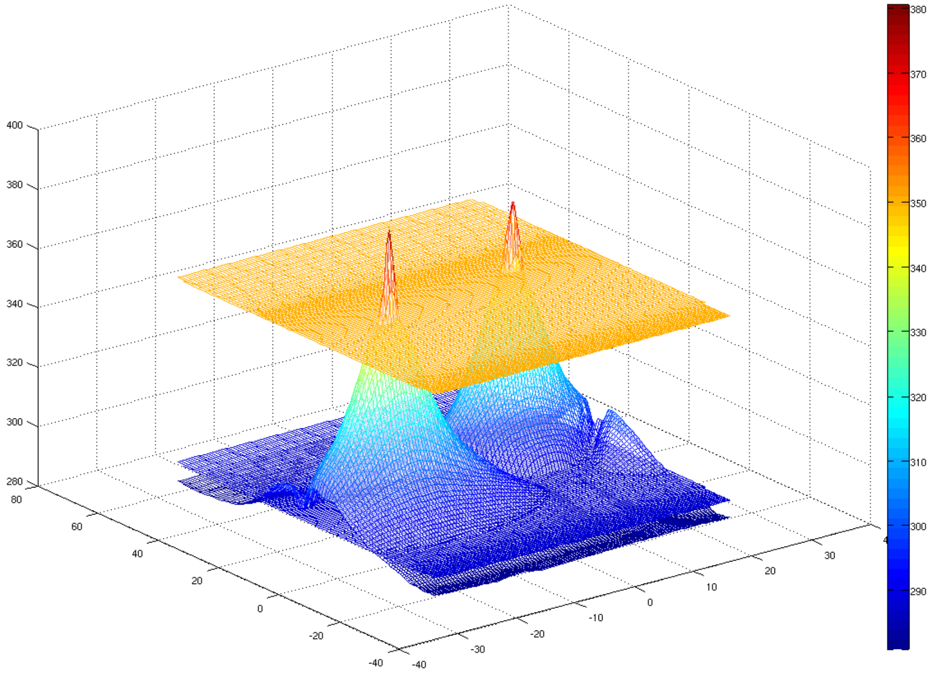

Figure A-9. Temperature boundary condition on the inner skin wall.

Figure A-10, Figure A-12 and Figure A-14 show the superposition of the heat transfer coefficient distributions two by two, one in colors and the other one in black.

Figure A-11, Figure A-13 and Figure A-15 present the relative error distributions. The maximum discrepancies are located at the neighboring of the jets stagnation points but do not exceed 12% then quickly drops below 2%, for the two extreme cases (cases 1 & 3) as shown in Figure A-11. Otherwise, it stands lower than 8% at the picks and also quickly drops below 2%, as shown in Figure A-13 and Figure A-15.

These results satisfactorily validate the “uncoupling” assumption with reasonably low impact on the internal heat transfer coefficient distribution.

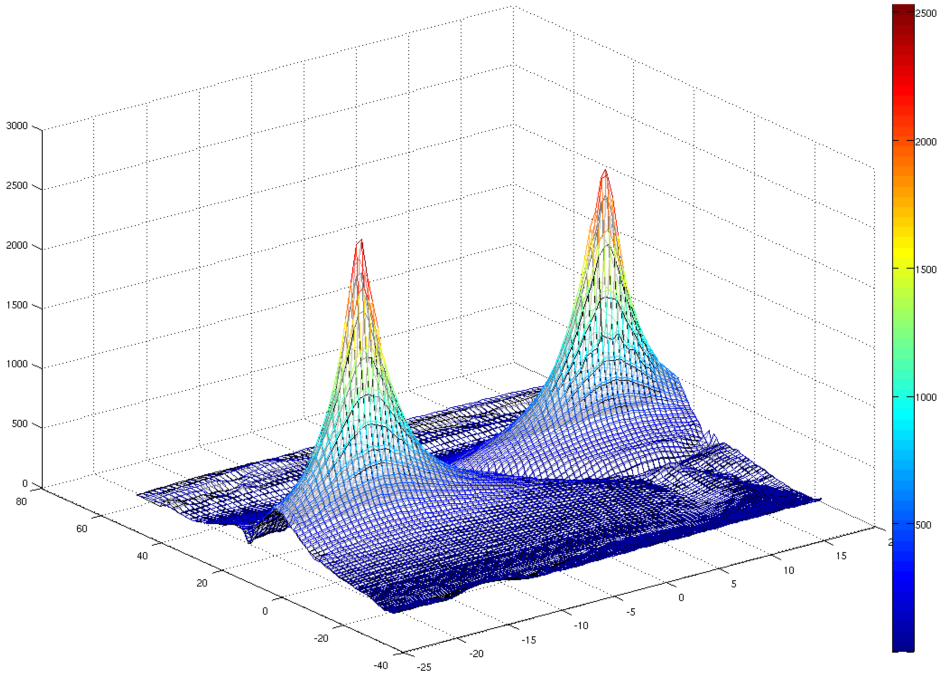

Figure A-10. Heat transfer coefficient distribution on the inner skin wall for cases 1 & 3.

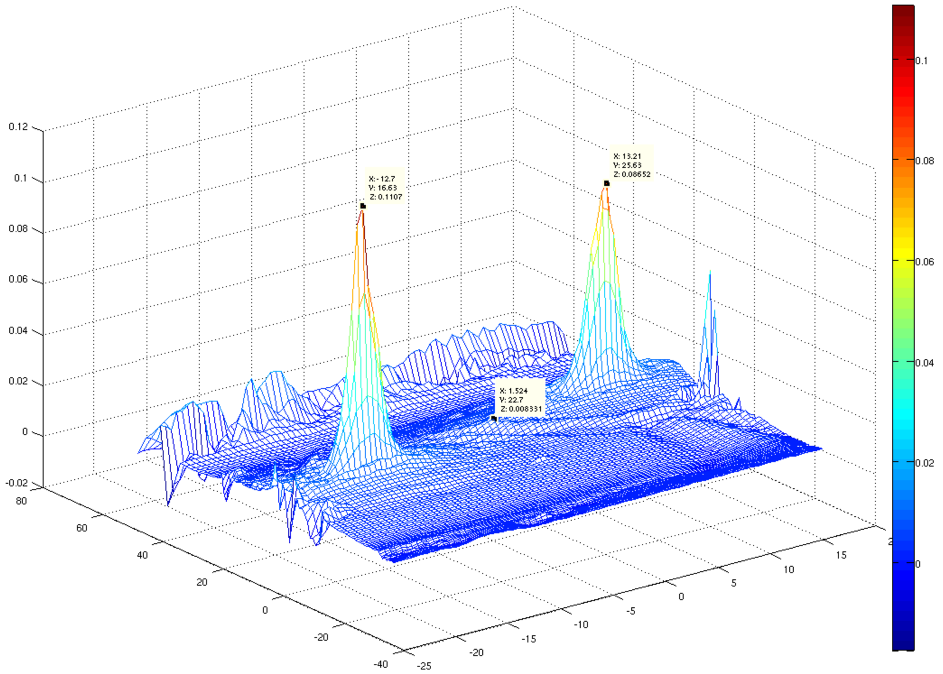

Figure A-11. Relative error distribution on the inner skin wall for cases 1 & 3.

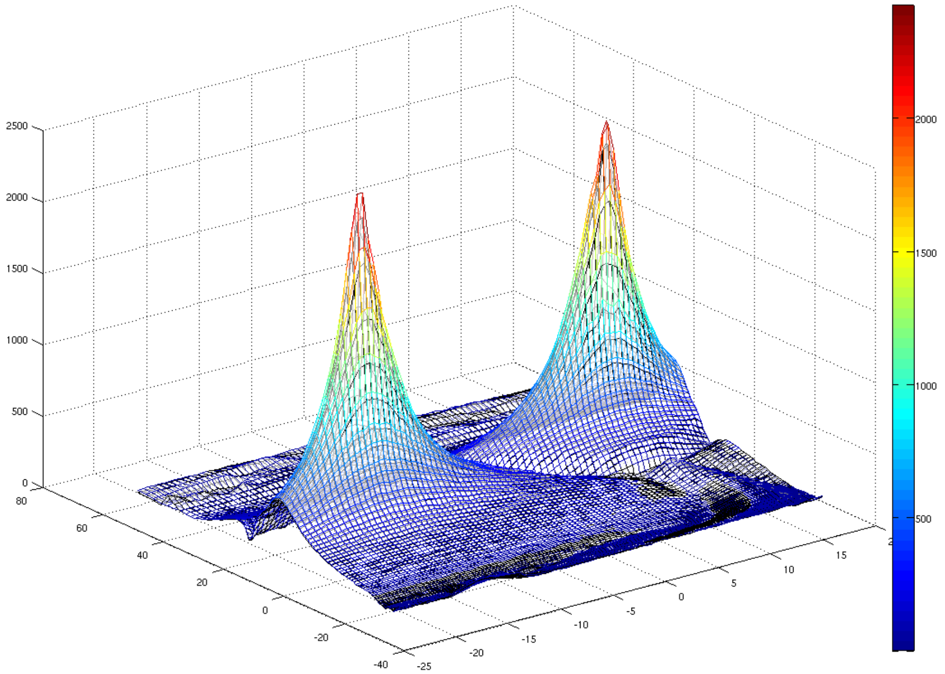

Figure A-12. Heat transfer coefficient distribution on the inner skin wall for cases 1 & 2.

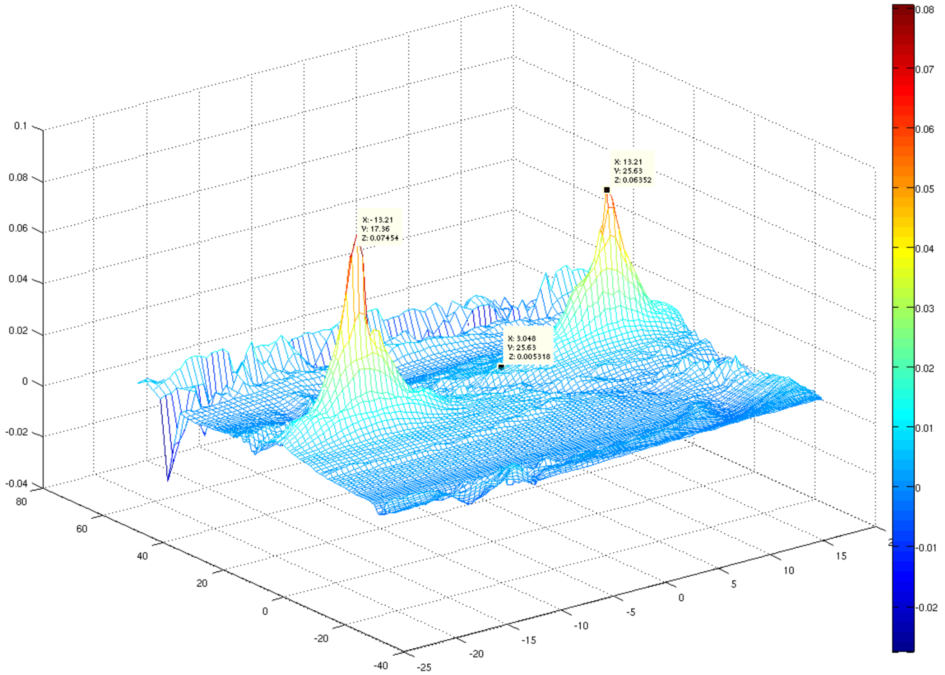

Figure A-13. Relative error distribution on the inner skin wall for cases 2 & 3.

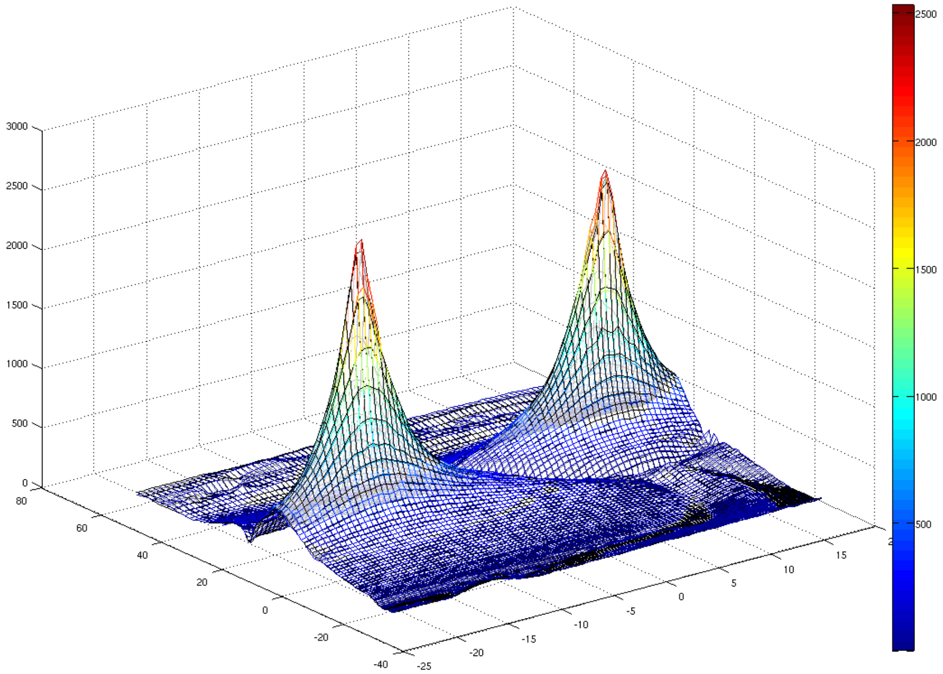

Figure A-14. Heat transfer coefficient distribution on the inner skin wall for cases 2 & 3.

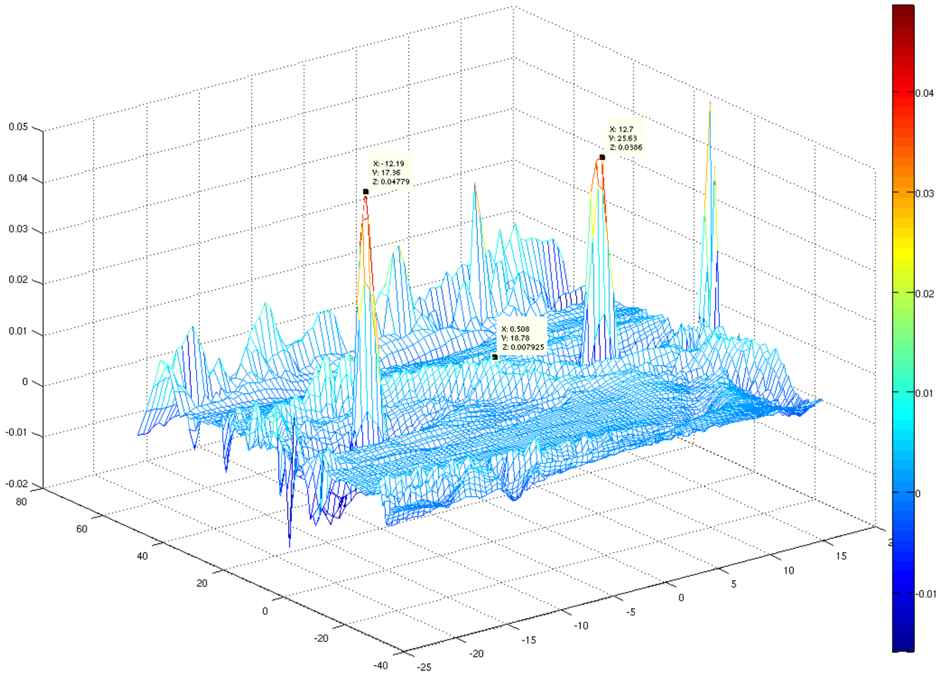

Figure A-15. Relative error distribution on the inner skin wall for cases 1 & 2.

APPENDIX B

B. 3D-CFD-BASED HEAT TRANSFER COEFFICIENT CORRELATION

As mentioned in section 3.2.3, the internal flow computation was replaced by a Heat Transfer Coefficient (HTC) correlation in order to efficiently save computational time and get a reasonably cost-efficient optimization framework. The original average Nusselt number correlation (cf. Equation (1)) was taken from the literature [36, 65-66].

$$\overline{Nu}\Big\|_0^r = \mathrm{Re}^{0.76}\cdot\left(24-\left|\left(z_n/d\right)-7.75\right|\right)\Big/\left(533+44\cdot\left(r/d\right)^{1.285}\right) \tag{1}$$

However, as shown in Figure B-1, this flat-plate-based correlation would not correspond to the reality of the actual problem (correlation is shown in colors and CFD results superimposed in black). These discrepancies would have a non-negligible impact on the water runback results, especially the water film thickness as shown in Figure B-2. Therefore, new average and local Nusselt number correlations (cf. Equation (2) and Equation (3)) were proposed based on the original correlation and fitted to 3D internal flow CFD computations using FENSAP. The correlated heat transfer coefficients were recovered from the Nusselt number expression as mentioned in Equation (4). Concerning the internal flow computation, the heat transfer coefficients are obtained from the Gresho convective heat flux computed at the wall and the temperature difference between the reference Piccolo temperature and the local wall temperature, as presented in Equation (5).

$$\overline{Nu}\Big\|_0^r = \mathrm{Re}^{0.76}\cdot\mathrm{Pr}^{0.42}\cdot\left(33-2.8\cdot z_n/d\right)\Big/\left(533+44\cdot\left(r/d\right)^{1.285}\right) \tag{2}$$

$$Nu_r = \left[r/\left(2\cdot dr\right)\cdot\left(\left(1+dr/r\right)^2\cdot\overline{Nu}\Big\|_0^{r+dr}-\overline{Nu}\Big\|_0^r\right)\right]\cdot\left[z_n/15+\left(2.6-z_n/15\right)\cdot e^{-0.25\cdot r}\right] \tag{3}$$

$$h_{c\,\mathrm{int}}\left(r\right)=Nu_r\cdot k/d \tag{4}$$

$$h_{c\,int}=\frac{q_{c\,\mathrm{int}}}{\left(T_{Pic}-T_w\right)} \tag{5}$$

Figure B-3 and Figure B-4 present how the original correlation and the new correlation respectively vary with normal distance and radial distance. The variation with normal distance was smoothed by introducing a quadratic term, and the variation with radial distance was sharpened using an exponential term.

The following figures (Figure B-5 to Figure B-20) compare the heat transfer coefficient distribution computed by CFD (in colors) to the one computed by the new correlation (in black), for each of the 8 different geometric configurations tested, which consisted in a combination of three jet angle configurations, three jet mass flow rate configurations and 8 Piccolo tube locations (for a jet-to-surface normal distance between 8.05 mm and 16.96 mm).

The fit with respect to CFD computations was highly enhanced, thus improving the consistency of the model. The error would generally be between 3% and 17%, sometimes locally higher at the stagnation point but would be less than 31% in the worst case.

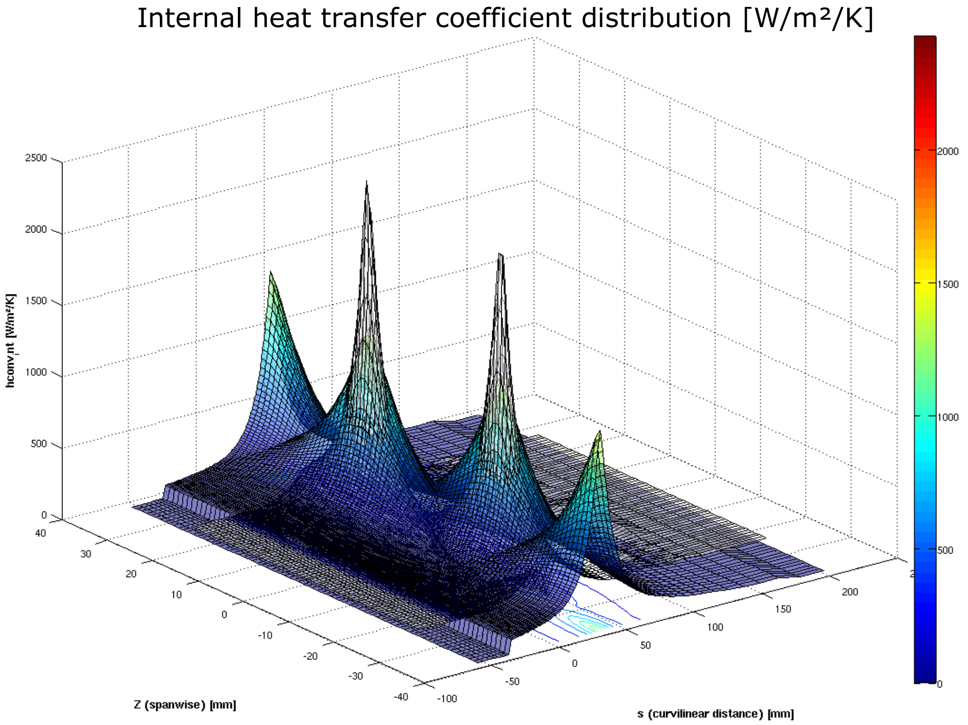

Figure B-1. Heat transfer coefficient distributions from original correlation vs. CFD.

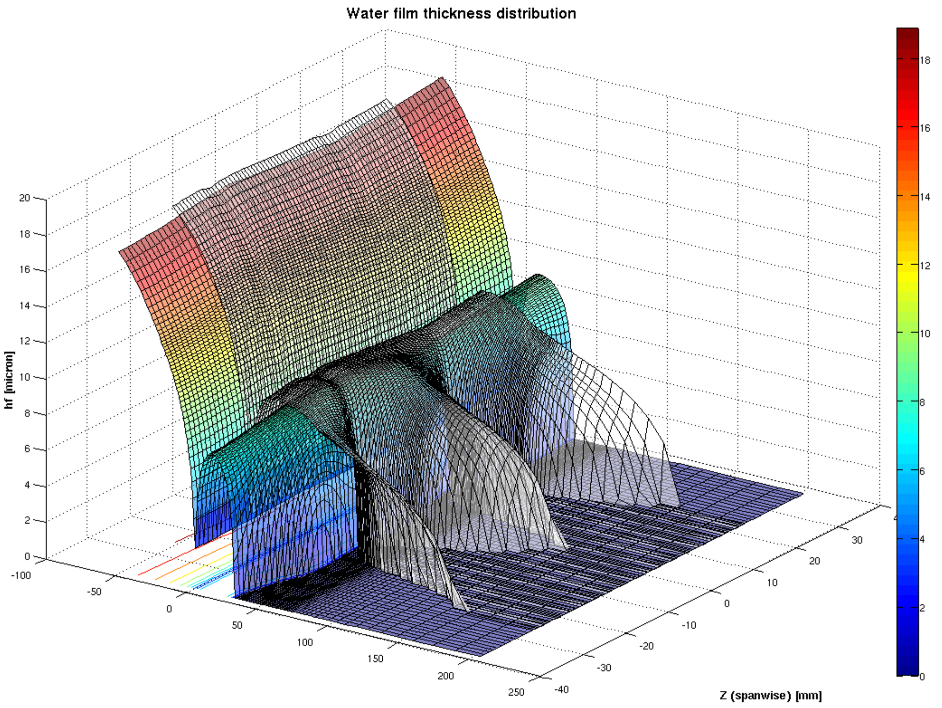

Figure B-2. Water film thickness distributions with HTC from original correlation vs. CFD.

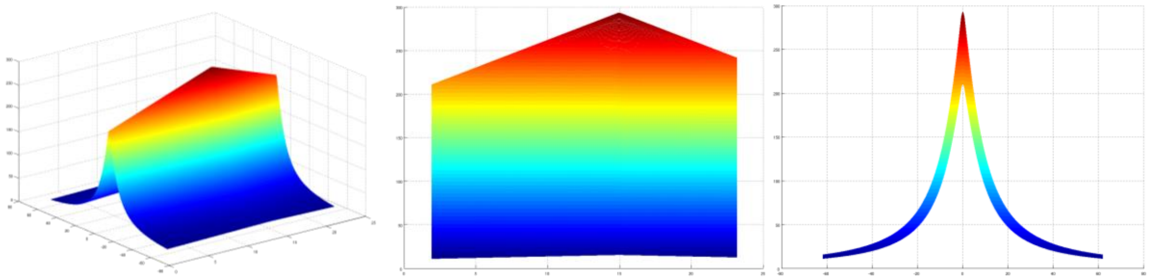

Figure B-3. Original correlation variations with normal distance and radial distance.

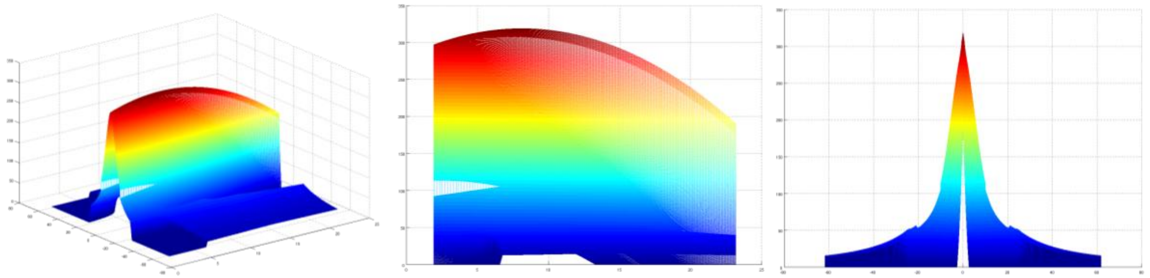

Figure B-4. New correlation variations with normal distance and radial distance.

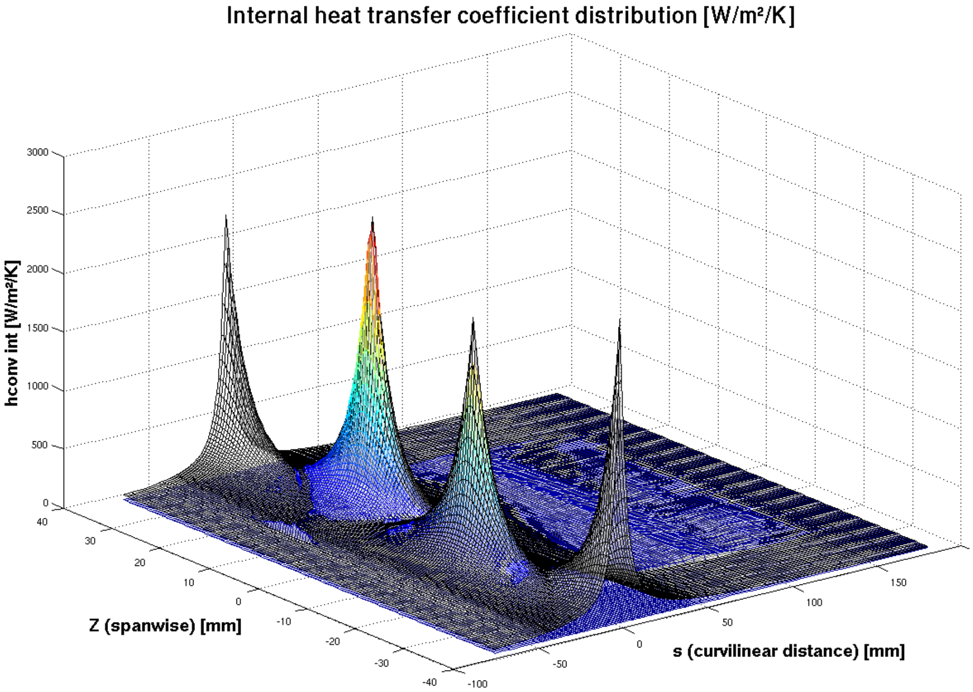

Figure B-5. HTC distributions from new correlation vs. CFD, case # 1.

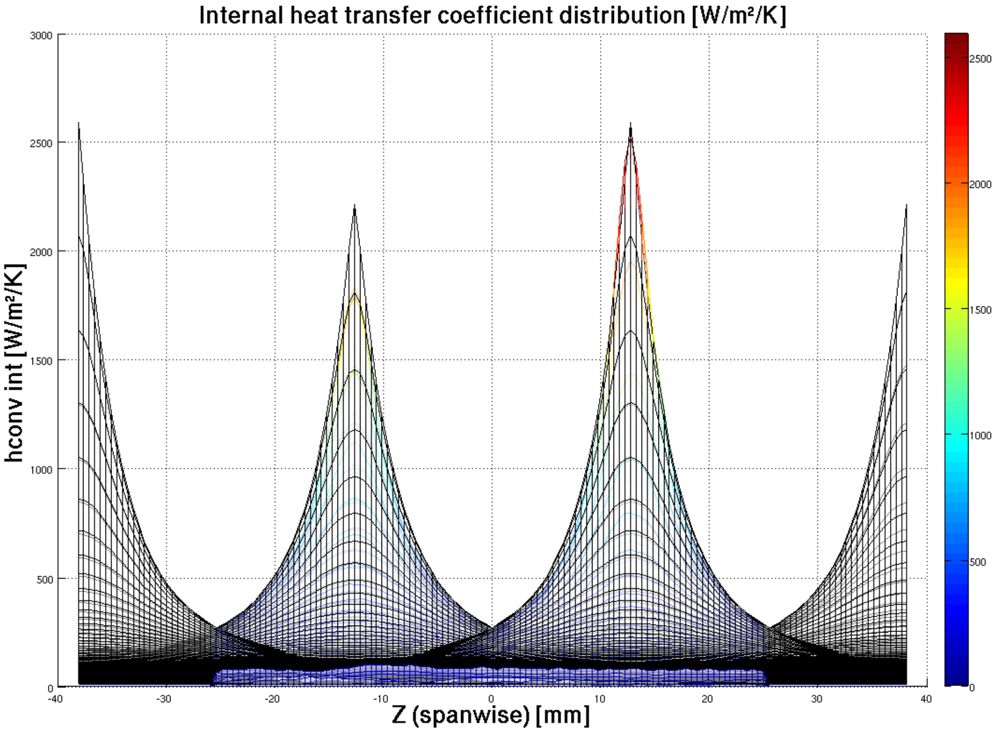

Figure B-6. HTC distributions from new correlation vs. CFD, case # 1 (close-up).

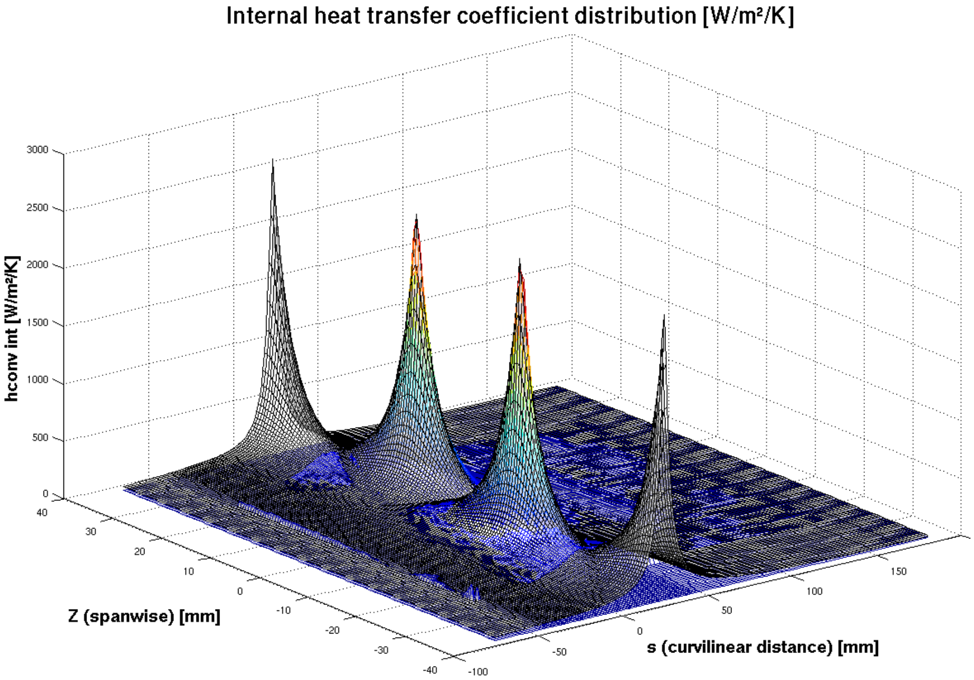

Figure B-7. HTC distributions from new correlation vs. CFD, case # 2.

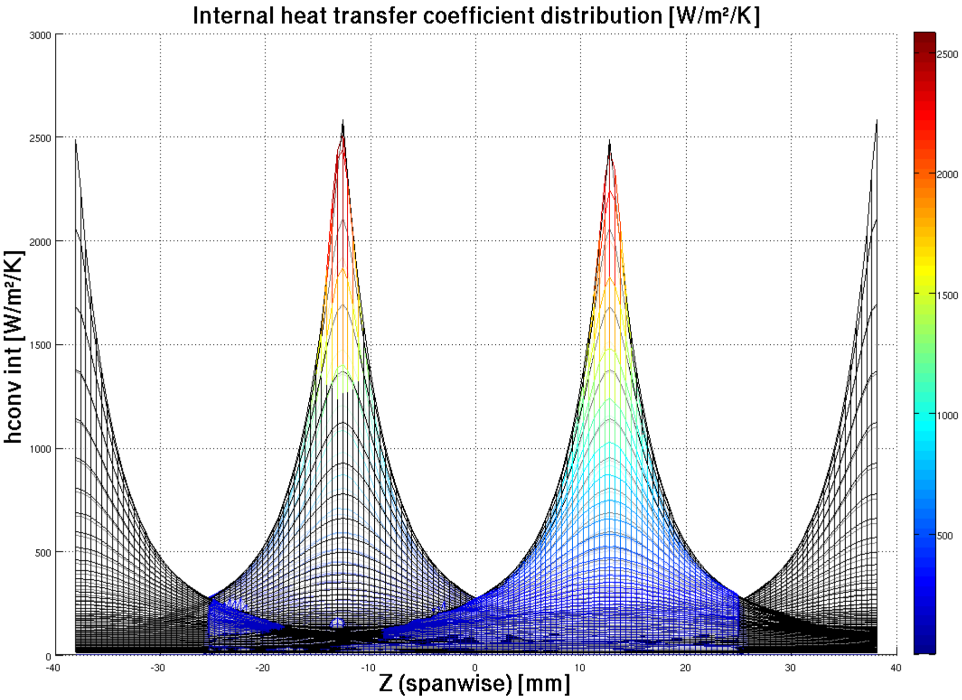

Figure B-8. HTC distributions from new correlation vs. CFD, case # 2 (close-up).

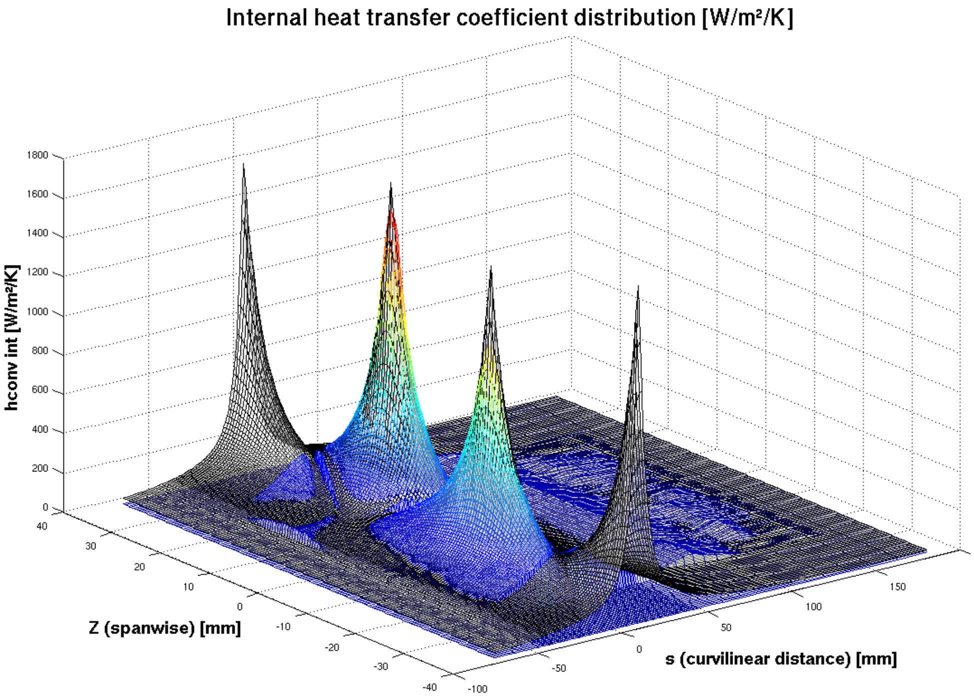

Figure B-9. HTC distributions from new correlation vs. CFD, case # 3.

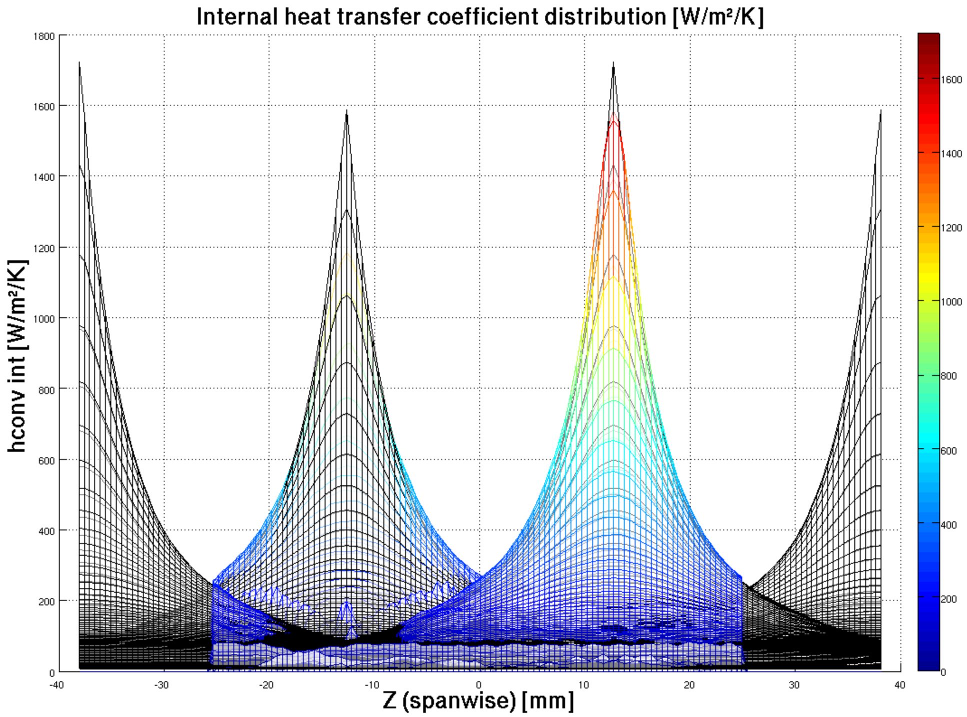

Figure B-10. HTC distributions from new correlation vs. CFD, case # 3 (close-up).

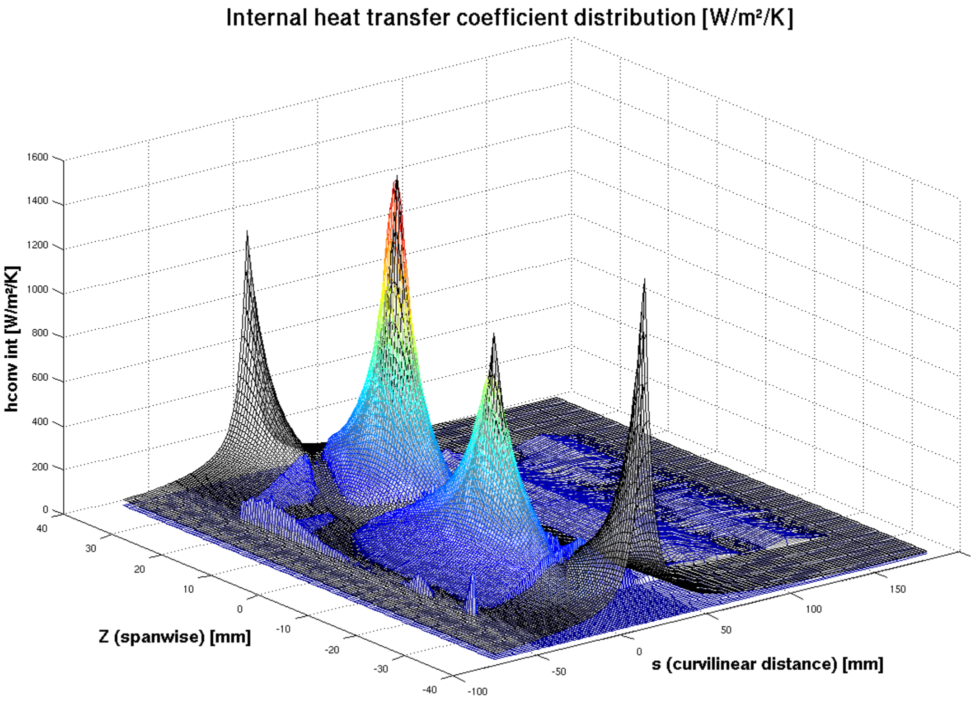

Figure B-11. HTC distributions from new correlation vs. CFD, case # 4.

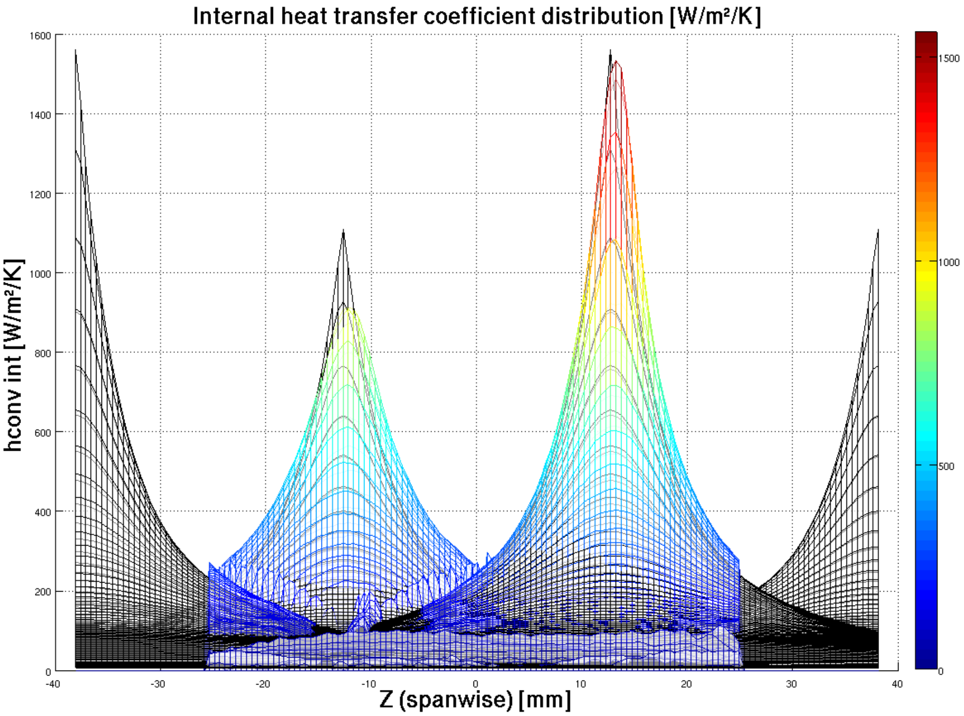

Figure B-12. HTC distributions from new correlation vs. CFD, case # 4 (close-up).

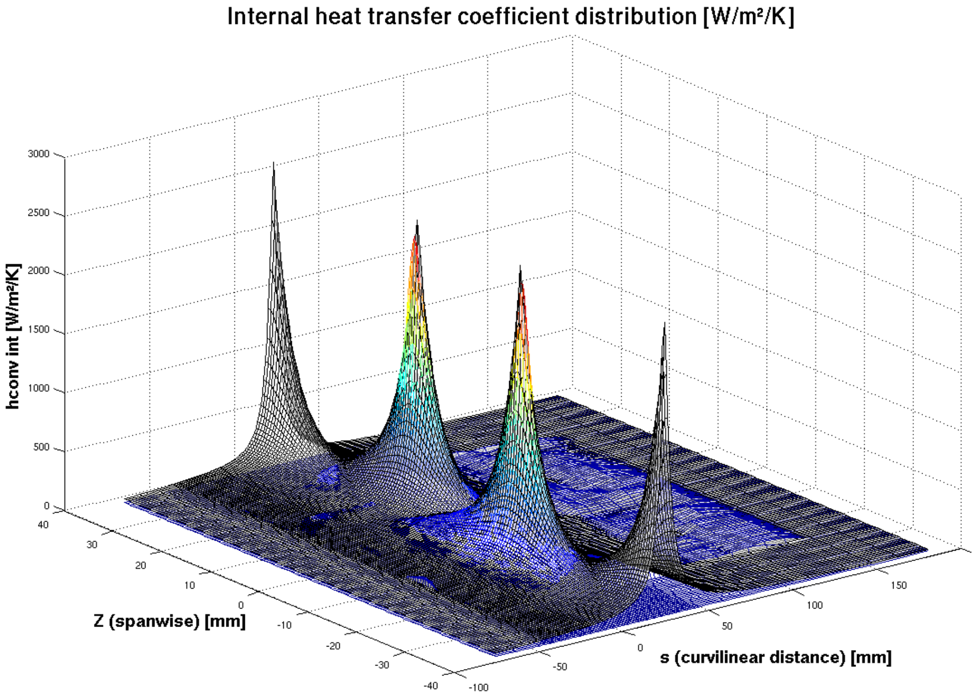

Figure B-13. HTC distributions from new correlation vs. CFD, case # 5.

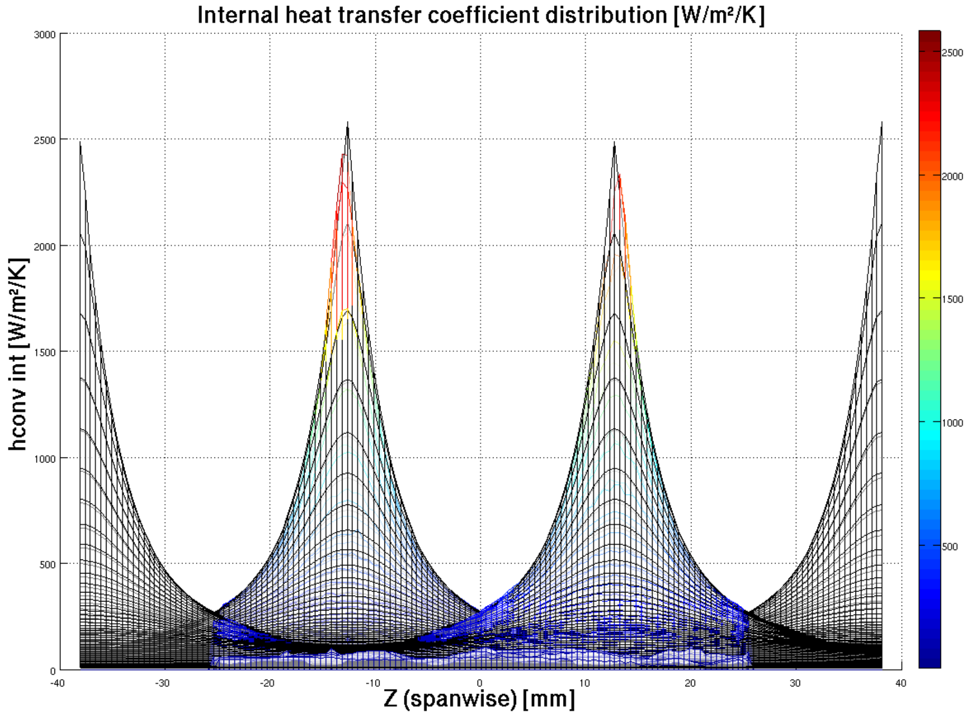

Figure B-14. HTC distributions from new correlation vs. CFD, case # 5 (close-up).

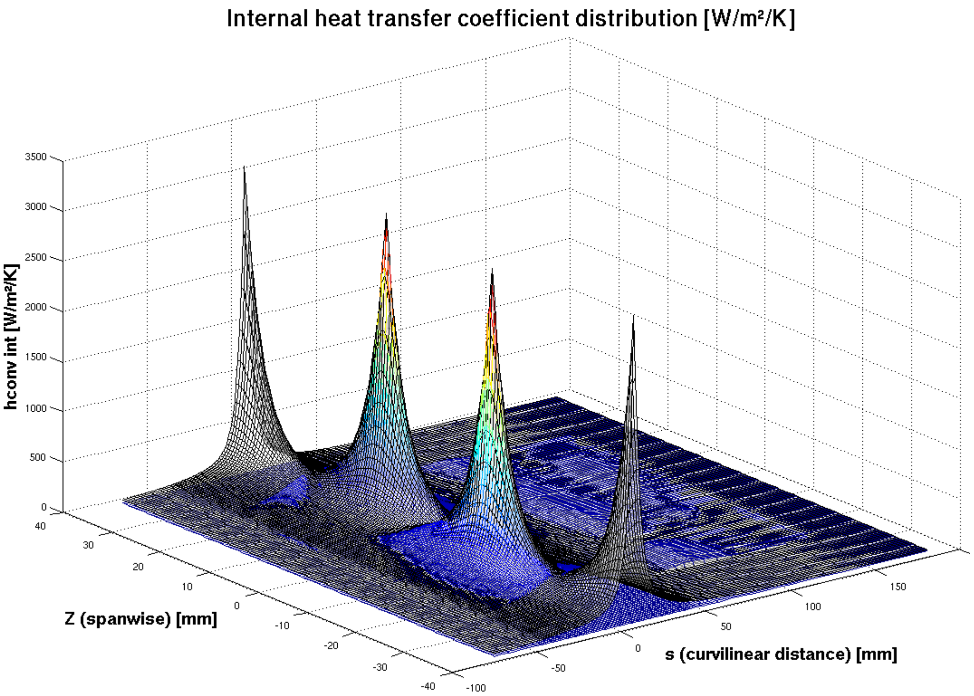

Figure B-15. HTC distributions from new correlation vs. CFD, case # 6.

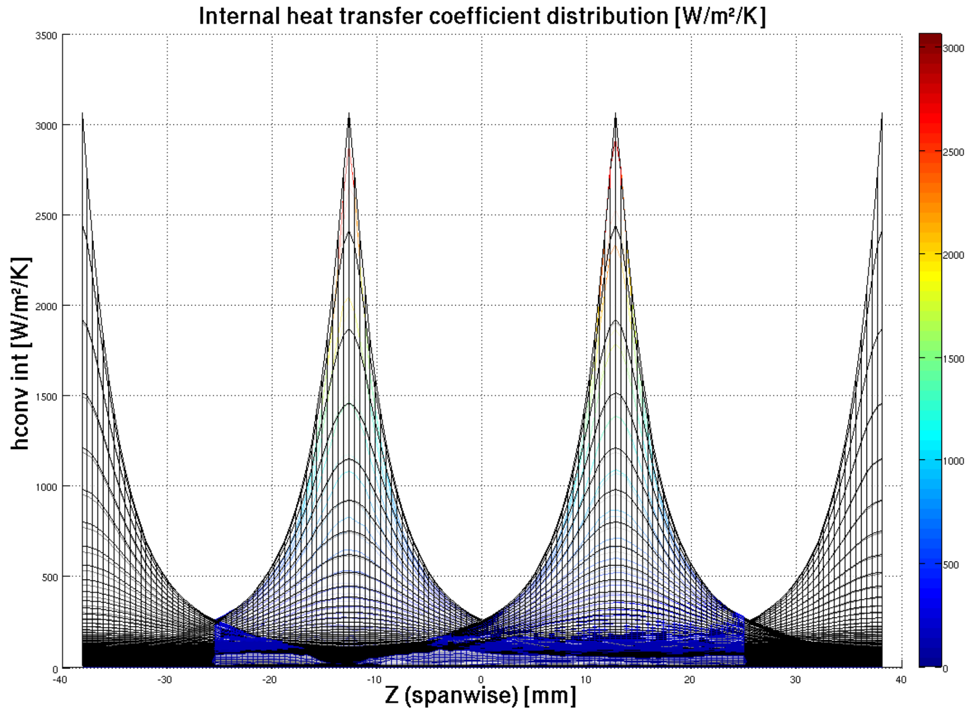

Figure B-16. HTC distributions from new correlation vs. CFD, case # 6 (close-up).

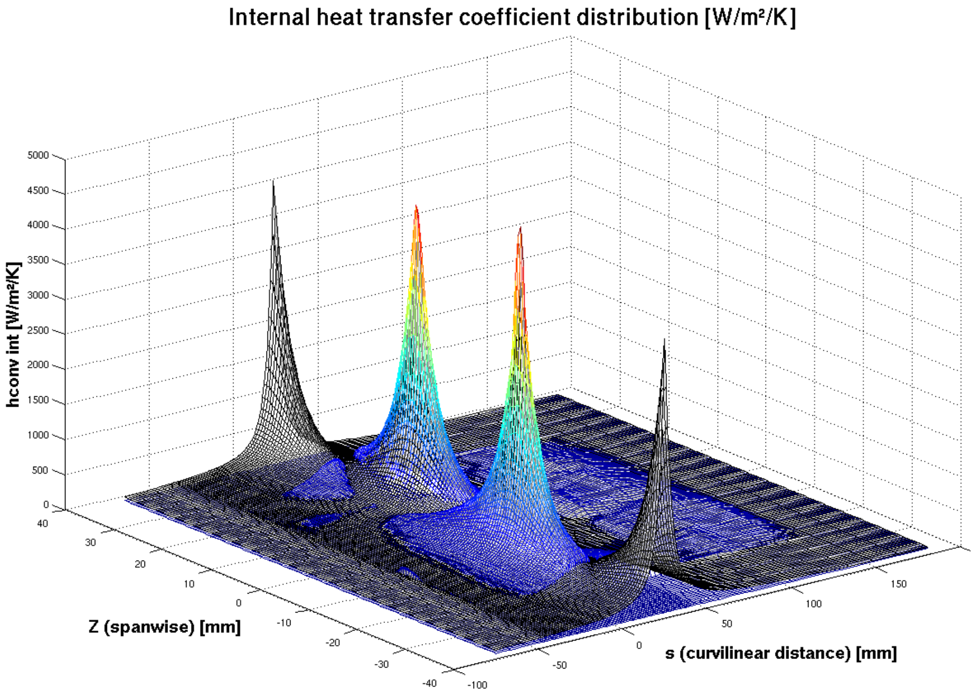

Figure B-17. HTC distributions from new correlation vs. CFD, case # 7.

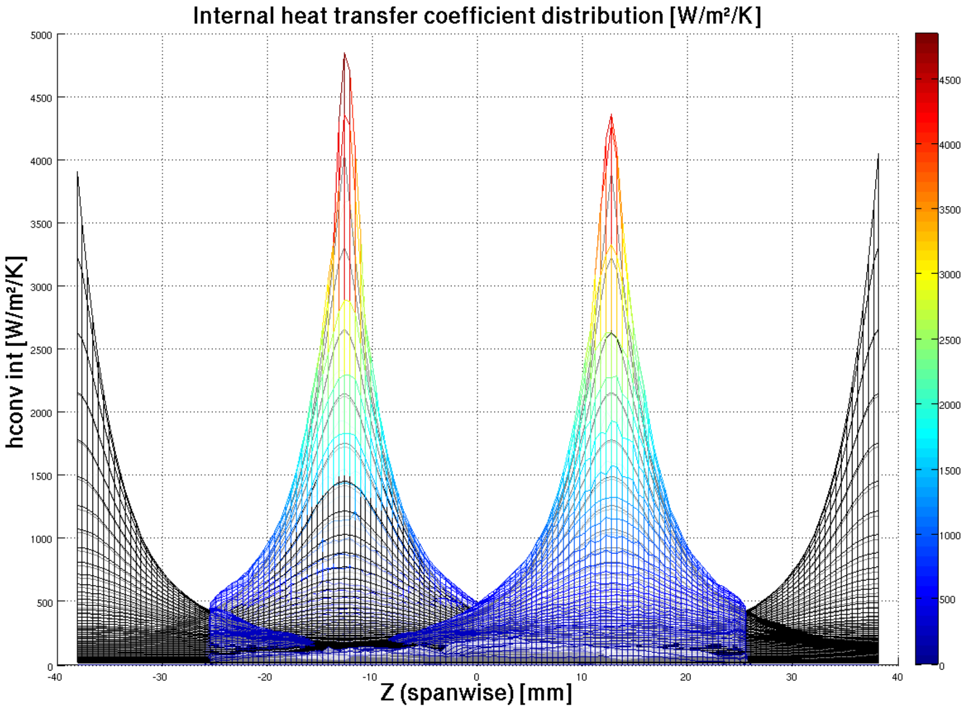

Figure B-18. HTC distributions from new correlation vs. CFD, case # 7 (close-up).

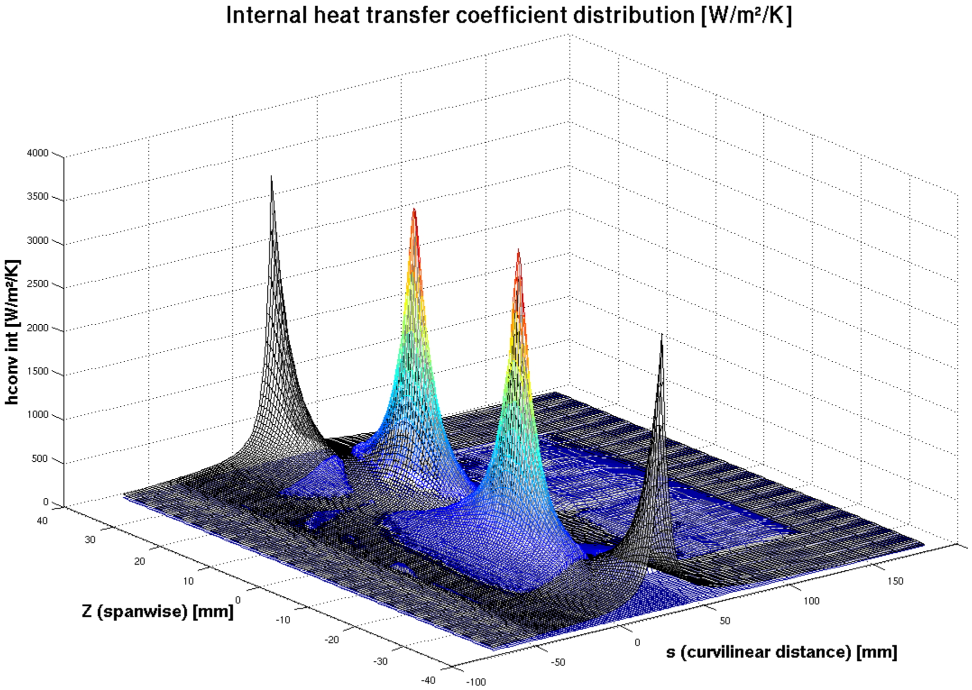

Figure B-19. HTC distributions from new correlation vs. CFD, case # 8.

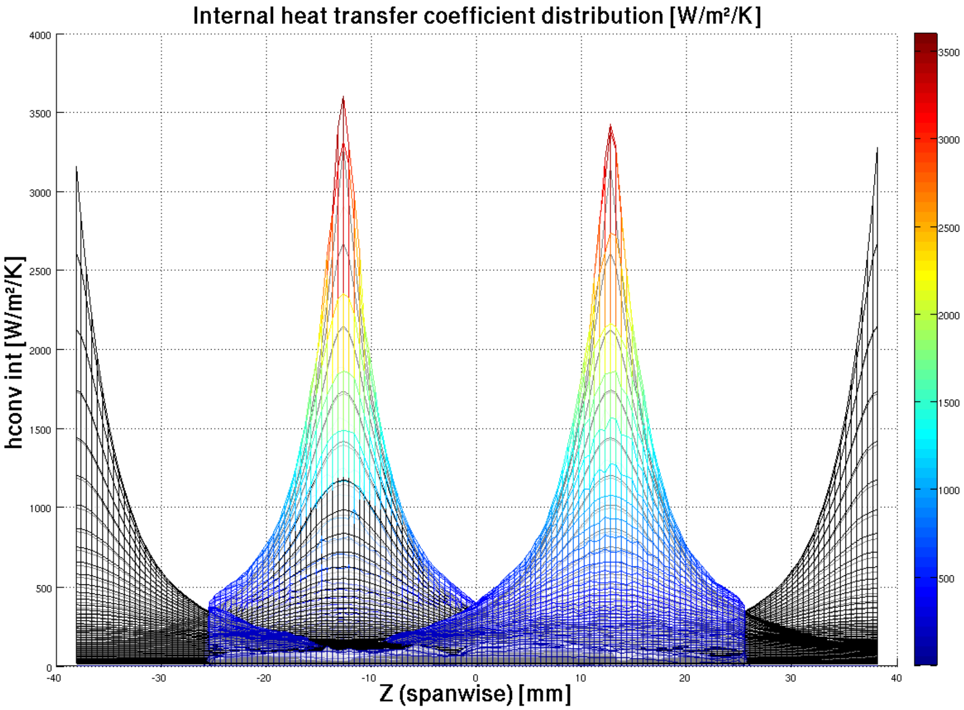

Figure B-20. HTC distributions from new correlation vs. CFD, case # 8 (close-up).

APPENDIX C

C. APPROXIMATION OF WATER RUNBACK SOLUTION USING POD

To give a sense of the accuracy of the POD model, the following results taken from the optimization procedure are presented. The solution computed directly from the water film model (shown in colors) is compared to the corresponding solution computed using the POD model (superimposed in black) for the same geometric configuration. The water runback mass flow rate surface distribution and the wall temperature distribution results are presented for three, four and five design variables.

In the case of three design variables, the results are very satisfactory. In the example shown in Figure C-1 and Figure C-2, the error for the water runback is included within -6.1% and +2.9%, and concerning the wall temperature, the error is within -1% and +0.8%, as shown in Figure C-3 and Figure C-4. More generally, the level of error for the water runback is evaluated about ±5% and about ±1% for the wall temperature. However, concerning water runback, the error at the relevant locations (meaning the upper and lower ends of the protected surface) is contained within ±3%.

In the case of four design variables, the results are still satisfactory even though the error ranges are slightly higher than in the previous case. In the example shown in Figure C-5 and Figure C-6, the error for the water runback is within -11.5% and +8.5%, and concerning the wall temperature, the error is included within -2.2% and +1.5%, as shown in Figure C-7 and Figure C-8. More generally, the level of error for the water runback is evaluated at about ±10% and about ±2% for the wall temperature. However, concerning water runback, the error at the relevant locations is contained within ±5%.

In the case of five design variables, the interpolation method seems to have more difficulties but the results are still satisfactory. In the example shown in Figure C-9 and Figure C-10, the error for the water runback is included within -21.1% and +25.2%, and concerning the wall temperature, the error is included within -3.8% and +4.9%, as shown in Figure C-11 and Figure C-12. More generally, the level of error for the water runback is evaluated about ±20% and for the wall temperature about ±5% (for five design variables). However, concerning water runback, the error at the relevant locations is contained within ±10%.

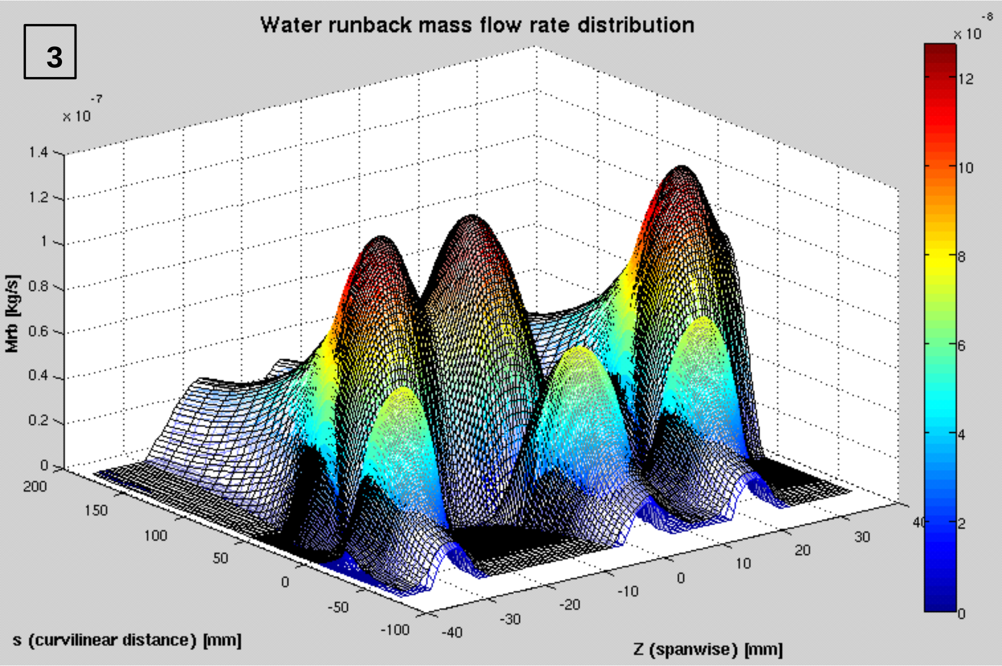

Figure C-1. Original and POD water runback mass flow distributions for 3 design variables.

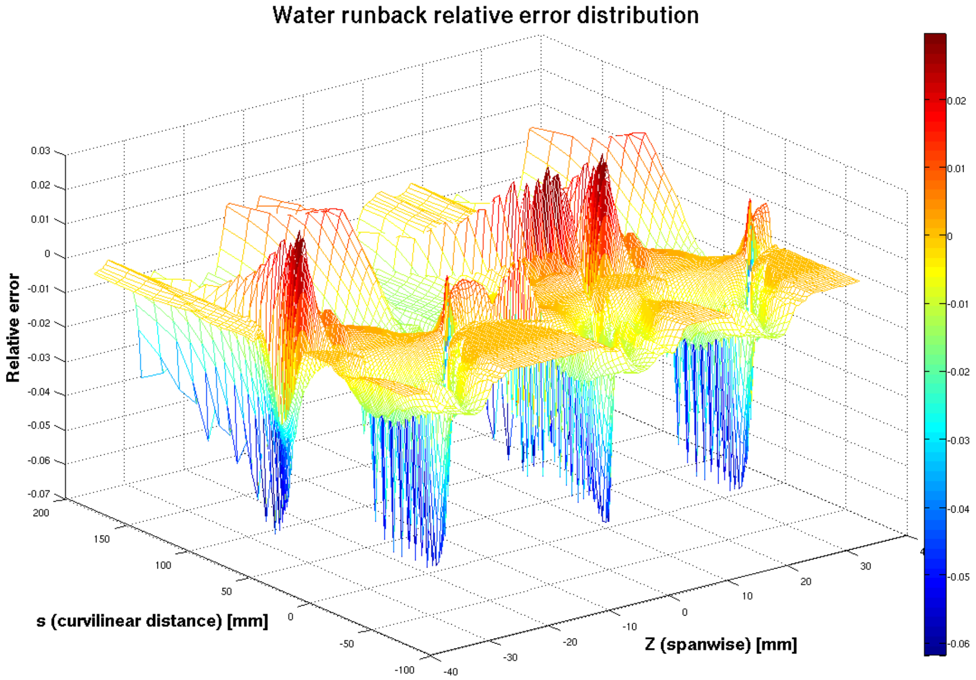

Figure C-2. Original and POD wall temperature distributions for 3 design variables.

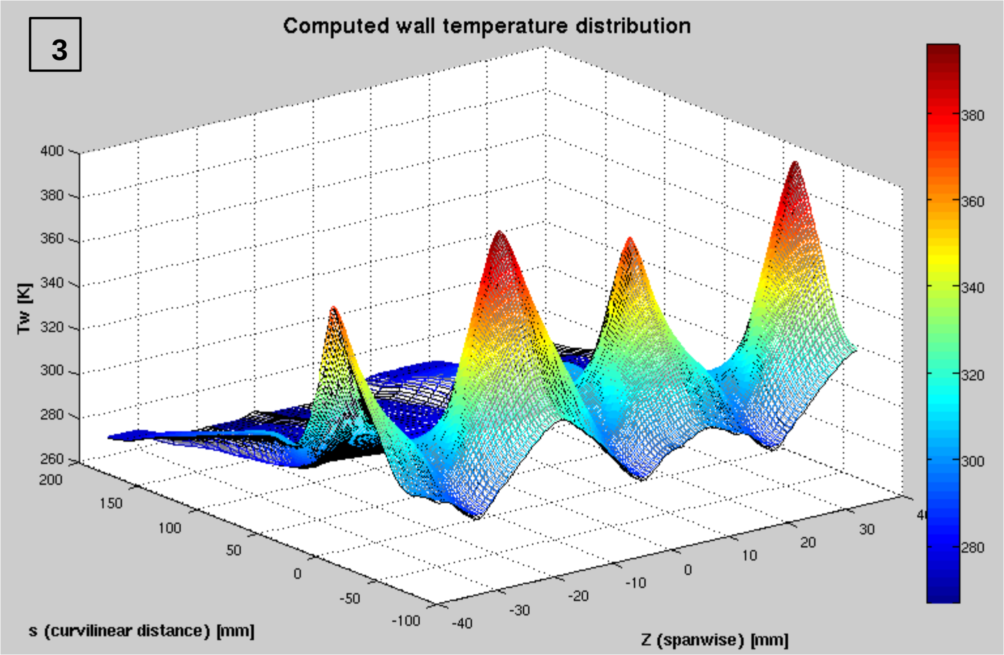

Figure C-3. Original and POD water runback mass flow distributions for 3 design variables.

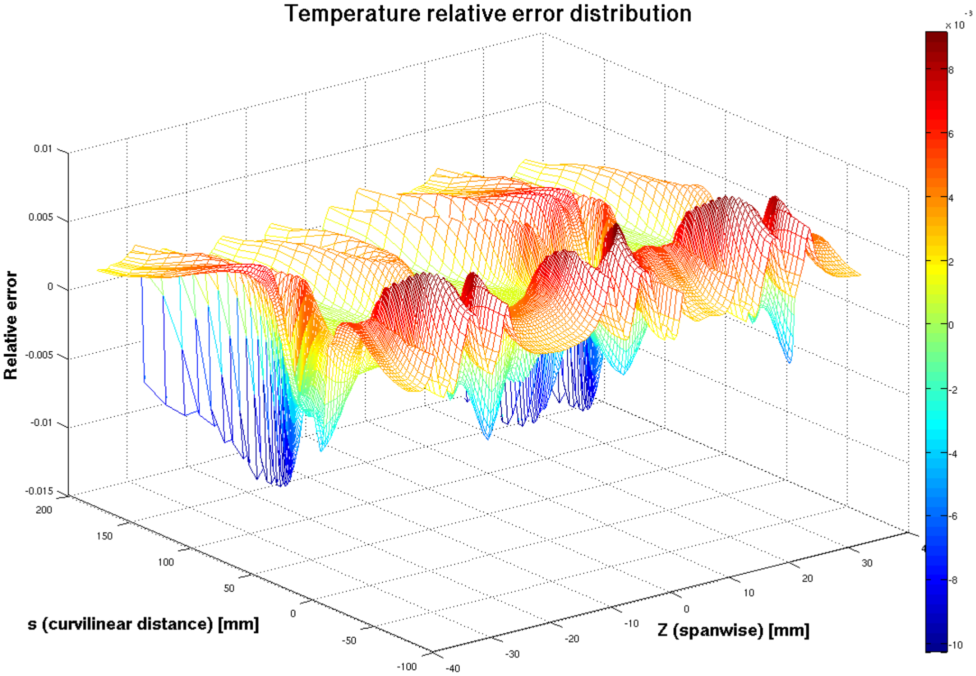

Figure C-4. Original and POD wall temperature distributions for 3 design variables.

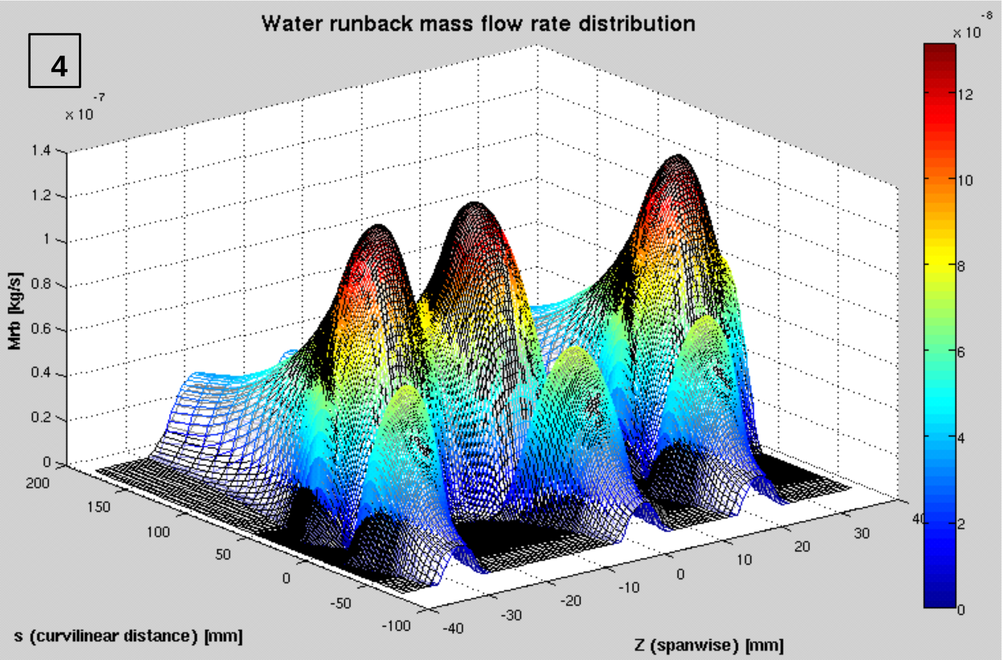

Figure C-5. Original and POD water runback mass flow distributions for 4 design variables.

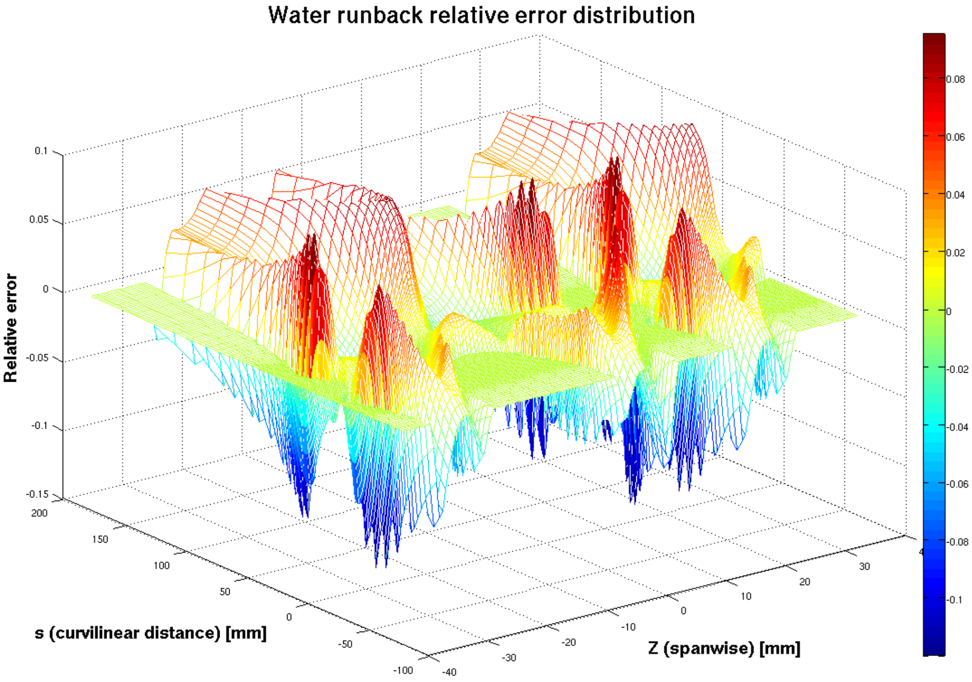

Figure C-6. Original and POD wall temperature distributions for 4 design variables.

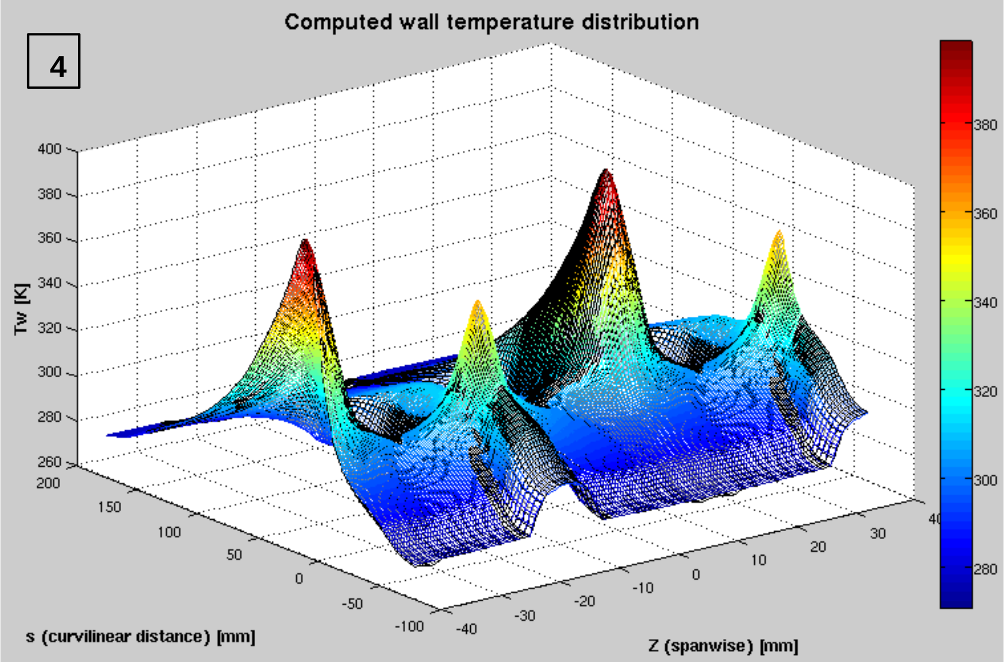

Figure C-7. Original and POD water runback mass flow distributions for 4 design variables.

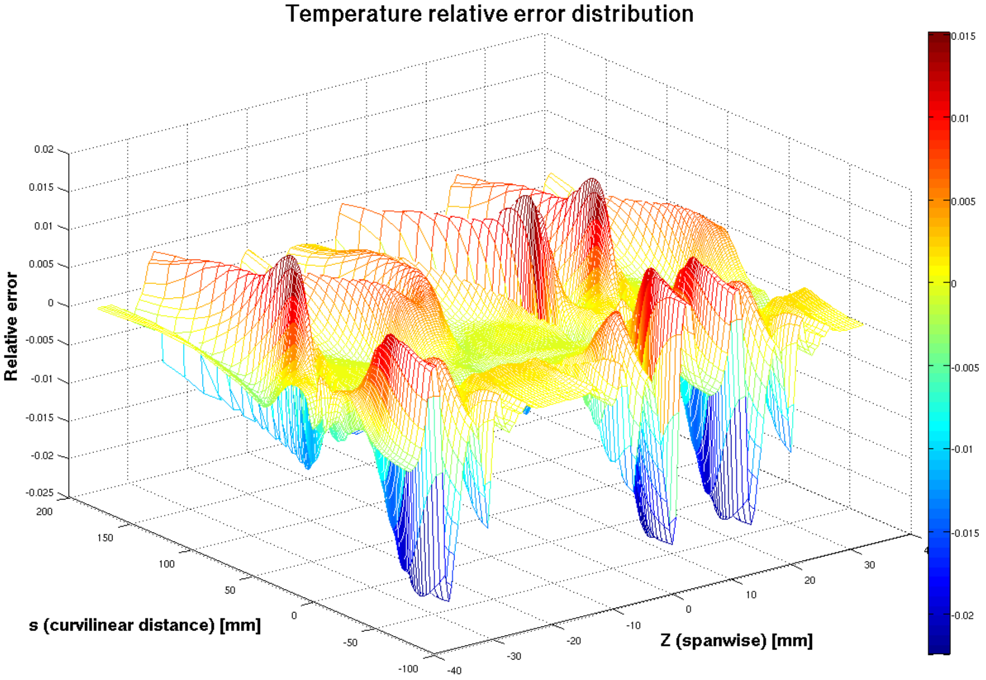

Figure C-8. Original and POD wall temperature distributions for 4 design variables.

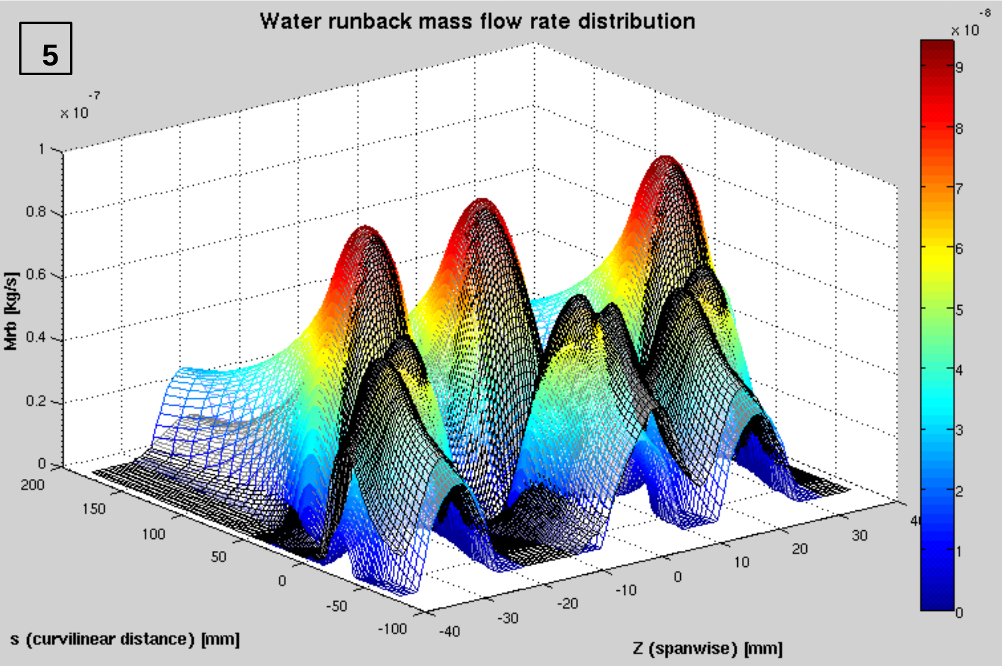

Figure C-9. Original and POD water runback mass flow distributions for 5 design variables.

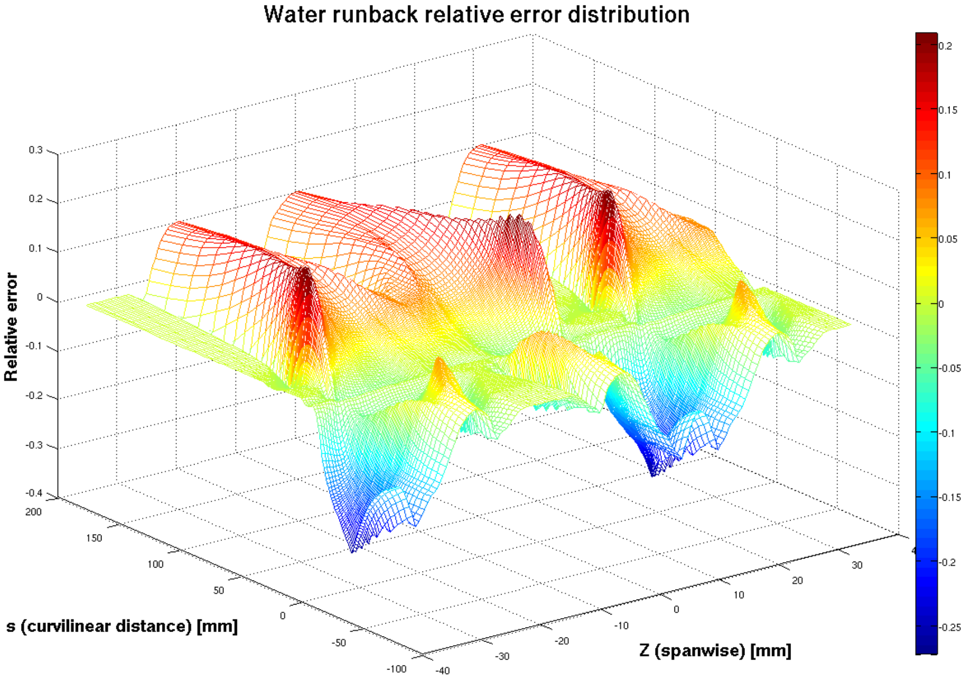

Figure C-10. Original and POD wall temperature distributions for 5 design variables.

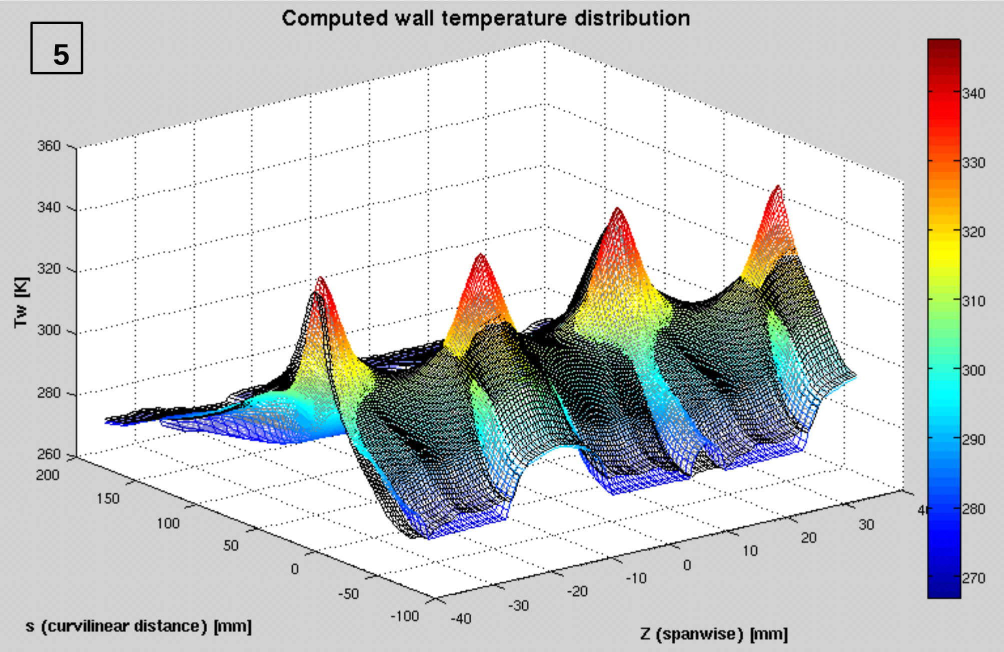

Figure C-11. Original and POD water runback mass flow distributions for 5 design variables.

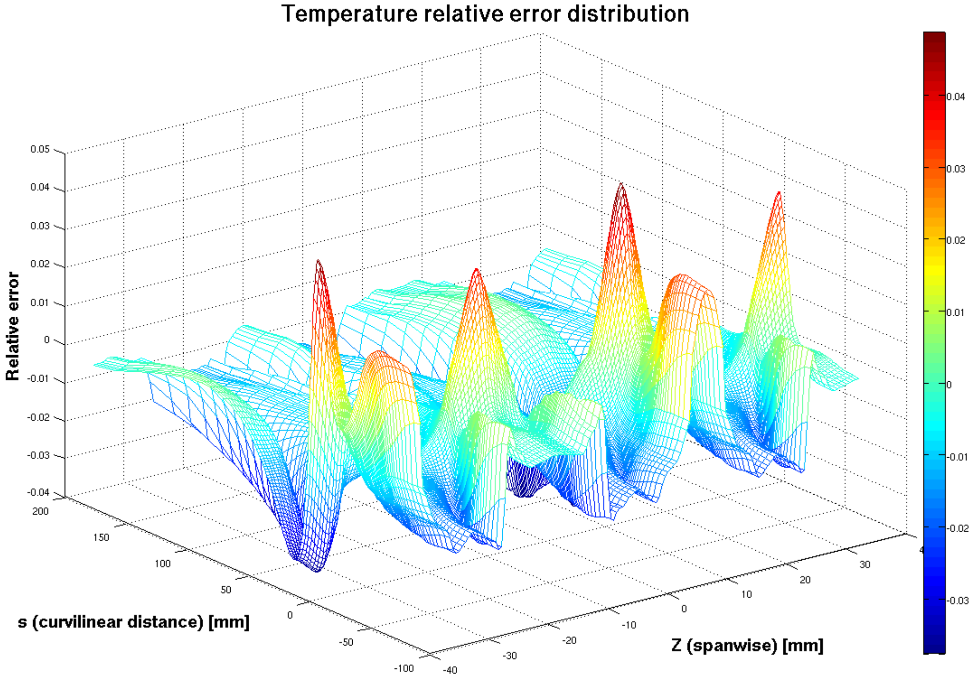

Figure C-12. Original and POD wall temperature distributions for 5 design variables.

This reveals to some extent some limitations of using a reduced order model. The introduced error might mislead the optimizer towards an "artificial" optimum since the water runback solutions are slightly biased and therefore do not correspond exactly to the associated geometric configurations, i.e. to the associated set of design variables. Nevertheless, these results are very encouraging since the error ranges are quite small and there is room for improvement with respect to the interpolation method and the ROM.

APPENDIX D

D. DIRECT OPTIMIZATION VERSUS SEQUENTIAL OPTIMIZATION

The difference between direct and sequential optimization is easier to visualize with a lower-dimension analogy in the case of a relatively simple arbitrarily chosen objective function, like the following 2D optimization example. The objective function contains a local minimum and a global minimum in order to use this example as a proof of concept and explain the genetic algorithm optimization process for both direct and sequential optimization.

D.1. Direct Optimization

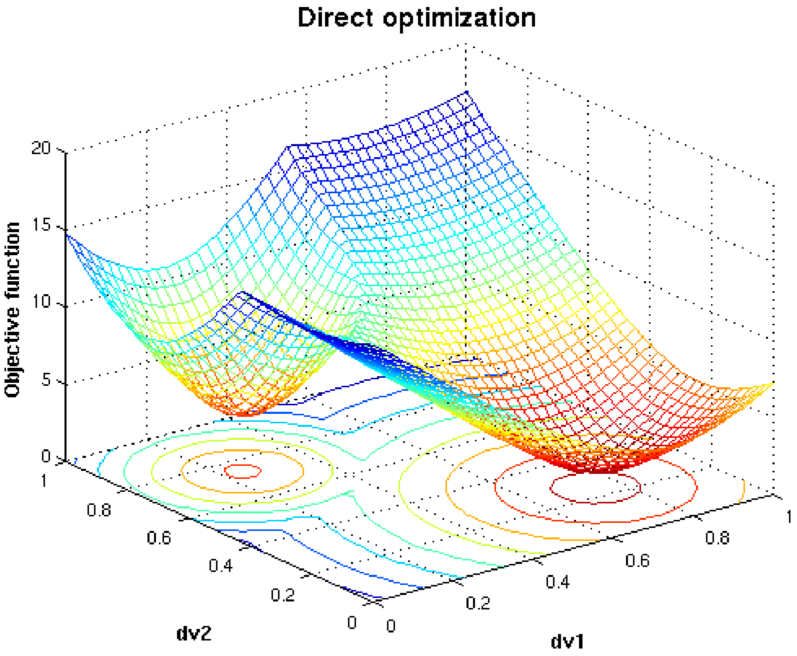

Figure D-1. 2D optimization example via direct optimization.

The 2D optimization example presented in Figure D-1 is implemented into the genetic algorithm module for a population size of 23 for 12 generations, with proportional fitness scaling, tournament selection method, a single point cross-over fraction of 80% and an elite count of two.

The population is initially uniformly spread over the two-design-variable design space, then the genetic algorithm process unfolds, gradually contracting the population towards the global minimum until complete convergence, as shown in Figure D-2.

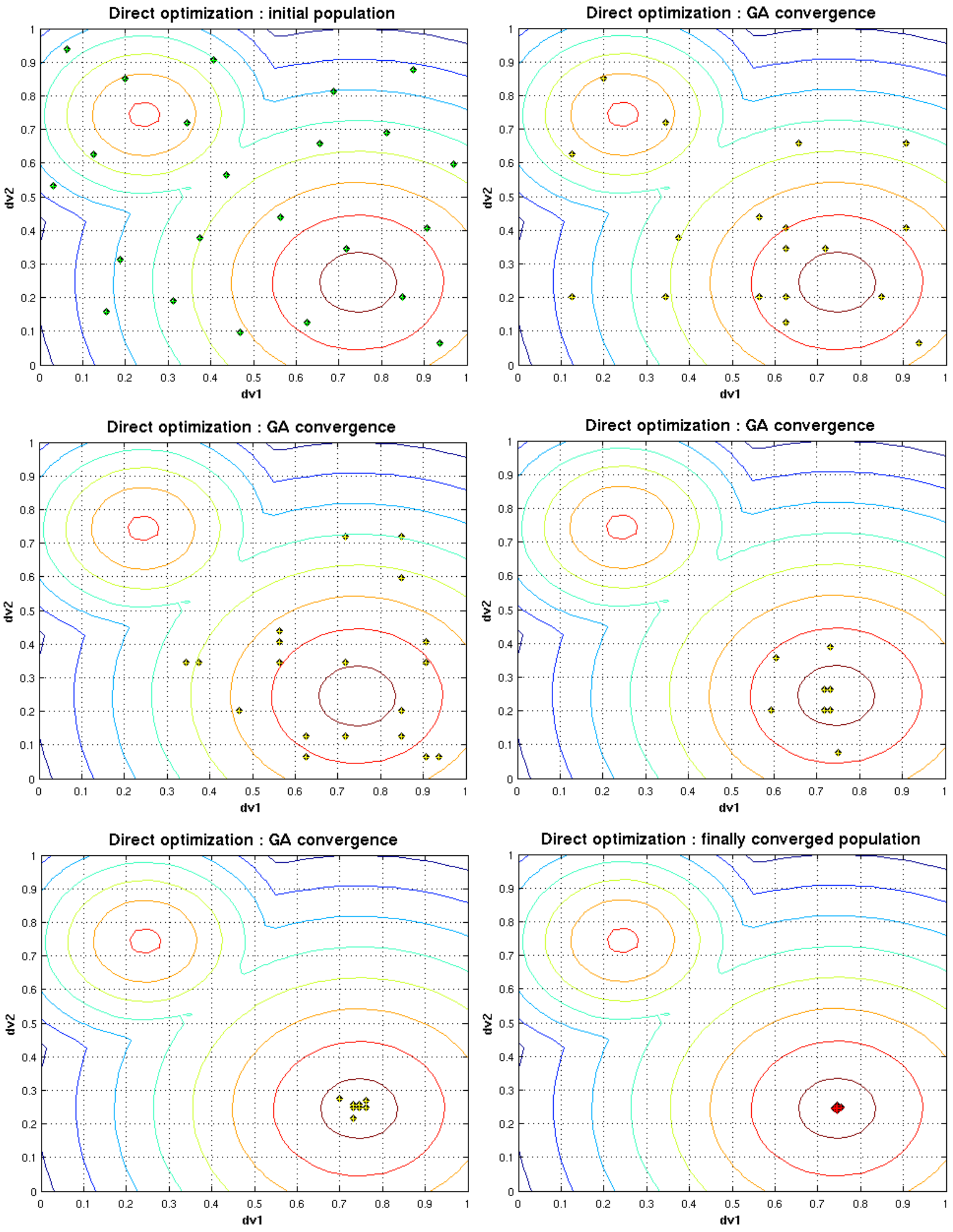

Figure D-2. Direct optimization from initial to final GA generation.

D.2. Sequential Optimization

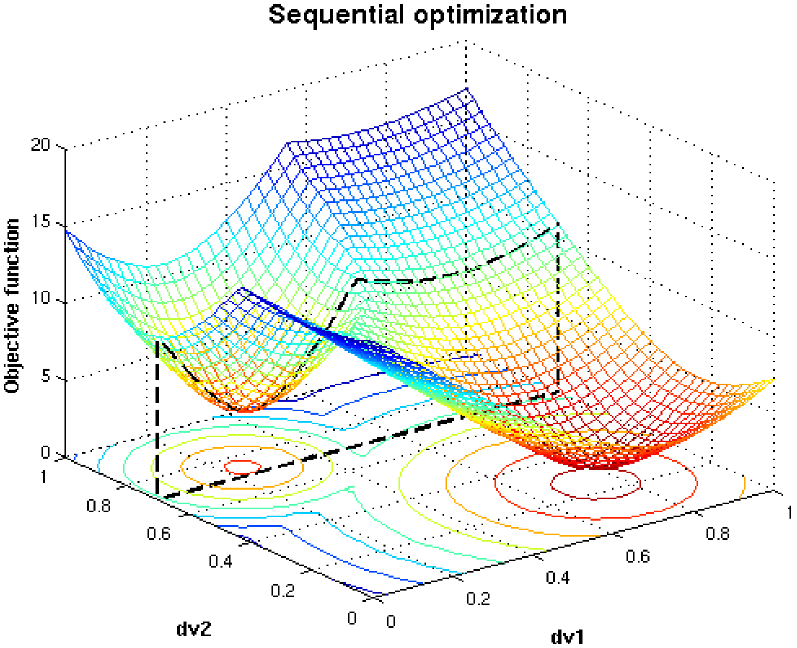

Figure D-3. 2D optimization example via sequential optimization: first step.

Sequential optimization is done in the following way. One of the two design variables is arbitrarily fixed, in order to first focus the search in the subspace of the remaining degree of freedom. In this case, the second design variable was set to 0.7, which can be visualized in Figure D-3 by the dotted-line-delimited plane.

On this 1D subspace, the population is uniformly distributed before launching the GA process which will also lead to the gradual contraction and final convergence about the global minimum of the subspace, which is in this case actually located relatively close to the local minimum of the two-dimensional design space, as shown in Figure D-4. Once the population has converged towards the optimum of the subspace, the additional degree of freedom is then released, so in this case, the second design variable is set free.

At that point, two alternatives can be encountered. Either the second step of the sequential optimization starts from the previously converged population, or it starts from an initial population obtained by spreading the 1D final population along the direction defined by the newly added design variable. These two cases were investigated and both led to a finally converging population located at the local minimum, as shown in Figure D-5 and Figure D-6. This shows that in certain conditions, especially without *a priori* knowledge of how the objective function behaves with respect to the constrained design variable(s), the GA does not guaranty completely avoiding converging towards a local extremum. Thankfully, it turns out that there are two types of remedy for this kind of behavior. The first one is mutation. Indeed, raising the mutation fraction from 20% to 75% in the first case and to 60% in the second case led to final converged population at the global minimum in both cases. However, this was done at the cost of more laborious convergence which would necessitate more than twice the number of generations (7+22 generations in the first case, 7+17 generations in the second case, as opposed to 12 for direct optimization). The second remedy is to use a less converged population from the 1D process, also spread along the direction defined by the newly added design variable, with a slightly higher mutation fraction (30% instead of 20%). This time, convergence towards the global minimum was achieved in 5+13 generations (cf. Figure D-7).

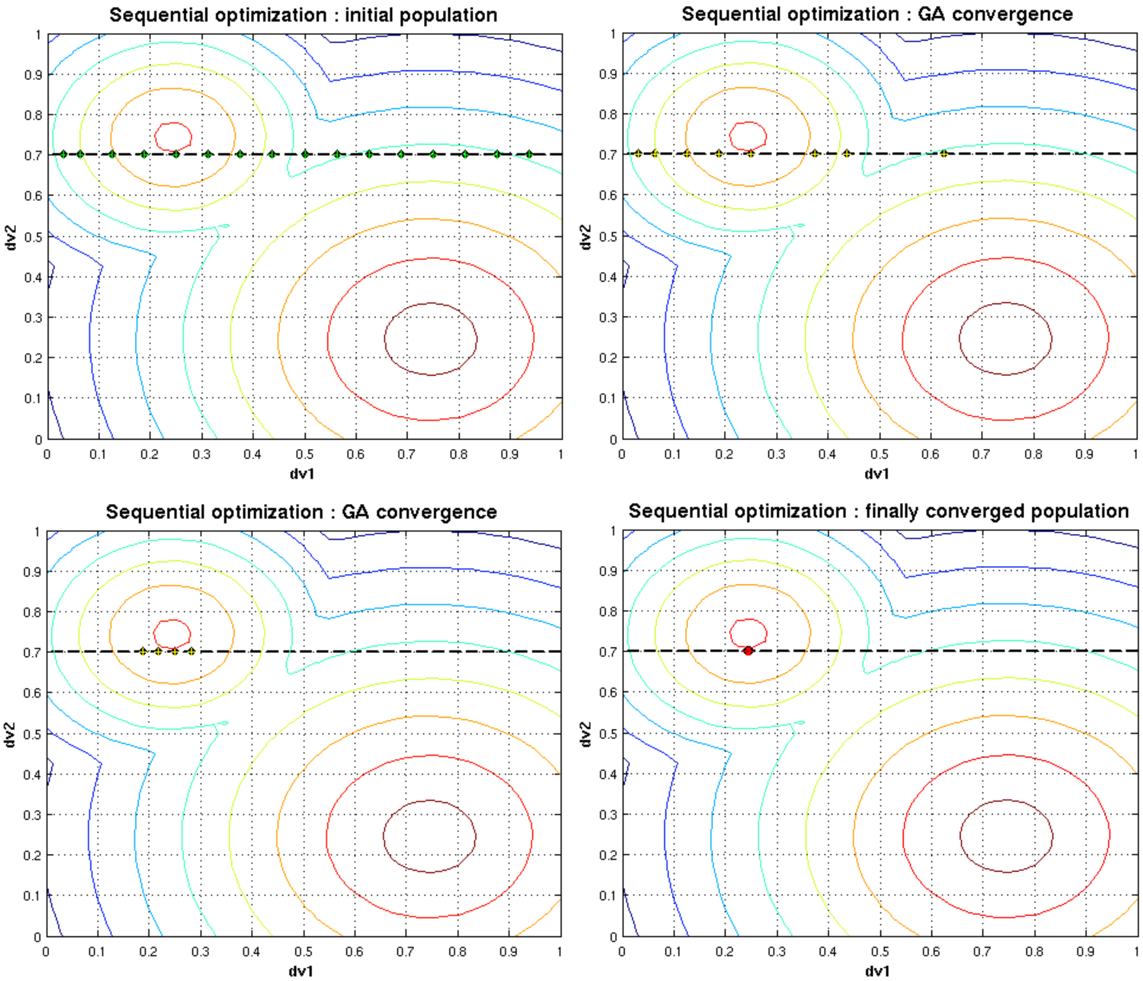

Figure D-4. Sequential optimization step 1: from initial to final GA generation.

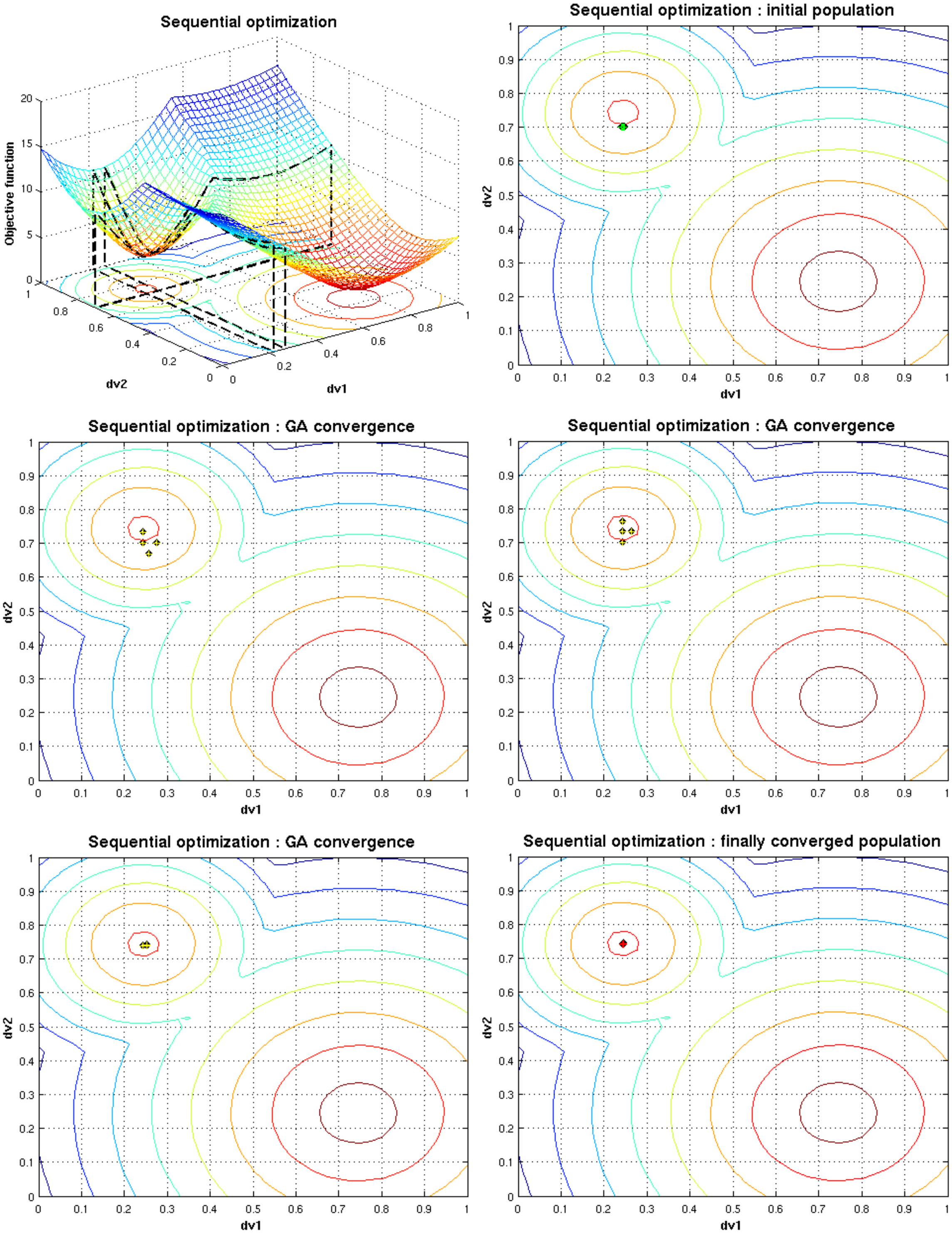

Figure D-5. Sequential optimization step 2: from initial to final GA generation.

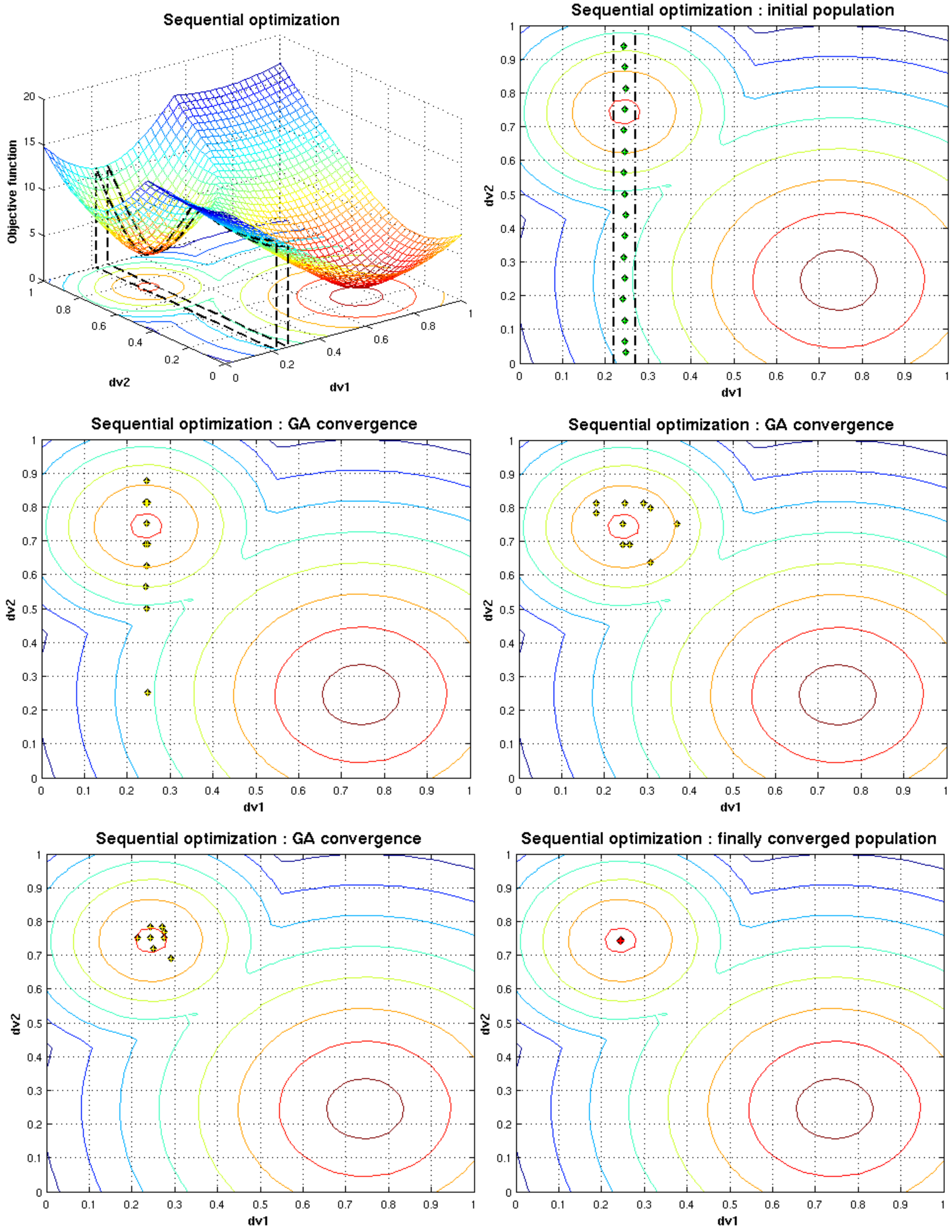
Sequential optimization

Sequential optimization : initial population

Sequential optimization : GA convergence

Sequential optimization : GA convergence

Sequential optimization : GA convergence

Sequential optimization : finally converged population

Figure D-6. Sequential optimization step 3: from initial to final GA generation.

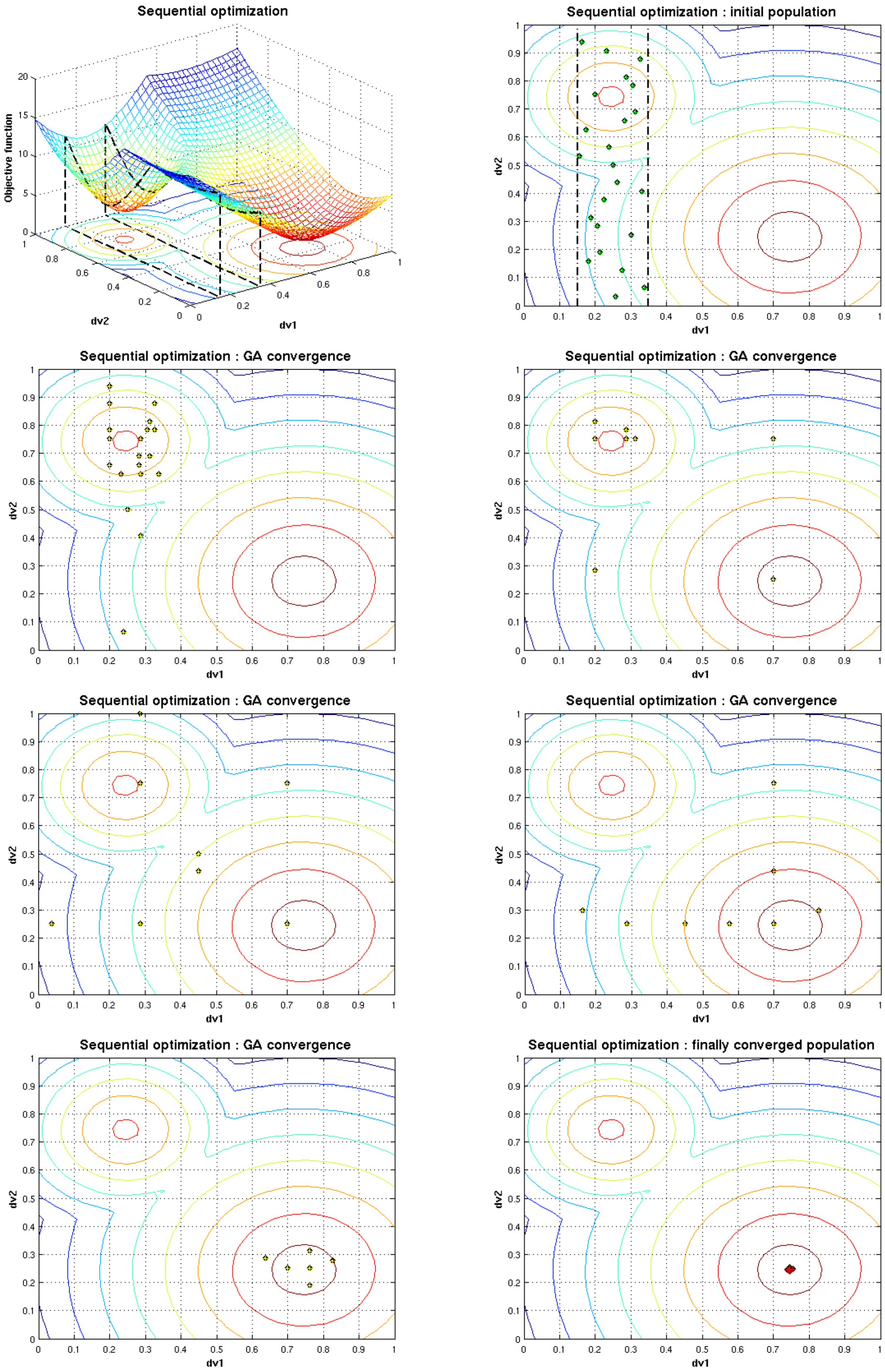
Sequential optimization

Sequential optimization : initial population

Sequential optimization : GA convergence

Sequential optimization : GA convergence

Sequential optimization : GA convergence

Sequential optimization : GA convergence

Sequential optimization : GA convergence

Sequential optimization : finally converged population

Figure D-7. Sequential optimization step 4: from initial to final GA generation.

From this simple example, it is quite obvious that when proceeding with sequential optimization, the optimal configuration of the subspace might only be a local optimum of the higher-dimension space. It is actually the most probable case since the subspace is constrained arbitrarily with respect to the remaining design variables. Therefore, starting from the lower-dimension optimal GA population results (even if it is uniformly spread in the supplementary dimension(s)) would not necessarily lead to significant improvement since it would introduce a bias in the GA initial population. It would moreover result in a more laborious convergence, since it would require a higher rate of mutation to recover the necessary diversity in the population.

Therefore, it would be more consistent and efficient to proceed with direct optimization, except in the case where *a priori* knowledge about the choice of the constrained design variables was available.

In any case, there is a compromise between accuracy and computational cost since increasing the population size will help the exploration of the design space and increase the consistency of the model, while increasing the number of generations will improve the convergence level and the consistency and repeatability of the results, at least as far as the genetic algorithm is concerned, but certainly at the cost of additional computations.